Quantum Transport in Topological Insulators and Nanopatterned Superconducting Systems

DISSERTATION ZUR ERLANGUNG DES DOKTORGRADES DER NATURWISSENSCHAFTEN (DR. RER. NAT.) DER FAKULTÄT FÜR PHYSIK

DER UNIVERSITÄT REGENSBURG

vorgelegt von

Stefan F. Hartl

aus München

im Jahr 2024

Promotionsgesuch eingereicht am: 27.03.2024

Die Arbeit wurde angeleitet von: Prof. Dr. Dieter Weiss

Prüfungsausschuss:

Vorsitzender:	apl. Prof. Dr. Juan-Diego Urbina
1. Gutachter:	Prof. Dr. Dieter Weiss
2. Gutachter:	Prof. Dr. Sergey Ganichev
weiterere Prüferin:	Prof. Dr. Milena Grifoni

Contents

Nomenclature

Abbreviations

$1D$	one-dimensional/one dimension
$2D$	two-dimensional/two dimensions
$3D$	three-dimensional/three dimensions
AC	alternating current
$AH\ 2700A$	Andeen-Hagerling 2700A capacitance bridge
ALD	atomic layer deposition
apl	außerplanmäßiger
AR	Allresist GmbH
BCS	Bardeen-Cooper-Schrieffer
BNC	bayonet Neill-Concelman
BZ	Brillouin zone
CAD	computer-aided design
CB	conduction band
CNP	charge neutrality point
$CSAR$	chemical semi amplified resist
DC	direct current
DF	Dirac fermion
DOS	density of states
DP	Dirac point
DUT	device under test
EBL	electron-beam lithography
ES	electron system
FFT	fast Fourier transform
$FQHE$	fractional quantum Hall effect
GL	Ginzburg-Landau
$GLAG$	Ginzburg-Landau-Abrikosov-Gor'kov
$HEMT$	high-electron mobility transistor
HS	hole system
ICB	integrated capacitance bridge
LL	Landau level
MBS	Majorana bound states
$MIBK$	methyl isobutyl ketone
NC	normal conductor
$PECVD$	plasma enhanced chemical vapor deposition

PID	proportional–integral–derivative
$PMMA$	polymethyl methacrylate
PVD	physical vapour deposition
QHE	integer quantum Hall effect
SC	superconductor
SdH	Shubnikov–de Haas
SEM	scanning electron microscope
SOC	spin-orbit coupling
TI	topological insulator
TSS	topological surface states
UHV	ultra-high vacuum
UV	ultraviolet
VB	valence band
vs	versus
VTI	variable temperature insert

Elements and chemical compounds

^3He	helium isotope with three nuclei
^4He	helium isotope with four nuclei
Al_2O_3	aluminium oxide
Ar	argon
Au	gold
Br_2	bromine
$C_2H_6O_2$	ethylene glycol
C_3H_9Al	trimethylaluminum
$CdHgTe$	cadmium mercury telluride
$CdTe$	cadmium telluride
Cr	chromium
Cu	copper
$GaAs$	gallium arsenide
H_2O	water
Hg	mercury
$HgTe$	mercury telluride
In	indium
N_2	nitrogen
N_2O	nitrous oxide
Nb	niobium
Pt	platinum
SiH_4	silane
SiO_2	silicon dioxide
Ti	titanium
$ZnTe$	zinc telluride

Physical constants

ϵ_0	vacuum electric permittivity	$8.854\,187\,812\,8 \times 10^{-12}\,\mathrm{F\,m^{-1}}$
μ_0	vacuum magnetic permeability	$1.256\,637\,062\,12 \times 10^{-6}\,\mathrm{N\,A^{-2}}$
$\mu_B = {e\hbar}/{2m_e}$	Bohr magneton	$9.274\,010\,078\,3 \times 10^{-24}\,\mathrm{J\,T^{-1}}$
$\Phi_0 = {h}/{2e}$	superconducting flux quantum	$2.067\,833\,848 \times 10^{-15}\,\mathrm{T\,m^2}$
$\Phi_0^m = {h}/{e}$	magnetic flux quantum	$4.135\,667\,696 \times 10^{-15}\,\mathrm{T\,m^2}$
c	speed of light in a vacuum	$299\,792\,458\,\mathrm{m\,s^{-1}}$
e	elementary charge	$1.602\,176\,634 \times 10^{-19}\,\mathrm{C}$
$h = 2\pi\hbar$	Planck constant	$6.626\,070\,15 \times 10^{-34}\,\mathrm{J\,Hz^{-1}}$
k_B	Boltzmann constant	$1.380\,649 \times 10^{-23}\,\mathrm{J\,K^{-1}}$
m_e	electron mass	$9.109\,383\,701\,5 \times 10^{-31}\,\mathrm{kg}$
$R_\mathrm{K} = {h}/{e^2}$	von Klitzing constant	$25\,812.807\,45\,\Omega$

1. Introduction

1.1. Thunderbolt and lightning

In the dark atmosphere of a thunderstorm, the bright flash of lightning is a spectacular natural phenomenon that must have fascinated humans since the dawn of mankind. The awe associated with this force of nature is deeply rooted in human consciousness. In Greek mythology, Zeus, the king of the gods, was repeatedly described by the poet Hesiod as wielding a "thunderbolt and lightning" [1]. These words also appear in modern art, such as in Queen's world-famous song Bohemian Rhapsody. Moreover, lightning is probably the most prominent example of electricity in nature. The connection between the two, i. e. that lightning is an electrical phenomenon, was not a priori obvious, but became clear with the flying kite experiment attributed to Benjamin Franklin [2]. Today, it is widely known that lightning is a flow of electric current, typically between a cloud and the earth, caused by an electrostatic potential difference. Research has also shown that the shape of lightning forms a fractal, self-similar pattern [3–5]. Lightning is just one example of an electrical phenomenon that has shaped culture, art, natural sciences and mathematics. The desire to understand such phenomena must have been a human desire long before the corresponding concepts and terminology were developed. Nowadays, we know that electricity and magnetism are interconnected and deeply rooted in each other, as reflected by the famous equations of James Clerk Maxwell [6].

This dissertation explores the topic of electricity and magnetic fields at a small scale, focusing on quantum physical effects. It describes electrons that can only move on the surface of the bulk of a new class of materials, but not inside it. It discusses the behaviour of electric currents and voltages in a strong magnetic field, which results in the conductivity always being a multiple of the exact ratio between the square of the elementary charge and Planck's constant. It also describes electric charges stored in a capacitor with such a low density of states, that alongside the known electrical capacitance an additional quantum capacitance appears. It addresses the phenomenon of currents that can flow with zero resistance due to their macroscopic quantum state, and explains the process of trapping magnetic flux quanta in an environment with numerous small holes. And finally, it shows that the electrical resistance in this environment can, similar to lightning, exhibit a complicated pattern with fractal features.

1.2. Historical overview

Our understanding of the laws of nature and their description through physics has grown dramatically since Maxwell's time. This section lists the most significant discoveries related to this thesis. It is divided into three parts, addressing historical developments in the fields of superconductivity, topological insulators and Majorana bound states.

In 1911, Heike Kamerlingh Onnes discovered **superconductivity** while measuring the resistance of mercury at liquid helium temperatures [7]. In 1950, Vitaly Ginzburg and Lev Landau published their theory explaining the phenomenon of superconductivity [8]. Seven years later, Alexei Abrikosov described the periodic lattice in which vortices are arranged in type-II superconductors [9, 10]. It was later shown that these Abrikosov vortices can host low-energy excitations called Caroli-de Gennes-Matricon states [11]. In 1984, Bernard Pannetier demonstrated that a fractal fine structure of the upper critical field line can be observed in a superconducting network made of small holes [12]. This fractal fine structure is related to the lower edge of the Hofstadter butterfly energy spectrum [13].

Quantum physics flourished throughout the first half of the 20th century, and in the 1940s solid-state physics emerged as an independent discipline [14, 15]. This gave rise to an incredible number of technical developments that have shaped our lives today. One of the most important of these developments has been microelectronics. It was in one such microelectronic structure, a metal-oxide-semiconductor field-effect transistor, that Klaus von Klitzing discovered the quantum Hall effect in 1980, where the Hall resistance exhibits quantized values [16, 17]. In 2005, Charles Kane and Eugene Mele described a new class of materials called **topological insulators** in two dimensions (2D) [18]. Two years later, together with Liang Fu, they extended their theory to three dimensions (3D) [19]. Unlike trivial insulators, these insulators have topologically protected conducting states between the conduction and valence bands. These states are located at the edges of a 2D plane or on the surfaces of a 3D bulk [20]. Andrei Bernevig proposed a CdTe/HgTe/CdTe quantum well system to construct such a topological insulator [21], which was later realised experimentally [22].

In 1937, the Italian physicist Ettore Majorana postulated the existence of a new particle in elementary particle physics [23]. This Majorana fermion is unique in that it is its own antiparticle. The following year Majorana disappeared in circumstances that remain unexplained to this day [24]. In 2008, 70 years later, it was again Fu and Kane who proposed that the combination of s-wave superconductors [25] and topological insulators could lead to the formation of quasiparticle excitations at their interface, which have properties similar to Majorana fermions [26]. These quasiparticle excitations are called **Majorana bound states** (MBS). When Cooper pairs tunnel into the 3D topological

insulator due to the superconducting proximity effect, and Abrikosov vortices with a flux equal to a superconducting flux quantum are present, MBS are formed at zero-energy in the vortex core [20, 27, 28]. Unlike the fermionic particles proposed by Ettore Majorana, MBS are not fermionic or bosonic but follow non-Abelian exchange statistics [29]. They are also known as anyons because they can have 'any' phase when two particles are interchanged [30, 31]. The properties of MBS make them suitable candidates for fault-tolerant quantum computation, which is the main driver for the search for them [32].

This thesis is related to or builds upon all the physical discoveries mentioned above. However, it is important to note that this is not a complete list, as there are undoubtedly many more historically significant names and discovered effects that could be included in this introduction.

1.3. Initial motivation

The unifying element of the experiments described in this thesis is the initial motivation: the search for signs of **Majorana bound states** in a heterostructure consisting of a superconductor and a strong 3D topological insulator based on HgTe. Niobium (Nb) was chosen as the superconductor for this purpose. The Nb layer is perforated with an array of periodically arranged holes, the so-called antidot lattice. This is displayed in figure 1.1. Assuming a square

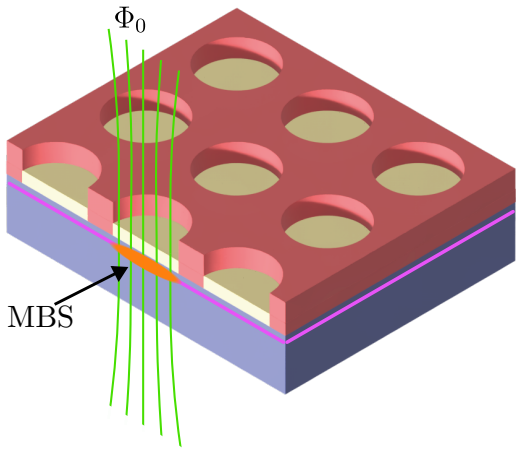

Fig. 1.1.: Simplified illustration of the emergence of Majorana bound states. A film of superconducting Nb (red), perforated with antidots, is deposited on the 3D topological insulator made of HgTe (purple). The yellow material is CdTe, which was removed around the antidots so that the HgTe surface states (magenta, only shown for top surface) can be proximitized by the superconducting Nb. Magnetic field lines are shown in green, depicting a single vortex with one flux quantum Φ_0. The zero-energy MBS (orange) are expected at the proximitized surface states of the HgTe. Topgate and insulator are not shown for clarity in this figure.

lattice constant $a_\square$, an external magnetic field of $B = \Phi_0/a_\square^2$ can generate exactly one flux quantum Φ_0 per antidot. The vortices tend to be located inside the antidots, as the antidots act as pinning centres [33]. Additionally, at millikelvin temperatures the HgTe is proximitized by the superconducting Nb [34, 35]. When all of these factors are combined, each antidot is expected to host zero-energy MBS [28]. The antidot cavity also serves the purpose of eliminating the Caroli-de Gennes-Matricon states [11, 36, 37], which would otherwise be challenging to differentiate from the MBS [38]. To detect the MBS, an electrical insulator and a metallic top gate are applied on top of the HgTe-Nb heterostructure, creating a capacitor. When the capacitance of such a system is measured, the so-called quantum capacitance appears in addition to the capacitance associated with the dielectric medium. This quantum capacitance is directly proportional to the thermodynamic density of states of the system [39]. The presence of Majorana bound states (MBS) in the antidots is expected to lead to an increased density of states, which should be reflected by a larger capacitance signal.

No evidence of MBS was found during the research phase of this thesis. However, a number of interesting physical effects were observed, which can be grouped together into two types of experiments. This thesis focuses on describing these effects.

1.4. Abstract

The first experiment discussed in this thesis investigates strained 3D HgTe, a strong topological insulator with conducting surface states [19]. Figure 1.2 (a) shows a pronounced quantum Hall effect observed at millikelvin temperatures in a magnetic field perpendicular to the sample geometry. This effect occurs despite the fact that the current is carried by electrons from the top surface, the bottom surface, and the bulk conduction band. Transport measurements were performed in a 4-terminal Hall geometry. Here, all charge carrier classes contribute to the current flow. 2D colour plots of the conductivity reveal different coexisting Landau fans, each of which can be assigned to a distinct electron species. Additionally, the magnetocapacitance was measured. The low density of states of a two-dimensional electron system (2DES) allows for the observation of the quantum capacitance, which is directly proportional to the thermodynamic density of states [40, 41]. This also permits drawing conclusions about the Landau levels. Since the capacitance measurements primarily probe the uppermost layer of charges, below 6 T only one Landau fan belonging to the 2DES of the top surface can be observed [39]. At high magnetic fields, the picture changes. Both the transport and capacitance measurements consistently show only one Landau fan, reflecting the total electron density of the system. The conclusion is that as the magnetic field increases, the different Landau levels

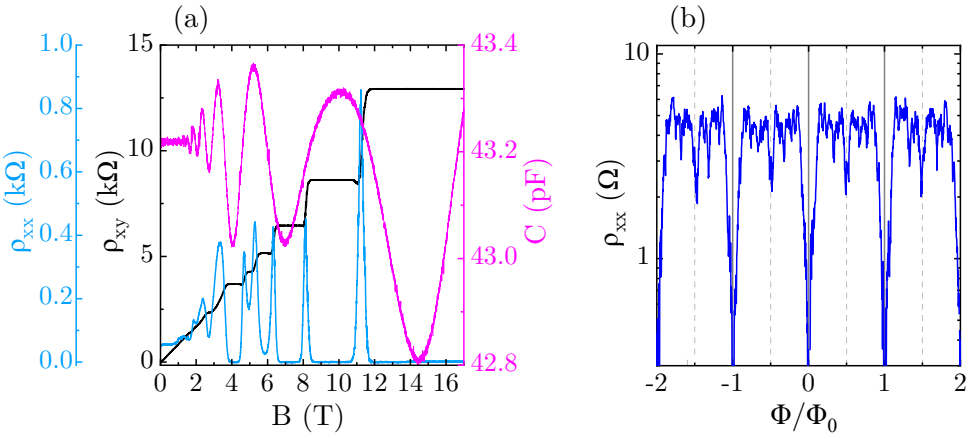

Fig. 1.2.: (a) Quantum Hall effect (black), Shubnikov-de Haas oscillations (turquoise) and capacitance (magenta). (b) Integer flux periodic resistance oscillations with fractional features.

merge into a single Landau fan. Consequently, at sufficiently high magnetic fields only one carrier species remains.

For the second experiment, a superconducting niobium film was deposited onto the HgTe. The film is perforated with an array of periodically arranged holes, so-called antidots. When an external magnetic field is applied perpendicular to the sample geometry, vortices with quantized magnetic flux are formed in the Nb [9]. The vortices tend to be trapped inside the antidots due to the attractive pinning potential of the antidots [33]. If the periodicity of the antidot lattice is commensurable with the strength of the magnetic field, the vortices form a stable lattice. The trivial case is when there is exactly one flux quantum per antidot, and the vortices assume the geometry of the perforated lattice [42]. The pinning properties of the antidots have been observed through transport measurements, which showed periodic oscillations of the resistance as a function of magnetic flux, as shown in figure 1.2 (b). Moreover, measurements of the differential resistance show that the integer pinning configurations remain stable even at high currents. Additionally, more detailed resistance measurements also reveal a pronounced fractional fine structure, which is associated with the lower edge of the fractal energy spectrum of the Hofstadter butterfly [12, 13]. This suggests complex yet stable lattice configurations of the vortices.

1.5. Thesis outline

The physics involved in the experiments on HgTe and those on Nb-HgTe heterostructures are very different. This thesis is structured to avoid a large separation between the theoretical and the corresponding experimental chapters. The thesis is therefore organised as follows:

- **Chapter 2** introduces topological insulators with a focus on 3D HgTe.

The chapter provides a concise overview of the key aspects of theoretical physics that are necessary for understanding the following chapters.

- **Chapter 3** proceeds with an explanation of transport in 2D electron systems, including the Drude model, the integer quantum Hall effect, and the concept of quantum capacitance. All of these topics are essential for the understanding of the results presented in chapter 6.
- **Chapter 4** covers the fabrication of the samples, outlining each step, with a particular emphasis on antidot lattices.
- **Chapter 5** explains the cryogenic measurement techniques. As a variety of setups were used to measure the samples, these are described individually. The chapter primarily focuses on the difficulties of capacitance measurements and their solutions.
- **Chapter 6** presents the magnetoresistance and capacitance measurements on the HgTe samples. It begins by detailing the complex characterisation of the wafer and the associated electrostatic model. The Landau levels observed in the capacitance and conductivity colour maps are then assigned to the individual two-dimensional electron and hole systems. It concludes with a section showing that at very high magnetic fields, the individual systems merge into a single system.
- **Chapter 7** is a theoretical chapter discussing superconductivity with a focus on the Ginzburg-Landau theory, which is briefly introduced. Subsequently, the behaviour of vortices in the superconductor is explained. In particular, an understanding of the interactions between the vortices and the antidots is established. This lays the foundation for understanding the results presented in chapter 8.
- **Chapter 8** shows experimental results of the observed pinning behaviour of the vortices in heterostructures made of Nb antidots and HgTe. The chapter starts with a characterisation of Nb. Then the integer pinning characteristics of the vortices are analysed. This is done by studying the number of vortices that can be pinned per antidot and how the pinning is affected by the current. Finally, the fractional pinning features that occur are presented and an attempt is made to determine their fractional values.
- **Chapter 9** summarizes the results and discusses possible opportunities and challenges.
- **Appendix A** contains a list of the individual sample fabrication steps belonging to the fourth chapter.
- **Appendix B** supplies additional data sets of the experimental results.

2. Topological insulators

Topology is a mathematical discipline concerned with the properties of geometric objects that remain unchanged when the objects undergo continuous deformation. For instance, a cup with a handle can be compared to a simit, a round loaf of bread with a hole in the middle (shaped like a torus). Both objects have a single hole. The key aspect is that the shape of the cup can be continuously altered until it becomes the shape of the simit, without closing or opening a hole. Therefore they are in the same topological class. For a counterexample, a sphere with no holes or a pretzel with three holes can be considered. It would be necessary to open or close the holes in order to continuously deform one into the other. Both of these objects therefore belong to distinct topological classes.

In solid-state physics, topology is also utilized. There, the closing and reopening of energetic gaps within the band structure is necessary to transform materials of different topology from one to another. The topological properties of insulators can be compared by analysing their potential for transformation into one another and determining whether it is necessary to open or close a band gap during the process. This opening or closing of the band gap is equivalent to the opening or closing of the hole. One can distinguish between trivial insulators, such as vacuum or SiO_2, and topological insulators, such as HgTe, as they are characterised by **topological invariants** [43].

Topological insulators (TI) are materials which are electrically insulating within their bulk, whilst being conductive on their surface. Figure 2.1 shows, that the surface states also exist within the band gap and are therefore called gapless. The 3D TIs based on HgTe which were investigated in this thesis have a three-dimensional, insulating bulk and two-dimensional, conductive topological surface states.

The detailed theoretical explanation of topological physics extends beyond the scope of this thesis. However, in order to understand the experimental results of this study, a rather concise theoretical framework is presented here. First, the concept of the Berry phase is introduced briefly. This is required for the derivation of the topological invariant known as the Chern number $\mathcal{C}$. The latter has a significant role in the categorization of the quantum Hall effect, as it is equivalent to the filling factor ν. This is followed by a brief discussion of the periodic table of topological invariants and the $\mathbb{Z}2$ invariant, which is used to

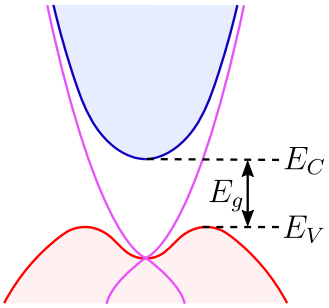

Fig. 2.1.: Simplified HgTe band structure. As an example for the electronic band structure of a topological insulator, the simplified energy dispersion of 3D HgTe is presented. The band gap E_g is spanned by the bottom of the conduction band E_C shown in blue, and the top of the valence band E_V shown in red. In contrast to trivial insulators, there are additional gapless topological surface states (TSS) which are shown in magenta.

classify TIs in 3D. Afterwards, the particular properties of the surface states are explained. Finally, the topic is narrowed down to HgTe: to understand how the chemical compound HgTe becomes a 3D TI, it is essential to elaborate on three fundamental aspects. The first is the inverted band structure, the second is the occurrence of surface states, and the third is the emergence of the band gap. The book by Gross and Marx [43] provides a clear overview of the topic. An in-depth analysis can be found in the textbooks of Shen [20] or Bernevig [44].

2.1. Berry phase and Chern invariant

The Berry phase is named after Michael Victor Berry, who published his work on the concept in 1984 [45]. The role of the Berry phase in Bloch-periodic systems in solid state physics was further developed by Joshua Zak [46].

In a crystal, an electron is described by eigenfunctions which are called Bloch functions $\Psi_{n,\mathbf{k}}(\mathbf{r})$. Here, $\mathbf{k}$ is the crystal momentum vector, $\mathbf{r}$ is the position and n refers to the nth energy band. The energy eigenstates of the Hamiltonian $\mathcal{H}(\mathbf{k})$ are then given by

$$u_{n,\mathbf{k}}(\mathbf{r}) = e^{-i\mathbf{k}\cdot\mathbf{r}}\Psi_{n,\mathbf{k}}(\mathbf{r}), \tag{2.1}$$

whereas e is Euler's number and $i = \sqrt{-1}$ is the imaginary unit. The Berry connection of the nth band is then defined as [47]

$$\mathbf{A}_n(\mathbf{k}) = i\langle u_{n,\mathbf{k}}|\nabla_{\mathbf{k}}|u_{n,\mathbf{k}}\rangle. \tag{2.2}$$

This Berry connection is used to derive the **Berry phase** γ_n, which is

$$\gamma_n = i\int_{BZ}\mathbf{A}_n(\mathbf{k})\mathrm{d}\mathbf{k} = i\int_{BZ}\langle u_{n,\mathbf{k}}|\nabla_{\mathbf{k}}|u_{n,\mathbf{k}}\rangle\mathrm{d}\mathbf{k}. \tag{2.3}$$

The Berry phase is dependent on the path of the line integral selected in the Brillouin zone (BZ). This is why it is also called the geometric phase [43]. It has been experimentally found in the topological surface states of HgTe [39]. In order to proceed with the topic of topological invariants, it is first necessary to introduce another variable known as the Berry curvature $\mathbf{\Omega}_n(\mathbf{k})$, which corresponds to the curl of the Berry connection $\mathbf{A}_n(\mathbf{k})$:

$$\mathbf{\Omega}_n(\mathbf{k}) = \nabla_\mathbf{k} \times \mathbf{A}_n(\mathbf{k}) = i\nabla_\mathbf{k} \times \langle u_{n,\mathbf{k}} | \nabla_\mathbf{k} | u_{n,\mathbf{k}} \rangle. \tag{2.4}$$

The Berry phase plays a key role in defining the Chern number $\mathcal{C}$, the first topological invariant to be treated here. The **Chern number** $\mathcal{C}_n$ of the nth band is the integral of the Berry-curvature over the Brillouin zone [43]:

$$\mathcal{C}_n = \frac{1}{2\pi} \int_{BZ} \mathbf{\Omega}_n(\mathbf{k}) \cdot \hat{\mathbf{n}} \, \mathrm{d}^2\mathbf{k}, \tag{2.5}$$

with $\hat{\mathbf{n}}$ being the unit normal vector. The integral over the BZ always results in an integer multiple of 2π, so the Chern number $\mathcal{C}_n$ is an integer number. The total Chern number of the system then results from the sum of the Chern numbers of the individual bands and is therefore given by

$$\mathcal{C} = \sum_{n=1}^{N} \mathcal{C}_n. \tag{2.6}$$

Different topological phases can be distinguished by their Chern number $\mathcal{C}$. Interestingly, in the quantum Hall effect, $\mathcal{C}$ appears in the transversal conductivity:

$$\sigma_{xy} = \mathcal{C} \cdot \frac{e^2}{h}. \tag{2.7}$$

The Chern number corresponds to the integer filling factor ν discussed in section 3.1.3, which indicates how many Landau levels are occupied [43]. The ratio e^2/h is the inverse of the von-Klitzing constant, which will be discussed in section 3.1.4.

2.2. Altland-Zirnbauer table

Altland and Zirnbauer introduced a system in 1997 to classify TIs and superconductors according to a periodic table of topological invariants [48]. To do so, initially it is necessary to determine which of the three symmetries – time reversal, particle hole, and chiral – apply to the system. As a result of the different combinations, 10 distinct symmetry classes can be identified. To each of these symmetry classes, for a given dimension, a specific topological invariant can be assigned. A system that has time reversal symmetry but broken particle-hole and broken chiral symmetry belongs to the AII symmetry class. The topological

invariant corresponding to this class in 3D is the $\mathbb{Z}2$ invariant. This invariant can be either 0, which represents topologically trivial, or 1, which represents topologically non-trivial [49–51]. 3D TIs belong into this AII class and are characterized by four $\mathbb{Z}2$ invariants, namely ν_0, ν_1, ν_2 and ν_3 (not to be confused with the filling factor ν). If the first invariant $\nu_0 = 1$, than this describes a special phase, a so-called **strong** TI. An example for such a strong TI is the strained 3D HgTe, the material which is investigated in this thesis [52].

2.3. Bulk-boundary correspondence

TIs, like trivial insulators, are insulating in the bulk. In contrast to these, however, TIs have the previously mentioned gapless conductive states on the surface. These states are a result of the non-trivial topology of the band structure. If a trivial insulator is brought into contact with a TI, the topological invariant must change at the interface. Due to the different topological classifications, this cannot happen without closing the band gap at the interface. Therefore, metallic conductive states arise on the surface of the TI. If the bulk Hamiltonian $\mathcal{H}$ is known, the existence of TSS can be predicted. This is described by the so-called **bulk-boundary correspondence** [43, 49, 53, 54]. The surface states are topologically protected by time-reversal symmetry and exhibit a number of captivating, distinct properties. Firstly, the TSS have a linear energy dispersion, forming a Dirac cone (see figure 2.2 (a)). In contrast to the fourfold degenerate graphene, there is only a single Dirac cone on each of the 6 surfaces of the TI. Additionally, electrons with spin up have opposite momentum compared to those with spin down. In other words, electrons with opposite spins move in opposite directions, as shown in figure 2.2 (b). This phenomenon is known as **spin-momentum locking**. Due to this relationship, back scattering from $\mathbf{k}$ to $-\mathbf{k}$ is prohibited, as the spin would need to be flipped simultaneously [50, 53, 55].

The previous section explained that the AII class of HgTe has time reversal

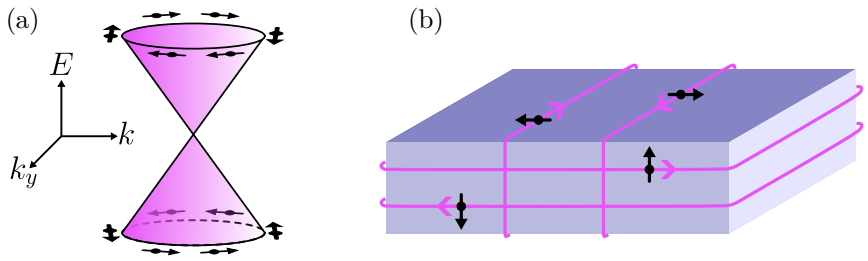

Fig. 2.2.: (a) Dirac-like energy dispersion in k-space of a single surface of the 3D TI. The spins are indicated by black arrows. (b) Real space picture of the conductive 2D surface states (magenta). The states are wrapped all around the insulating 3D bulk material (purple box). Because of spin-momentum locking, the movement of electrons with spin up is in opposite direction to that of electrons with spin down (adapted from reference [55]).

symmetry. However, this symmetry is broken by an external magnetic field. In this thesis, fields of up to 17 T were used, which raises the question of whether this affects the TSS. The answer is that their existence is stabilised by the inverted band ordering, but they are no longer necessarily protected from back scattering [49, 56].

2.4. Band structure inversion of HgTe

Unstrained bulk HgTe is a semimetal composed of the elements mercury and tellurium. While both HgTe and CdTe possess a zincblende crystal structure, only HgTe has an **inverted band structure**. This band structure inversion of HgTe was already experimentally observed in 1976 by Groves et al. [57] using interband magnetoreflection measurements. The exact energies were calculated by Berchenko et al. [58] only a couple of months later [52, 58, 59].

Both CdTe and HgTe have a similar energy gap E_{in} which separates the s-type Γ_6 and p-type Γ_8 bands. The Γ_6 band originates from the cadmium or mercury atoms, while the Γ_8 band originates from the tellurium atoms. Both systems, CdTe and HgTe, can be described by the Hamiltonian $\mathcal{H}_0$. In both cases, the Γ_6 band resides above the Γ_8 band. However, to describe the physical situation accurately, it is necessary to include that the energy bands are altered due to relativistic corrections of the Hamiltonian, as shown in figure 2.3. This occurs because CdTe and HgTe consist of heavy elements with large atomic

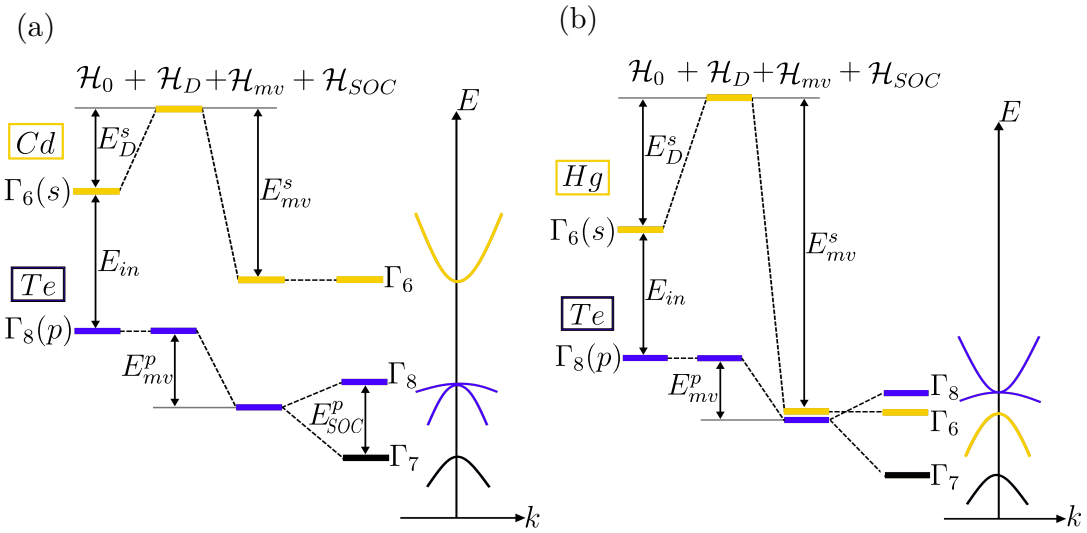

Fig. 2.3.: Relativistic corrections of the CdTe and HgTe band structures. (a) The left part shows the effect of the three terms of $\mathcal{H}_{rel}$ on the Γ_6 (yellow) and Γ_8 (blue) bands in CdTe. The initial energy E_{in} and the relativistic corrections E_D, E_{mv}, and E_{SOC} are indicated. The right part displays a simplified representation of the final energy dispersion. (b) Relativistic corrections of the band structure in HgTe. The final configuration indicates that the Γ_6 band is below the Γ_8 band (adapted from [58]).

numbers, specifically $Z_{\mathrm{Cd}} = 48$, $Z_{\mathrm{Te}} = 52$, and $Z_{\mathrm{Hg}} = 80$. [49, 58, 60]. The total relativistic correction is

$$\mathcal{H}_{rel} = \mathcal{H}_D + \mathcal{H}_{mv} + \mathcal{H}_{SOC}. \tag{2.8}$$

The first summand is the so-called Darwin correction $\mathcal{H}_D$. This is the additional energy due to the interaction of the electrons with the atomic nucleus. The Darwin correction is zero for p-type electrons and finite for s-type electrons. The second summand comes into play because the mass of a particle increases at high velocities. It is therefore called the mass-velocity term $\mathcal{H}_{mv}$. The third summand gives a necessary correction due to the spin-orbit coupling. $\mathcal{H}_{SOC}$ partially lifts the threefold degeneracy of the p-type Γ_8 band. The result, which can be seen in figure 2.3, is a twofold degenerate heavy and light hole Γ_8 band and a split-off Γ_7 band.

The first two summands are significantly larger for HgTe than for CdTe. Therefore, after performing the calculation correctly, the result is that for HgTe the Γ_6 band is below the Γ_8 band and the band structure is inverted, whereas for CdTe the non-relativistic sequence remains [58, 61].

2.5. Topological surface states

As previously explained, a TI enclosed by a trivial insulator results in the formation of TSS at the interfaces. In principle, even vacuum would suffice to give rise to TSS, but in this work, a heterostructure is created by growing HgTe on top of CdTe. The dominant reason for CdTe as the trivial insulator of choice is described in section 2.6.

As explained earlier, in CdTe, the Γ_6 band is located above the Γ_8 band. In HgTe, however, the Γ_8 band is situated above the Γ_6 band. Due to symmetry

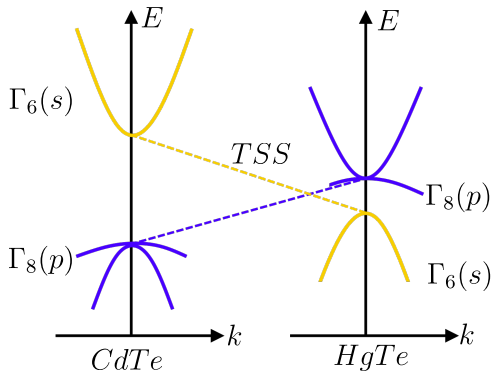

Fig. 2.4.: Emergence of TSS at the CdTe-HgTe interface. Connecting the Γ_8 bands to each other and the Γ_6 bands to each other leads to TSS at the interface of CdTe and HgTe.

reasons it is not possible to continuously transform s-type bands into p-type bands [49]. However, the s-type Γ_6 bands may be connected to each other, as well as the p-type Γ_8 bands. This inevitably leads to the two bands crossing at the interface of the materials and ensures that the **TSS with linear energy dispersion** emerge (see figure 2.4), forming a two-dimensional electron system (2DES) [55].

However, it should be mentioned that the energy dispersion of the TSS in HgTe is not perfectly linear. Due to a hybridization of the TSS with the valence band, the dispersion relation deviates slightly from a linear course and gets an additional, parabolic contribution [59, 62–64].

2.6. Strained HgTe

Growing the HgTe on a CdTe substrate also has an additional, intended effect, as it opens the bandgap in the semimetallic material. The exact lattice constants are $a_{\mathrm{HgTe}} = 0.646\,\mathrm{nm}$ and $a_{\mathrm{CdTe}} = 0.648\,\mathrm{nm}$. The small lattice mismatch of the two zincblende structures is only 0.3 %. Below a critical film thickness of 200 nm, the HgTe takes on the lattice constant of the CdTe. At larger film thicknesses, the HgTe lattice constant relaxes. In this work, only wafers with HgTe thicknesses of 80 nm were investigated, which have been shown to be completely strained by X-ray diffraction measurements [63, 67]. This uniaxial strain in the HgTe **opens a gap** in the Γ_8 bands of the otherwise semimetallic HgTe, as shown in figure 2.5. More precisely, the gap opens up between the

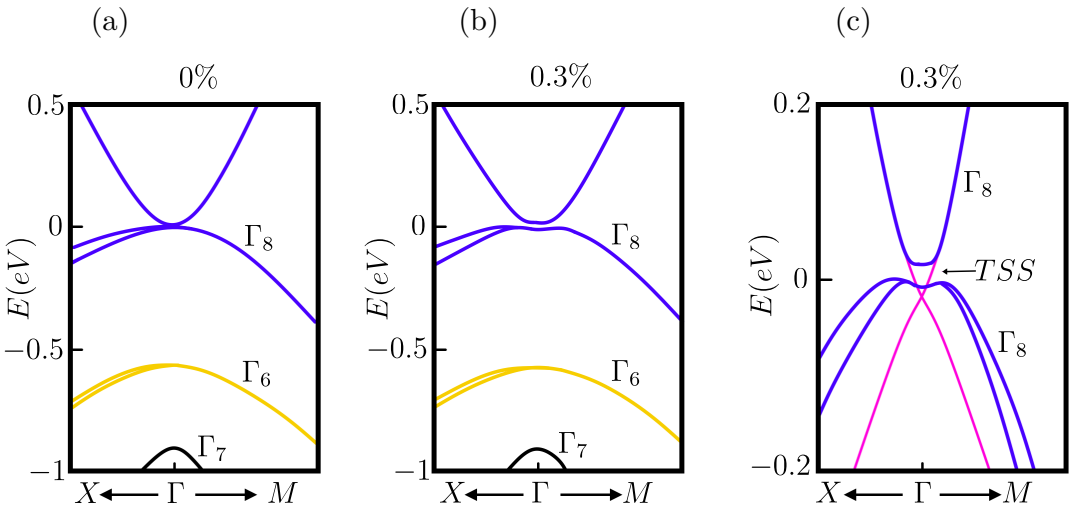

Fig. 2.5.: Band structure of HgTe at different strain values calculated with ab initio methods by Wu et al. [65]. (a) Bulk band structure of HgTe without strain. (b) Bulk band structure of HgTe at 0.3 % strain which opened the band gap between the Γ_8 bands. (c) Close up of the bulk band gap of HgTe at 0.3 % strain and the gapless topological surface states drawn in pink. The Dirac node is buried in the valence band (adapted from [65, 66]).

heavy hole and light hole band of the formerly twofold degenerate Γ_8 band. The bulk HgTe is then insulating and only the non-spin degenerate surface states remain in the band gap. The HgTe is now a TI [59, 63–65]. The gap size at the Γ-point is typically reported to be 15 to 20 meV [67–69].

The experiments in this thesis focus on the electrons of the top and bottom surfaces of the 3D TI, which form two separate 2DESs. When the Fermi energy is in the conduction band, the bulk electrons also contribute. Empirical evidence shows that these also behave like a 2DES. When the Fermi energy is in the valence band, a 2D hole system is observed. This will be demonstrated in chapter 6.

When describing the band structure of strained HgTe, it is important to note that the Dirac point, i. e. the point where the two conical surfaces of the Dirac cone meet, is buried deep in the valence band. At present, it cannot be accessed by transport experiments as the Fermi level cannot be tuned to this region [59, 65].

3. Transport in 2D electron systems

The first section of this chapter describes electron transport in a Hall bar geometry. The Drude model is used to explain the physics at low magnetic fields. At higher magnetic fields, Landau quantization may occur, leading to the quantum Hall effect and Shubnikov-de Haas oscillations. The second section of the chapter covers electric capacitances. Capacitances are usually associated with the dielectric medium between two conducting bodies. However, in systems with a low density of states, such as 2D electron systems, there is an additional contribution from the so-called quantum capacitance. Both magnetotransport and quantum capacitance can provide valuable insights into the physics of the observed sample.

3.1. Magnetotransport

This section's description of the behaviour of electrons in a two-dimensional system subjected to a perpendicular magnetic field equally applies to holes.

3.1.1. Hall bar geometry

In the following, a two-dimensional conducting layer with the Hall bar geometry shown in figure 3.1 is assumed. In the x-direction an electric field E_x is applied with a current density $j_x = \frac{I}{W}$. When a magnetic field B is applied perpendicular to the sample geometry, a Lorentz force acts on the moving charge carriers, resulting in a charge separation. In response, an electric field builds up in the y-direction, and counteracts the Lorentz force until both forces are in equilibrium. The resulting potential difference is the Hall voltage named after Edwin H. Hall [70, 71].

The electric field $\boldsymbol{E}$ and current density $\boldsymbol{j}$ are connected by a 2×2 resistivity tensor $\boldsymbol{\rho}$:

$$\begin{pmatrix} E_x \\ E_y \end{pmatrix} = \begin{pmatrix} \rho_{xx} & \rho_{xy} \\ \rho_{yx} & \rho_{yy} \end{pmatrix} \begin{pmatrix} j_x \\ j_y \end{pmatrix}. \tag{3.1}$$

For symmetry reasons this equation can be simplified with $\rho_{xx} = \rho_{yy}$ and

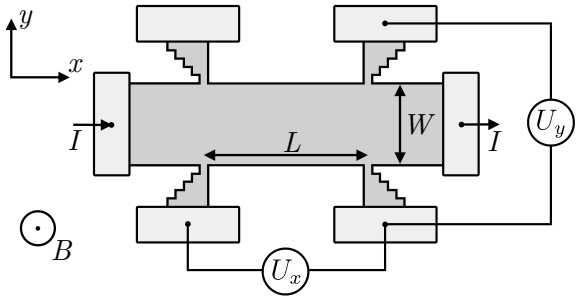

Fig. 3.1.: Hall bar geometry with width W and length L. The current runs in x-direction, the magnetic field points out of the plane. The longitudinal voltage U_x and the transversal voltage U_y can be measured by four-terminal sensing.

$\rho_{xy} = -\rho_{yx}$ [64, 72]. As soon as the system is in the steady-state condition, no current flows in y-direction and $j_y = 0$. Then, equation 3.1 reduces to [71]

$$E_x = \rho_{xx} j_x \quad \text{and} \quad E_y = -\rho_{xy} j_x. \tag{3.2}$$

Experimentally, the **longitudinal** resistivity ρ_{xx} and the **transversal** resistivity ρ_{xy} can be directly obtained in a Hall bar geometry by [72]

$$\rho_{xx} = \rho_{yy} = R_{xx} \frac{W}{L} = \frac{U_x}{I} \frac{W}{L} \tag{3.3}$$

and by

$$\rho_{xy} = -\rho_{yx} = R_{xy} = \frac{U_y}{I}. \tag{3.4}$$

By matrix inversion[1], the conductivity tensor $\boldsymbol{\sigma}$ can be obtained from the resistivity tensor $\boldsymbol{\rho} = \begin{pmatrix} \rho_{xx} & \rho_{xy} \\ -\rho_{xy} & \rho_{xx} \end{pmatrix}$ by

$$\boldsymbol{\sigma} = \frac{1}{\rho_{xx}^2 + \rho_{xy}^2} \begin{pmatrix} \rho_{xx} & -\rho_{xy} \\ \rho_{xy} & \rho_{xx} \end{pmatrix}. \tag{3.5}$$

Vice versa, one can obtain the resistivity tensor from the conductivity with

$$\boldsymbol{\rho} = \frac{1}{\sigma_{xx}^2 + \sigma_{xy}^2} \begin{pmatrix} \sigma_{xx} & -\sigma_{xy} \\ \sigma_{xy} & \sigma_{xx} \end{pmatrix}. \tag{3.6}$$

3.1.2. Diffusive Drude transport

At low magnetic fields, a 2D electron system (2DES) behaves diffusively and can be described with the Drude model, which was published in 1900 and is named after Paul Drude [74]. Once again, the descriptions also apply to a 2D

[1]The inverse $\boldsymbol{A}^{-1}$ of a 2×2 matrix $\boldsymbol{A} = \begin{pmatrix} a & b \\ c & d \end{pmatrix}$ is given by $\boldsymbol{A}^{-1} = \frac{1}{\det \boldsymbol{A}} \cdot \begin{pmatrix} d & -b \\ -c & a \end{pmatrix}$ [73].

hole system (2DHS).

A simple Newtonian equation of motion can be set up, first without magnetic field, where $\boldsymbol{v}$ is the electron velocity and m^* the effective mass. The force acting on an electron with charge e due to the electric field $\mathbf{E}$ is considered. In addition, a friction term is included to provide a phenomenological description of collisions with defects using a mean scattering time τ and a drift velocity $\boldsymbol{v}_d$ [66]:

$$m^* \frac{d\boldsymbol{v}}{dt} = -e\mathbf{E} - \frac{m^*}{\tau}\boldsymbol{v}_d. \tag{3.7}$$

Under the steady state condition $^{dv}/_{dt} = 0$, we directly obtain a solution for the drift velocity:

$$\boldsymbol{v}_d = -\frac{e\tau}{m^*}\mathbf{E}. \tag{3.8}$$

The drift velocity is related to the electric field via a proportionality constant $\mu = {}^{e\tau}/_{m^*}$, which describes the electron mobility. To obtain the current density the charge carrier density n_s is multiplied with the drift velocity [66]:

$$\mathbf{j} = -n_s e \boldsymbol{v}_d = n_s e \mu \mathbf{E}. \tag{3.9}$$

In the second step equation 3.8 was used. Now, we additionally consider a magnetic field perpendicular to the sample geometry in the equation of motion and obtain [66, 71]

$$m^* \frac{d\boldsymbol{v}}{dt} = -e(\mathbf{E} + \boldsymbol{v}_d \times \mathbf{B}) - \frac{m^*}{\tau}\boldsymbol{v}_d. \tag{3.10}$$

Once again the steady state condition is considered and the equations 3.2 are used. Then, one obtains two expressions which connect the experimentally measurable resistivities with the material properties n_s and μ. Firstly, if ρ_{xy} is measured as a function of the magnetic field, the **charge carrier density** can be determined from the slope of the curve by

$$\rho_{xy} = -\frac{E_y}{j_x} = -\frac{B_z}{e n_s}. \tag{3.11}$$

Secondly, once the charge carrier density is known, the electron **mobility** μ can be derived from the zero-field resistivity ρ_{xx} by

$$\rho_{xx} = \frac{E_x}{j_x} = \frac{m^*}{n_s e^2 \tau} = \frac{1}{e n_s \mu}. \tag{3.12}$$

If there is more than one charge-carrier type the situation becomes more difficult: Then a two-carrier Drude model can be employed to describe ρ_{xx} and ρ_{xy} at small magnetic fields. In chapter 6, this approach is employed and

described [64, 66, 71, 72].

3.1.3. Landau quantization

The classical Drude description of the behaviour of electrons is valid for small fields. In the case of large perpendicular magnetic fields, high electron mobility ($\mu B = \omega_c \tau > 1$), and low temperatures ($k_B T < \hbar\omega_c$) the underlying physics changes decisively, and a quantum mechanical description is needed. The cyclotron frequency ω_c refers to the circular motion assumed by the electrons in response to the Lorentz force. The product $\omega_c\tau$ is equal to the number of cyclotron revolutions an electron completes until the next scattering process. Consequently, for $\omega_c\tau > 1$ the electron follows multiple, overlapping circular orbits and interferes with itself [71]. This leads to an additional quantization of the system, termed Landau quantization. The density of states is now split into Landau levels, named after Lew D. Landau [75]. An extensive experimental description of the physical background can be found in reference [72]. A rather theoretical approach is discussed in reference [61].

First, we set up the Schrödinger equation of an electron in a magnetic field [72]:

$$\left[\frac{(\mathbf{p} + e\mathbf{A})^2}{2m^*} + V(z)\right]\Psi = E\Psi. \tag{3.13}$$

The Hamiltonian $\mathcal{H}$ considers the external magnetic field $\mathbf{B}$ via the vector potential $\mathbf{A}$ with $\mathbf{B} = \nabla \times \mathbf{A}$, $\mathbf{p}$ stands for the momentum operator, and $V(z)$ for the confinement potential. As a solution one gets then the following energy eigenvalues [72]:

$$E_n = \hbar\omega_c\left(n + \frac{1}{2}\right) \quad \text{with} \quad n \in \mathbb{N}_0. \tag{3.14}$$

These are similar to the energy eigenvalues of a harmonic oscillator. It is now evident that the Landau levels have a discrete energetic spacing of $\hbar\omega_c$. Moreover, the lowest Landau level lies at $\frac{1}{2}\hbar\omega_c$. The fan-like pattern of LL in an energy E vs magnetic field B plot (or gate voltage V_g vs B), shown in figure 3.2, is also called a Landau fan.

At large magnetic fields, an additional Zeeman term lifts the degeneracy of an initially spin degenerate system. The energy eigenvalues are then given by [72]

$$E_n^{\pm} = \hbar\omega_c\left(n + \frac{1}{2}\right) + sg^*\mu_B B_z \quad \text{with} \quad n \in \mathbb{N}_0, \tag{3.15}$$

where $s = \pm 1/2$ is the spin quantum number, g^* is the Landé g-factor, and μ_B is the Bohr magneton. Landau levels are highly degenerate. The degeneracy n_{LL} is directly proportional to the magnetic field and given by

$$n_{\mathrm{LL}} = g_s\frac{eB}{2\pi\hbar}, \tag{3.16}$$

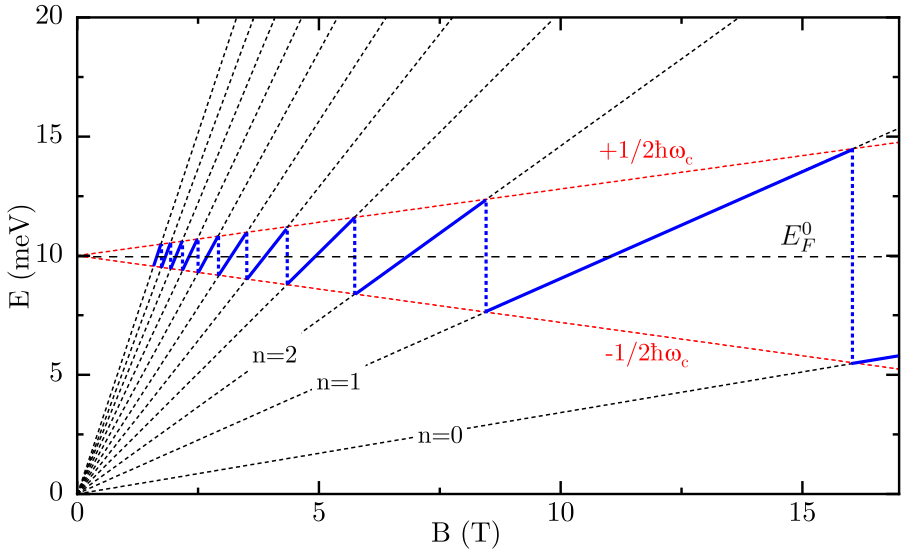

Fig. 3.2.: Oscillations of the Fermi energy E_F (blue) as a function of the magnetic field B. The Landau levels are drawn as black, dashed lines originating at 0 T. Spin degeneracy is neglected here. E_F^0 indicates the zero field Fermi energy. With increasing magnetic field, both the energy spacing between two Landau levels ($\hbar\omega_c$) and the Landau level degeneracy n_{LL} increase. Thus, more states per Landau level can be occupied by electrons. If one assumes a constant charge carrier density then at certain magnetic field values the highest occupied LL is depopulated and the Fermi energy falls to the next Landau level below. This leads to oscillations of the Fermi energy which are $1/B$ periodic (adapted from [76]).

with g_s standing for the spin degeneracy factor. The number of occupied, spin resolved ($g_s = 1$) Landau levels is called the **filling factor** ν. It can be calculated by the ratio of occupied states n_s to the Landau level degeneracy n_{LL} with

$$\nu = \frac{n_s}{n_{\mathrm{LL}}} = n_s \left(\frac{eB}{2\pi\hbar}\right)^{-1}. \tag{3.17}$$

Furthermore, the magnetic flux quantum $\Phi_0^m = h/e$ can be introduced here. Eventually, one obtains [72]

$$\nu = n_s \left(\frac{B}{\Phi_0^m}\right)^{-1} = n_s A \left(\frac{\Phi}{\Phi_0^m}\right)^{-1}. \tag{3.18}$$

In the second step, the magnetic field B is replaced by the magnetic flux Φ per area A with $B = \Phi/A$. The total number of electrons is given by $n_s A$ and the total number of magnetic flux quanta is equal to Φ/Φ_0^m. Consequently, the filling factor ν also represents the number of electrons per magnetic flux quantum in the same area.

Until now, Landau levels were assumed to be δ-function shaped peaks. In reality, however, Landau levels are broadened due to disorder and inhomogeneities. This leads to the so-called **localized** and **extended** states (see grey areas in

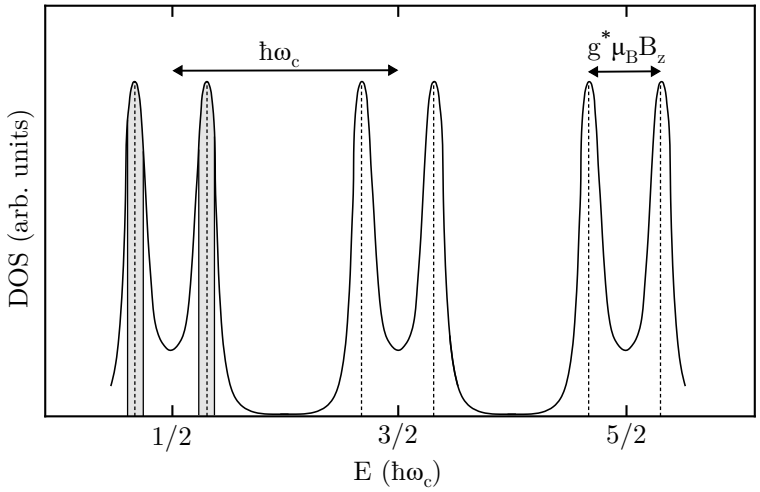

Fig. 3.3.: The density of states (DOS) versus energy E for spin-split Landau levels (solid line). Without the energy broadening discussed below, the Landau levels would consist of δ-function shaped peaks. These are drawn as vertical dashed lines, which also simultaneously index the centres of the broadened Landau levels. The spacing of the Landau levels is $\hbar\omega_c$, the spacing resulting from the spin splitting is $g^*\mu_B B_z$. For the first spin-split Landau level, the regions with extended states are additionally highlighted in grey (adapted from [71]).

figure 3.3). The extended states sit close to the centre of the Landau levels [66, 77]. A way to distinguish between Landau and Zeeman gap is the following: Landau level splitting happens only in a magnetic field perpendicular to the sample geometry. Zeeman splitting also occurs in parallel fields.

3.1.4. Phenomenological picture of QHE and SdH

The occurrence of Landau levels in the system leads to two related effects which shall be discussed here. The first is the quantum Hall effect (QHE). It was first published in 1980 by Klaus von Klitzing et al. [16]. In 1985, he received the Nobel Prize for its discovery [17]. The transverse resistance ρ_{xy} as a function of the magnetic field shows **plateaus** with well defined resistance values

$$\rho_{xy} = \frac{R_\mathrm{K}}{\nu} \quad \text{or} \quad \sigma_{xy} = \frac{\nu}{R_\mathrm{K}}, \tag{3.19}$$

where $R_\mathrm{K} = h/e^2$ is the von-Klitzing constant and ν represents an integer number that corresponds to the filling factor[2]. Intriguingly, the plateau values are independent of the sample geometry or sample size and do not depend on material properties.

In 2018, seven natural constants were defined to a fixed value. This was done with the aim of providing a basis for a generally applicable redefinition of the SI units. Among other things, the values for e and h were defined and thus

[2] ν also corresponds to the Chern invariant $\mathcal{C}$, as mentioned in section 2.1.

R_K is also assigned a fixed, exact value of 25 812.807 45 [...] Ω [78].

Furthermore, it can be observed that the longitudinal resistivity oscillates as a function of the inverse magnetic field. The ρ_{xx} curve shows flat minima whenever a plateau is seen in ρ_{xy}, and peaks whenever ρ_{xy} changes its value. This is called Shubnikov-de Haas (SdH) effect and was observed by the two physicists Lev Shubnikov and Wander J. de Haas (see reference [79]).

Figure 3.4 shows an example of a QHE and a SdH measurement. One can clearly see the SdH peaks and the QHE plateaus. It should be mentioned, that the graph shows measurements on a more complicated system. However, at high magnetic fields this system behaves as described in this section and is therefore sufficient to illustrate the described physics.

The SdH oscillations are **related to the carrier density** n_s. Using equation 3.17 and replacing $2\pi\hbar$ by h it follows for spin-resolved systems, that

$$n_s = \frac{e}{h}\frac{\nu}{\frac{1}{B}}. \tag{3.20}$$

The charge carrier density is obtained experimentally from the distance between two successive SdH minima [72]:

$$\nabla\left(\frac{1}{B}\right) = \frac{1}{B_{i+1}} - \frac{1}{B_i} = \frac{|e|}{hn_s}. \tag{3.21}$$

In chapter 6 this equation is applied intensively. There, the described $1/B$ periodicity is also used to determine the carrier density from SdH oscillations originating from holes and from measurements of the sample capacitance.

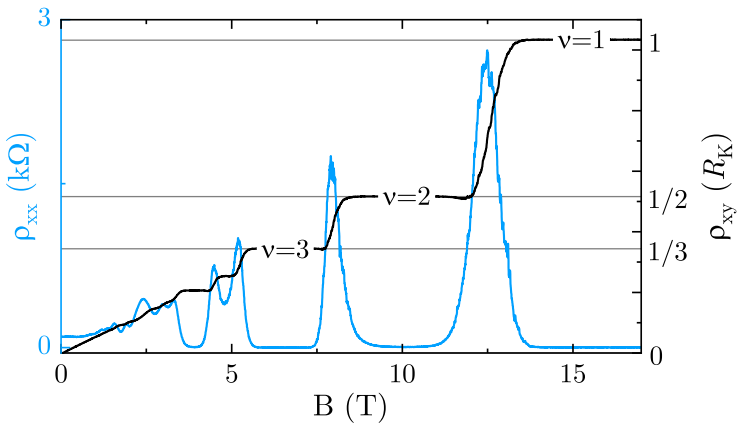

Fig. 3.4.: QHE and SdH oscillations. The QHE (black) is typically observed in the transverse resistance ρ_{xy} as a function of the magnetic field B, which exhibits plateaus at R_K/ν. The plateaus corresponding to the filling factors $\nu = 1 - 3$ are labelled and indicated by grey lines. The Shubnikov-de Haas effect (blue) is observed in the longitudinal resistance, ρ_{xx}. It drops to zero when plateaus are visible in ρ_{xy} and exhibits peaks when ρ_{xy} makes a step.

Besides the integer QHE, there is also the fractional quantum Hall effect (FQHE) [80]. The FQHE exhibits plateaus corresponding to fractional ν. However, this topic will not be discussed in this thesis.

3.1.5. Microscopic picture of QHE and SdH

The following section is based on an article by Jürgen Weis [77] and the doctoral theses of Andreas Gauss [81] and Maximilian Kühn [82]. It provides only a brief overview of the microscopic picture of the quantum Hall effect. The detailed picture can be found in the references.

Initially, the edge channel model was used to explain the appearance of the quantum Hall plateaus and the SdH oscillations. The electrons follow a cyclotron orbit due to the magnetic field. At the edge of the sample, electrons are reflected and cannot complete their circular motion. Therefore, they move along the edge. This picture is called skipping orbits. As a consequence, the current flow takes place entirely at the edges of the sample in 1D channels [83, 84].

In contrast to this, it has been demonstrated that the current flow is not restricted to the edges of the sample, but also flows within the bulk[3] of the sample. There are distinct current distributions, each corresponding to a Hall potential profile, i. e. the profile of the voltage drop over a cross-section of the Hall bar. This was shown experimentally with scanning force microscopy on GaAs [85, 86] and theoretically underpinned using self-consistent calculations of the electrostatic potential from the electron density [87, 88]. These results strongly contradict the edge-channel picture. Instead, the behaviour is described with a landscape consisting of electrically compressible and incompressible regions. This is displayed in figure 3.5 (a) and (b). The compressibility κ is defined as [89]

$$\kappa^{-1} = n_s^2 \frac{\delta\mu}{\delta n_s}, \tag{3.22}$$

where n_s is the charge carrier density and μ is the chemical potential, i. e. the Fermi energy at $T = 0\,\mathrm{K}$.

Within **incompressible** regions, the Fermi energy E_F lies between two Landau levels, i. e. in a Landau gap. The LL below are completely occupied, the LL above are unoccupied, resulting in an integer filling factor. As there are no available states at the Fermi energy, the electrons cannot rearrange themselves. Consequently, an electrostatic potential gradient cannot be screened and the resulting behaviour is similar to that of an insulator. The local conductivity σ_{xx} is equal to zero [81]. In **compressible** regions, the Fermi energy E_F lies in a LL, resulting in a non-integer filling factor. The electrons can now screen

[3] The term bulk refers to the interior area of a 2D electron system here. Not to be confused with the bulk of the 3D HgTe.

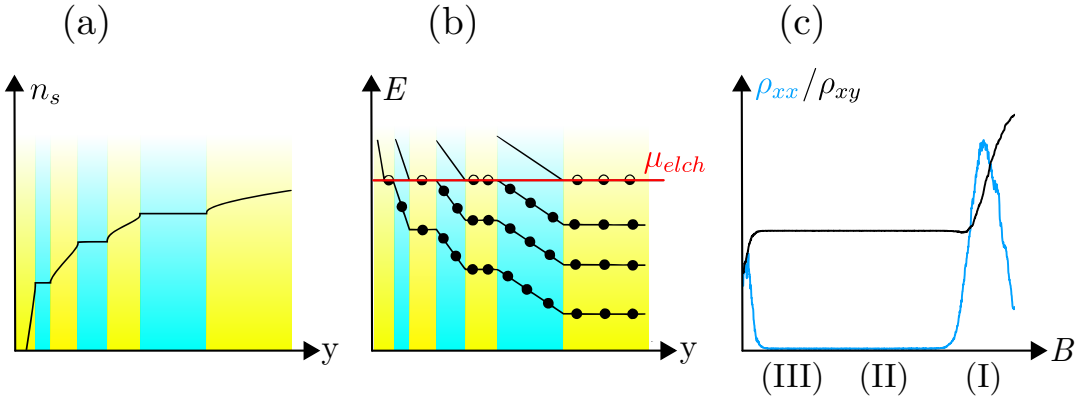

Fig. 3.5.: Compressible and incompressible regions in the QHE. The figures (a) and (b) show electrically compressible and incompressible regions in a semi-infinite 2DES, assuming a one-sided confinement by an in-plane metallic gate located at negative y-values. It is energetically favourable to have alternating strips of compressible (yellow) and incompressible (cyan) regions. (a) In the compressible strips, E_F lies in a partially filled LL, enabling an increase in the charge carrier density n_s. Once the LL is filled, no free states are available, and an incompressible strip is observed where n_s remains constant. A significant quantity of chemical energy μ would be required to occupy the second LL. (b) Instead, it is energetically more favourable to bend the LLs downwards below the electrochemical potential μ_{elch}. Only once the next LL intersects with μ_{elch} this LL will be filled, causing n_s to increase again. (c) Within one quantum Hall step's magnetic field interval, three fundamentally different current distributions emerge. These are indicated with Roman numerals and elaborated in the main text (Figure (a) and (b) adapted from reference [82], calculations by Chklovskii et al. [87].).

variations of the electrostatic potential, which is therefore constant in these regions. A finite local conductivity σ_{xx} is obtained.

Assuming a Hall bar and an electrochemical potential difference between its current contacts, the compressible strips carry the electrochemical potential μ_{elch}[4] of the source and drain along opposite edges of the sample, resulting in a Hall voltage. If there is a plateau in the transversal resistance, a **dissipationless current** flows along the Hall bar in the incompressible regions, i. e. along the x-direction in figure 3.1. If ρ_{xx} is measured using the longitudinal 4-point contacts, the result is zero as there is no dissipation[5]. If there is a Hall plateau step in the transversal resistance, i. e. if ρ_{xy} increases linearly, then dissipation takes place in the Hall channel and peaks can be seen in ρ_{xx}. The dissipationless flow of the Hall current is a property of the Hamiltonian's eigenfunctions [77]. This can also be understood as the current is being carried by the incompressible regions. In these regions, there are no free states at the Fermi energy, so no scattering can take place. On the other hand, in compressible regions, scattering processes occur, leading to dissipation [90].

[4] μ_{elch} considers the chemical potential and the local electrostatic single-electron energy and is assumed to be constant over the whole 2DES ($\mu_{elch} = \mu(\mathbf{r}) - e\Phi(\mathbf{r}) = \text{const.}$) [85].
[5] There is still dissipation at both current contacts at the end of the Hall bar [77].

When examining the cross section of the LL in a 2DES with an electric field in the y-direction E_y[6], the LL are bended due to the Hall voltage. This results in a drift in the x-direction and generates the Hall current density j_x [77, 85]:

$$j_x = \nu \frac{e}{h^2} E_y. \tag{3.23}$$

It can now be seen that **all occupied LL contribute** to the Hall conductivity $\nu \cdot e/h^2$. The current integrated over the width of the Hall bar is [77, 91]

$$I_x = \nu \frac{e^2}{h} U_y. \tag{3.24}$$

The quantized Hall resistance occurs when the Hall voltage U_y drops solely over incompressible regions with the same filling factor within the sample cross-section [77]. With the equation $\rho_{xy} = U_y/I_x$, the known values of the quantum Hall plateaus are obtained (see equation 3.19).

It is important to note that in very pure samples, the Hall plateaus become narrower. Robust quantum Hall plateaus arise due to disorder or inhomogeneities, such as static potential fluctuations or electron depletion at the edge of the sample [77]. Additionally, it should be mentioned that in the QHE regime, the resistivities ρ_{xx} and ρ_{xy}, as well as the conductivities σ_{xx} and σ_{xy}, are local quantities due to the inhomogeneity of the sample. However, in this thesis, the values are calculated using the equations from section 3.1.1 and are considered as averages over the sample geometry.

For a Hall bar based on GaAs, there are three magnetic field ranges that can be distinguished based on the **current distribution**. These are numbered using Roman numerals and their positions within the Hall plateau are depicted in figure 3.5 (c). The order progresses from small to large magnetic fields, and from (III) to (I), respectively.

(III) The **edge-dominated quantum Hall regime** - at the plateau, coming from low magnetic fields. The 2DES exhibits mostly compressible behaviour except close to the edges where it becomes incompressible. The Hall voltage drops and the dissipationless current flows at these edges, causing ρ_{xx} to drop to 0 and ρ_{xy} to assume a constant value.

Within a plateau, the incompressible strips widen and move towards the centre of the Hall bar as the magnetic field increases.

(II) The **bulk-dominated quantum Hall regime** - at the plateau, towards higher magnetic fields. The incompressible strips merge in the centre of the Hall bar, resulting in an incompressible bulk. Hence, the Hall voltage drops in the bulk and the current flows in there. In contrast to the edge channel picture, there is no current at the compressible edges.

[6]This assumes the orientation of figure 3.1.

(I) The **classical Hall regime** - at the centre of the LL, off-plateau region. There is a linear drop in Hall voltage over the entire sample width. The current is now dissipative and flows over the entire sample width. The 2DES is fully compressible, while ρ_{xx} is finite and ρ_{xy} increases linearly.

This described development of the Hall potential drop and the current distribution is repeated for each plateau. The magnetic field affects the compressible/incompressible landscape within each plateau, but this is not reflected in the integral current I_x and relation 3.24 remains stable. In the fully compressible classical Hall regime, there is no quantization in ρ_{xy}.

3.2. Capacitance

The experimental part of this thesis investigates the capacitance of a topgate-insulator-mesa structure. This capacitance is made up of two components: The first is the geometric capacitance, which is associated with the dielectric medium. The second is the quantum capacitance, which is of greater interest as it directly reflects the thermodynamic density of states.

3.2.1. Geometric capacitance

For a metal-insulator-metal plate capacitor the geometric capacitance C_{geo} is determined by

$$C_{geo} = \epsilon_r \epsilon_0 \frac{A}{d}, \tag{3.25}$$

where ϵ_r is the relative permittivity, ϵ_0 is the vacuum permittivity, A is the overlap area of the plates and d is their separation. The calculation of the area A involves determining the overlap of the plates, as illustrated in figure 3.6 (a).

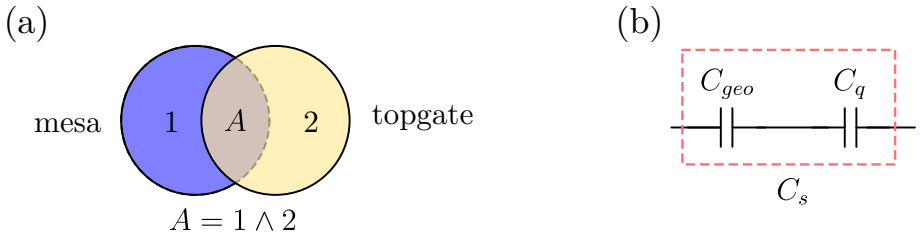

Fig. 3.6.: Overlapping area A and series capacitance of C_{geo} and C_q. (a) The area of overlap between two parallel plates 1 and 2 of a capacitor, which are placed closely together ($d << A$), is denoted by A. In the Boolean algebra terminology A is determined by the conjunction of plate areas $1 \wedge 2$. The geometric capacitance determined by equation 3.25 only takes this area into account. The capacitor plates in the experimental part of this thesis are composed of mesa and topgate. (b) The series connection of geometric capacitance and quantum capacitance results in the sample capacitance C_s.

The total geometric capacitance of multiple insulating layers $\mathcal{N}$ stacked between two metal plates can be calculated by the series connection of the individual capacitances $C_{geo,\,i}$ using

$$\frac{1}{C_{geo,\,tot}} = \sum_{i=0}^{\mathcal{N}} \frac{1}{C_{geo,\,i}}. \tag{3.26}$$

Moreover, C_{geo} is related to the voltage drop ΔV_{geo} by

$$\Delta V_{geo} = \frac{\Delta Q}{C_{geo}}, \tag{3.27}$$

which shows that an additional charge $\Delta Q = e\Delta N$ is drawn into the system by ΔV_{geo}. Here, e is the elementary charge and ΔN represents the number of carriers.

3.2.2. Quantum capacitance

In 1987, Serge Luryi described the role of a 2DES (two-dimensional electron system) in a metal-insulator-2DES structure. Luryi stated that the 2DES functions as an additional capacitor in series to the geometric capacitance [92]. This was preceded by Kaplit and Zemel in 1968, who used capacitance measurements to observe Landau levels in a 2DES [93]. Altering the electron density

$$\Delta n = \frac{\Delta N}{A} = \frac{\Delta Q}{Ae} \tag{3.28}$$

in a system with a low density of states $D(E)$ also affects the chemical potential μ, as the states are filled with electrons:

$$\Delta\mu = \frac{\Delta n}{D(E)} = \frac{\Delta Q}{Ae \cdot D(E)}. \tag{3.29}$$

A variation in the chemical potential $\Delta\mu$ involves a voltage change [94]:

$$\Delta V_q = \frac{\Delta\mu}{e} = \frac{\Delta Q}{Ae^2 \cdot D(E)}. \tag{3.30}$$

The denominator $Ae^2 \cdot D(E)$ is then referred to as the quantum capacitance C_q. It is crucial to understand that the quantum capacitance is only finite for systems with a low thermodynamic density of states. For systems with a high density of states, such as metals, the addition of charge carriers will not significantly alter the chemical potential. This results in a negligible ΔV_q, and therefore an infinite C_Q. However, in order to affect the capacitance of the sample C_s, the quantum capacitance must be sufficiently small. This can be seen from the following derivation. The total voltage change, ΔV, is the sum of ΔV_{geo} and

ΔV_q:

$$\Delta V = \Delta V_{geo} + \Delta V_q. \tag{3.31}$$

Equations 3.27 and 3.30 provide the necessary expressions for these voltage quantities. Along with the expression for the sample capacitance $C_s = \Delta Q/\Delta V$, one obtains

$$\frac{\Delta Q}{C_s} = \frac{\Delta Q}{C_{geo}} + \frac{\Delta Q}{Ae^2 \cdot D(E)}. \tag{3.32}$$

This directly shows that C_s is the **series capacitance** of C_{geo} and C_q:

$$\frac{1}{C_s} = \frac{1}{C_{geo}} + \frac{1}{C_q}. \tag{3.33}$$

The corresponding circuit diagram is shown in figure 3.6 (b). Moreover, it is evident that for a system with an infinite density of states, i. e. an infinite C_q, the sample capacitance C_s is reduced to C_{geo}. For this reason, for thick metal layers, capacitance measurements will solely show the geometric capacitance. Furthermore, in actual measurement setups, so-called parasitic capacitances are unavoidable. These will be addressed in section 5.2.1.

When measuring the capacitance of a topgate-insulator-mesa structure in a sample based on HgTe, the primary observation is the density of states of the **top surface** of the 3D TI [39]. Consequently, Landau quantization of the top surface can be observed in the capacitance by applying a magnetic field perpendicular to the sample geometry. The experimental part of this thesis comprehensively presents and thoroughly discusses data related to this phenomenon.

As a final remark of this section, it should be noted that capacitance directly measures the thermodynamic density of states at the Fermi energy, which includes the localized states. In transport experiments, only the extended states contribute to the longitudinal conductivity σ_{xx}. Furthermore, σ_{xx} is proportional to the second order of the modulated density of states [95]. This explains why σ_{xx} exhibits sharp peaks, while the capacitance displays wide oscillations.

4. Sample fabrication methods

This section describes the wafer material used and the fabrication process that enables transport and capacitance measurements. First, a small fragment, now called sample, is broken out of the wafer. A Hall bar geometry is then etched into the sample to enable carrying out four-point measurements. Following this, two layers of electrical insulators are applied to cover the entire sample area. Finally, a metallic electrode is deposited which overlays the Hall bar. This topgate allows tuning of the Fermi energy within the band structure and is utilized for capacitance measurements.

For all processes, it is essential to ensure that a temperature of 100 °C is not exceeded. At higher temperatures there is always the danger of diffusion effects of the mercury, which would make the sample unusable for the experiments [96].

Comprehensive explanations of sample fabrication are contained in previously published works by Johannes Ziegler and Hubert Maier [64, 66]. Consequently, only the most relevant aspects will be covered here. Appendix A features a list showing all individual steps of sample fabrication. This includes the specific chemicals used and other items relevant to the processes.

4.1. Wafer material

All HgTe wafers, which were used in this work, were grown in the Rzhanov Institute of Semiconductor Physics, Novosibirsk. For the experiments in chapter 6, the n-doped wafer with the number 190301 was used. Figure 4.1 (a) displays the material system which comprises of individual layers with specific thicknesses[7]. First, a 30 nm thick ZnTe layer is deposited on top of (013)-oriented 400 µm of GaAs using molecular beam epitaxy. This is succeeded by a $5-6$ µm thick CdTe layer. As described in section 2.6, the CdTe induces strain into the subsequent 80 nm thick HgTe layer, which opens the gap within the band structure. Additionally, two 20 nm thick $Cd_xHg_{1-x}Te$ buffer layers enclose the HgTe. This enhances the electron mobility μ of the system by an order of magnitude and reduces the bulk impurity concentration [68, 97]. Moreover, the $Cd_xHg_{1-x}Te$ buffer layers are heavily n-doped with indium atoms. The doping extends to a thickness of 10 nm within each buffer layer. The bulk density of the indium

[7] The information on the thicknesses of the individual layers of the wafers was obtained from a private conversation with N. N. Mikhailov.

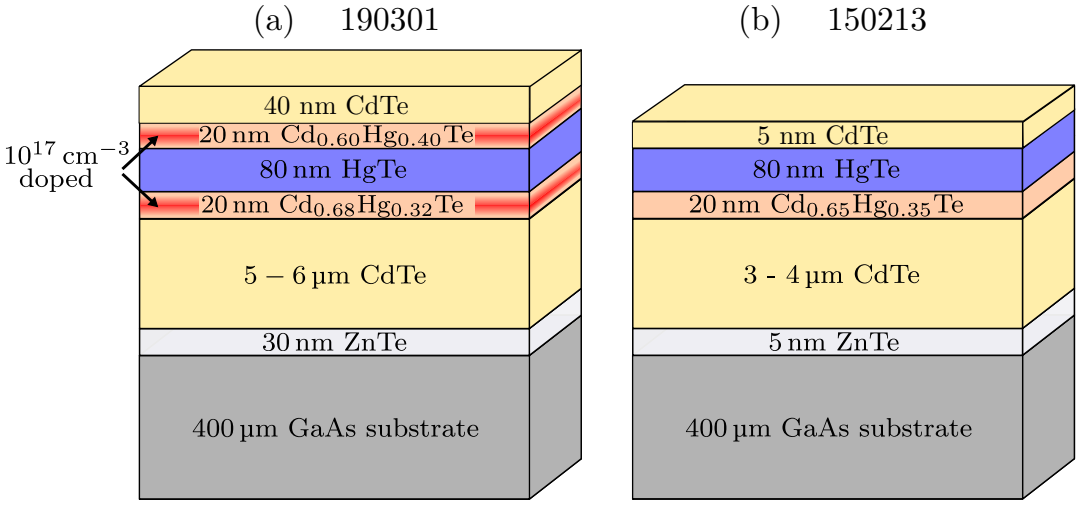

Fig. 4.1.: Cross section, not to scale, of the wafers with numbers 190301 and 150213. (a) The HgTe is sandwiched by symmetrically doped $Cd_xHg_{1-x}Te$ buffer layers. The doping is indicated in red. Below is an explanation and description of the individual layers. (b) The wafer has a similar structure, but has a very thin CdTe cap layer and is not doped.

atoms is $1 \times 10^{17}\,\mathrm{cm}^{-3}$. This increases the electron density within the HgTe and alters the electrostatics of the system. The wafer structure is closed with a 40 nm CdTe cap layer.

For the experiments in chapter 8, the wafer with number 150213 was used. It has a similar structure and is depicted in figure 4.1 (b). However, there are some notable differences: firstly, there is no modulation doping. Secondly, the $Cd_xHg_{1-x}Te$ buffer layer above the HgTe is absent, and the CdTe cap layer thickness is significantly thinner at only 5 nm. This wafer was the preferred choice for fabricating samples with Nb antidots as the cap layer had to be removed to create direct contact between Nb and HgTe. A thinner cap layer is more easily removed using the available etching processes. Furthermore, it also enables the lift-off process described in section 4.3.

4.2. Hall bar etching

First, the wafer is broken into samples of a suitable size of about 4 x 4 mm. The conducting HgTe is partially etched, leaving only the shape of a Hall bar and its associated electrical contacts. This is depicted in figure 4.2.

After cleaning the sample, a resist sensitive to ultraviolet (UV) light is dripped onto it. By so-called spin coating, i. e. fast mechanical rotation of the sample, the resist is evenly distributed and gets a largely homogeneous layer thickness. Subsequent heating of the sample at 80 °C, the baking, hardens it. The hardened resist is then exposed to UV light by means of optical lithography. Between the UV lamp and the sample is a transparent, photolithographic quartz

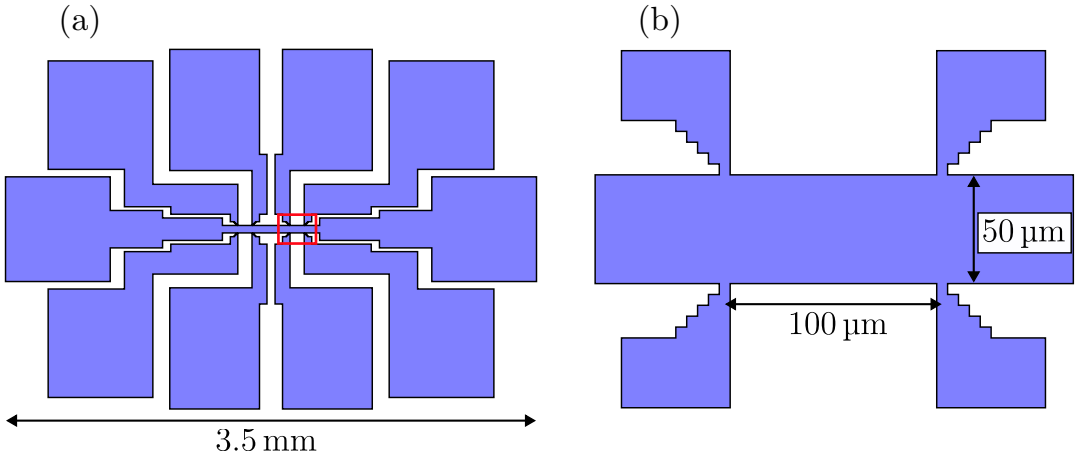

Fig. 4.2.: (a) Typical sample design from a bird's eye view. The mesa measures approximately 3.5 mm x 2.5 mm. Ten contact pads are visible at the edges, each with an approximate size of 700 µm x 700 µm. During the measurement, current runs through two of the contacts, and a four-point voltage can be measured at the remaining eight contacts. All contacts lead to the sample centre, where two Hall bar structures are available for experiments. (b) Enlargement of the image section indicated with a red rectangle on the left displays a typical Hall bar. As illustrated in figure 3.1, the current typically goes through the left and right contacts, and the upper and lower ones function as voltage taps.

glass mask. A layer of chromium on the mask obstructs UV light in certain regions. It serves as a template pattern for the photosensitive resist. Thus, only certain structures of the resist are exposed to UV light, which causes the long-chain polymers of the resist to be broken down into shorter structures. Subsequent chemical development of the resist causes the exposed short-chain structures to dissolve and only the unexposed resist remains [98]. The absolute limit of the resolution of this system is determined by the wavelength of the UV light. However, based on experience, structures a few micrometers in size can be fabricated. The desired shape, specified by the template of the chromium-plated mask, is that of a Hall bar with large contact fields.

The remaining resist then serves as protection for the subsequent etching process. **Wet chemical etching** with bromine has proven to be more advantageous than dry etching with argon ions. The latter significantly reduces the mobility of the electrons in the HgTe [64, 99]. In the more careful wet chemical etching, the sample is immersed in a solution of bromine, ethylene glycol and water at 0 °C. A steady temperature is a prerequisite for a constant etching rate [100]. After an experimentally determined time of 4 min, approximately 200 nm of the wafer are removed by etching. This is sufficient to remove the cap layer and the HgTe and allows electrical current to flow only in the designated areas defined by the mask. After the resist layer has been chemically removed, the etching depth can be confirmed by measuring the surface profile and thus unwanted current paths can be excluded.

4.3. Antidot fabrication

This section describes the procedure used to fabricate superconducting niobium (Nb) antidots on the HgTe Hall bar, which are investigated experimentally in chapter 8. As the fabrication of the antidots posed a major challenge, the individual steps and difficulties are described in detail. Benedikt Kopyciok, Marcel Hild and Lukas Rupp investigated various ways of building antidots as part of their theses, making a noteworthy contribution to the success of the project. For the experiments described in chapter 6, this fabrication step was omitted, and the topgate was deposited directly.

Recipes were optimized based on three different resists: chemical semi-amplified resist (CSAR), polymethyl methacrylate (PMMA), and Allresist-negative 7520 (AR-N 7520). In all three cases, the resist was exposed using electron beam lithography (EBL). The major advantage of using EBL over optical lithography is its significantly higher resolution limit. However, this is not given by the de Broglie wavelength of the electrons, which is approximately 7 pm at an acceleration voltage of 30 kV [101]. Rather, the forward scattering of the electrons in the resist and backscattering from the substrate beneath the resist play significant roles [102]. As a result, the actual resolution is well below the de Broglie wavelength. In this doctoral thesis, antidots with a diameter of 40 nm have been realized.

In figure 4.3 the individual steps of the antidot fabrication are sketched. As a first step, (a) an electron-sensitive **resist is applied** to the sample. Spin coating ensures that the resist becomes uniformly thick. The resist is then baked to evaporate the solvents. (b) Next, the resist is **exposed by EBL** and immersed in a (c) **developing chemical**. This removes part of the resist and only circular resist columns remain. After the resist development step, the CdTe cap layer is removed, followed by the metallisation. Both of these processes take place in situ[8] in an UHV chamber, i. e. without exposure to air in between the processes. (d) The **CdTe layer is removed** with Ar^+-etching. However, this does not only remove the CdTe layer but is also prone to harm the resist. To avoid this problem, it is necessary to minimise the exposure to etching as much as possible. This was accomplished by using a wafer with a thin CdTe cap layer. This thin cap layer was the decisive factor why wafer number 150213 with only 5 nm of CdTe was used for the samples with antidots. (e) 3 nm of Titanium (Ti) are evaporated using an electron gun and then deposited onto the sample. This serves as a seed layer for the following Nb deposition and enhances the HgTe-Nb interface quality [104]. The **Nb is deposited** via Ar^+-sputtering, which involves accelerating argon ions towards a Nb target. During the collision, these ions detach parts of the target, which are subsequently deposited on the sample. Initially, attempts were made to work with a layer thickness of

[8] Latin, meaning "on site" [103]

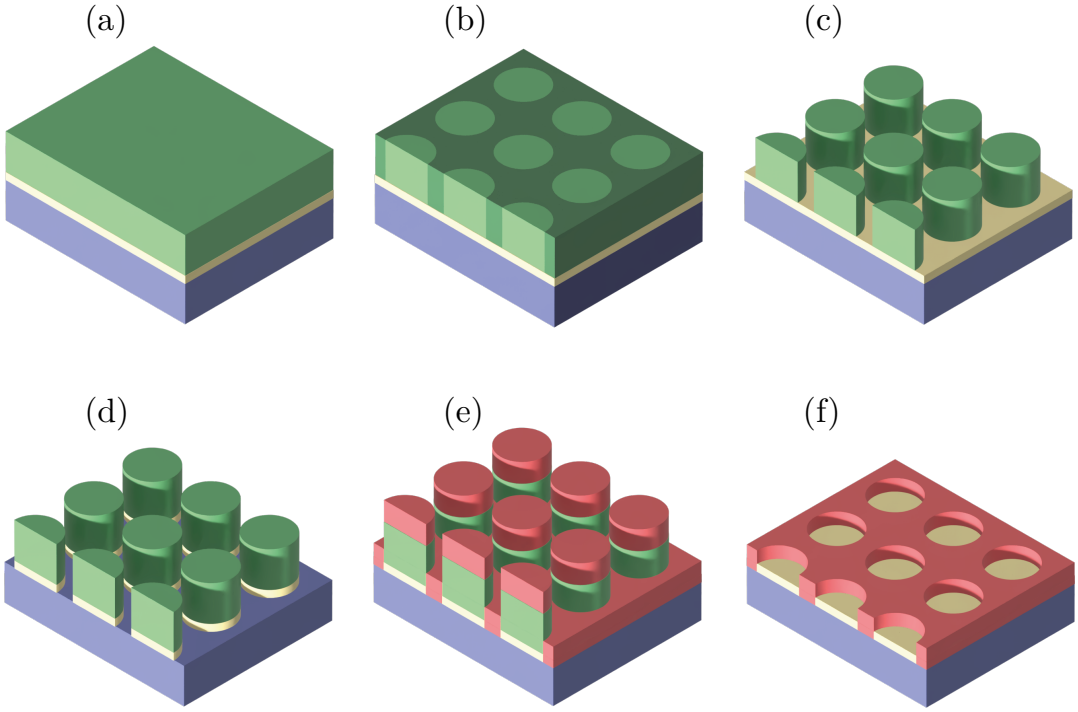

Fig. 4.3.: Schematic illustration of the sequential fabrication steps for Nb antidots on an HgTe wafer. The figures are not to scale. (a) Resist application: The heterostructure consisting of HgTe (purple) and CdTe (yellow) is coated with an electron sensitive resist (light green). (b) Example of electron beam lithography on a positive resist: The regions where Nb is intended to remain in the final sample are exposed with EBL (slightly darker green). (c) Resist development: The exposed areas of the resist are removed through chemical development. Only the periodically arranged resist columns remain. Any possible undercut of the resist is not displayed here. (d) Ar^+-etching: The CdTe layer is removed in areas not covered by resist using argon ions. This is followed by (e) metallization in ultra-high vacuum (UHV), where 3 nm Ti, 30 nm Nb and 3 nm Pt (shown in red) are deposited on the HgTe and on the resist columns. (f) In the lift-off step, the resist columns and the overlying metals are removed using a remover chemical and the mechanical force of an ultrasonic bath. The final result is a layer with holes arranged in a periodic pattern, the antidots (Figure has been created with the support of Benedikt Kopyciok.).

100 nm, but this significantly decreased the probability of a successful lift-off. Thinner layers of approximately 30 nm were found to be successful. Finally, 3 nm of platinum (Pt) were deposited with an electron gun to minimise potential oxidation effects on the surface of the Nb [105, 106]. During metallization, the Ti-Nb-Pt layer adheres to both the wafer and to the resist. In the (f) **lift-off** process, a chemical removes the remaining resist columns with the Ti-Nb-Pt layer on top. The chemical can be sprayed onto the sample under pressure using a syringe, and the sample can be placed in the chemical in an ultrasonic bath. These extra mechanical components have been found to be necessary for a successful lift-off.

The final step is a meticulous documentation and inspection of the results.

Scanning electron microscopy (SEM) is used to observe the finished antidots and capture images, as shown in figure 4.4. This is necessary to confirm the success of the lift-off and to document the diameter and shape of the antidots. These variables depend on various process parameters, including the exposure dose. They can vary considerably, as even minor influences result in significant variations. Only the periodicity of the antidots is reliably given by the lithographic data file.

Regarding the used resist a distinction can be made between positive resists

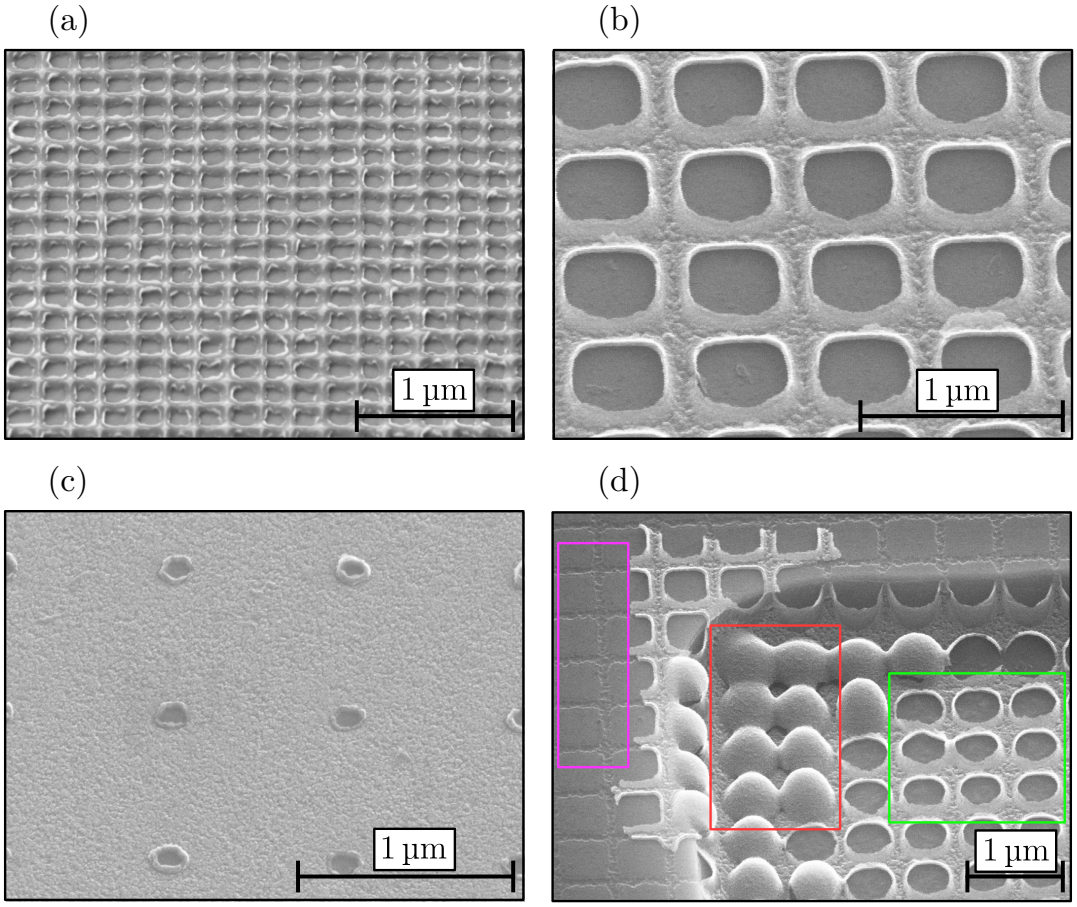

Fig. 4.4.: Scanning electron microscope (SEM) images of Nb antidots on HgTe samples after the lift-off step. To provide optimal visualisation of the structures, the images have been taken at an inclined angle. (a) Sample created with CSAR, featuring 200 nm periodic antidots with a diameter of approximately 120 nm. (b) Antidots made with PMMA, exhibiting a rather quadratic shape with a periodicity of 600 nm and a maximum diameter of 450 nm. (c) 800 nm periodic antidots built with negative resist with a diameter of 90 nm. (d) Example image of a lift-off revealing two failures. The brighter, hill-shaped structures in the centre of the image (red rectangle) are resist columns that are completely covered by a metallic layer. They were not removed during the lift-off. On the left-hand side of the image (magenta rectangle), the entire metallic layer has been ripped off, revealing the etching trenches caused by argon ion bombardment. On the right (green rectangle), the antidot lift-off was successful.

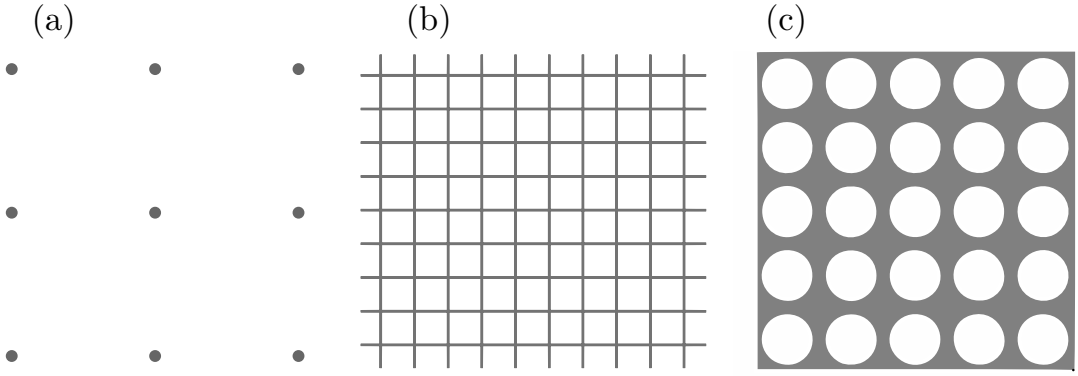

Fig. 4.5.: Different lithographic exposure methods. (a) If a negative resist is used, periodically spaced dots can be exposed. Due to electron scattering processes, this results in resist columns of finite diameter after development. The thickness can be influenced by the point dose (unit fC). (b) However, when using positive resists, the resist must be exposed around the resulting resist column. A cross-shaped line grid has proven to be very successful. The intersections of the grid receive twice the exposure dose, resulting in a larger width of the exposed resist at these points due to the electron scattering proximity effect [110]. By optimizing the line dose (unit $\mathrm{pC\,cm^{-1}}$), round resist columns and consequently round antidots are obtained. (c) This method also applies to positive resists: exposing the entire area (unit $\mathrm{\mu C\,cm^{-2}}$) surrounding the antidots turned out not to be advantageous compared to the line dose method. The proximity effect due to the electron scattering, which occurs during exposure, was too large to reliably produce finely resolved structures [110].

(CSAR, PMMA) and negative resists (AR-N 7520). For positive resists, the areas that are not exposed by the EBL remain after development. The resist is exposed in a grid lattice shape. Figure 4.5 (b) and (c) shows corresponding lithographic patterns. Afterwards, a chemical specifically designed for this purpose dissolves only the exposed resist. Only periodically arranged resist columns remain. Conversely, for negative resists, dot-shaped areas are exposed, as shown in figure 4.5 (a). Again, a specific chemical is used, but this time it removes the unexposed resist. The result is similar as only resist columns with positions defined by the lithographic file remain.

Further differences exist between the three resists used. These will be briefly discussed here: CSAR has a natural undercut, i. e. the resist columns are slightly thinner at the bottom than at the top [107]. This facilitates the lift-off process. In contrast, PMMA does not have a natural undercut. Therefore a double resist system was used. Initially, PMMA 50K resist is applied, followed by PMMA 200K. The lower layer exhibits more sensitivity to the electron beam than the upper layer, resulting in a pronounced undercut [108]. Even though the negative resist AR-N 7520 does not show any undercut, an attempt was made to use it as the objective was to generate the smallest possible antidots with large periods [109].

Antidots with very small periodicities down to 150 nm were achieved with

CSAR. PMMA successfully produced highly uniform antidots with larger periodicities (400 - 800 nm) and larger diameters (300 - 600 nm). By using negative resist, tiny antidots - with diameters as small as 40 nm and periodicities of up to 800 nm - could be produced. However, the lift-off failed for the majority of the samples due the negative resist's missing undercut. Despite these challenges, a number of samples were successfully fabricated. A detailed list of the individual work steps and process parameters can be found in appendix A.

4.4. Topgate deposition

Similar to a field-effect transistor, the Fermi energy in the band structure of HgTe can be tuned with a metallic topgate. In this way, the behaviour of the charge carriers in the valence band, in the band gap and in the conduction band can be investigated. Furthermore, the topgate structure is essential for capacitance measurements.

Figure 4.6 shows such a topgate stack. To build it, two types of **insulators** are used. First, 30 nm SiO_2 are deposited globally, i. e. over the entire sample area. This is done with a plasma enhanced chemical vapour deposition (PECVD)

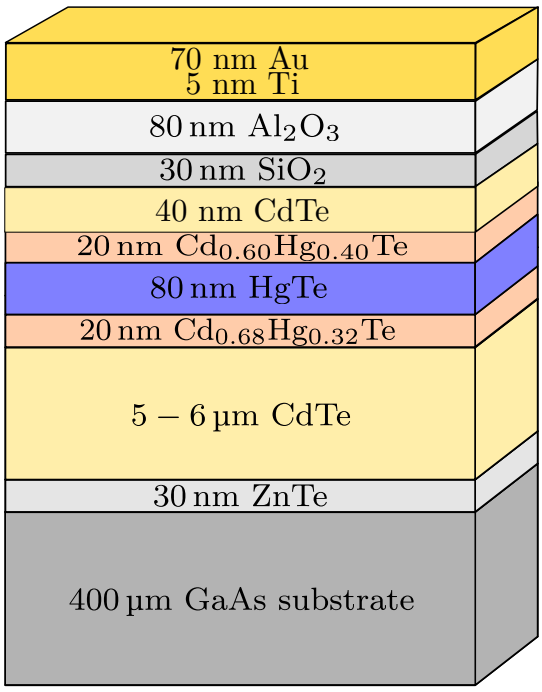

Fig. 4.6.: Cross section, not to scale, of a sample based on the wafer number 190301 with a topgate deposited on it. This figure depicts the individual layers used in the experiments presented in the chapter 6, so there is no layer with antidots. In addition to the insulating CdTe and $Cd_xHg_{1-x}Te$ two different materials, namely SiO_2 and Al_2O_3, function as dielectrics. The SiO_2 layer is 30 nm thick and serves as a seed layer for the growth of 80 nm of Al_2O_3. Moreover, a metallic electrode consisting of 5 nm Ti and 100 nm Au is deposited.

process at a temperature of 80 °C. The SiO_2 layer has a relative permittivity of $\epsilon_{SiO_2} = 3.5$ [39], serving as a seed layer for the subsequent growth of the Al_2O_3, which has a significantly higher permittivity of $\epsilon_{Al_2O_3} = 9$ [111]. The Al_2O_3 is globally grown to a layer thickness of 80 nm at a temperature of 80 °C using a process called atomic layer deposition (ALD). In this process, gaseous trimethylaluminium and water vapour are alternately released onto the sample surface, which then grow in layers and finally yield the electrically insulating compound Al_2O_3.

For the **metallic** topgate electrode, a lithographic process similar to that used for the mesa is employed. First, a resist is applied, optically exposed and then developed to act as a template for the shape. Using a vacuum based physical vapour deposition (PVD) process, a 5 nm thick titanium layer is deposited, followed by a 70 nm thick layer of gold. The titanium serves as a adhesion layer between the insulator and the gold.

It should be noted that the resist mask serves a slightly different function

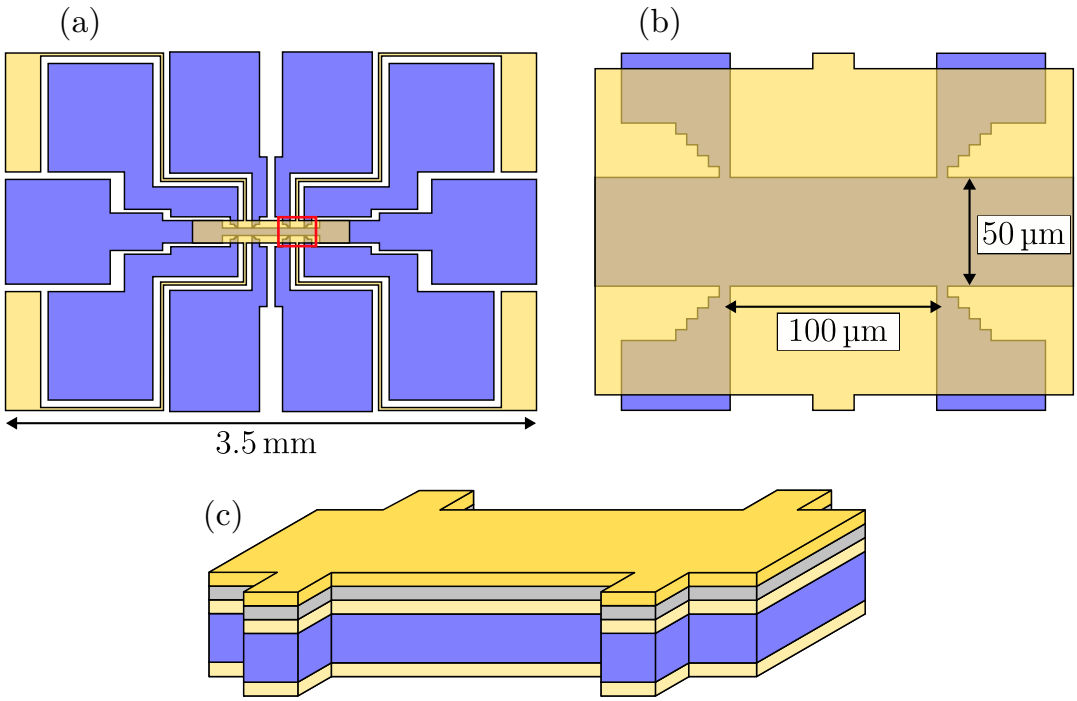

Fig. 4.7.: (a) Typical sample design from a bird's eye view with topgate. Only the HgTe mesa (purple) and the metallic topgate electrode (gold, slightly transparent) are shown, without showing the insulators in between. There are four topgate contact pads in the corners of the design, three of which are redundant. Thin lead channels connect these pads to the sample centre. (b) Enlargement of the image section indicated with a red rectangle on the left. The topgate overlaps with the Hall bar. By applying a voltage, it is possible to adjust the Fermi energy in the system. (c) Schematic, highly simplified 3D view of the Hall bar. The topgate electrode (gold) is separated from the conducting HgTe (purple) by thin insulator layers (yellow and grey).

in this process. In etching, the resist covers the shape of the resulting mesa to protect it from the etching chemicals. Conversely, for the topgate electrode, the resist mask takes on a negative shape. Its purpose is to completely cover areas where the presence of Ti-Au is unwanted. A lift-off process is then used to remove the resist and the metals above it, using acetone as a solvent. All that remains is the Ti-Au adhering directly to the insulators. The design is based on the principle that the metal should cover the entire Hall bar to ensure a uniformly tuned Fermi energy within the four-point voltage taps. However, the metallic leads and contact pads should not overlap with the HgTe leads or contact pads, else it increases the risk of electrical short-circuits. An example of this type of design is shown in figure 4.7.

4.5. Electrical contacting

The completed sample is then glued into a standardised 20-pin chip carrier with PMMA resist. This enables all sample holder sockets of our group's various cryostats to be used. To create electrical connections between the sample's contact pads and the chip carrier, a **gold wire** is bonded with a wire bonder. The wire can be properly bonded to the contacts on the chip carrier and the golden contact pads of the topgate. However, to establish a reliable connection with the contact pads of the HgTe mesa, a soldering procedure with indium is imperative. The metal secures the wire in place and facilitates an electric connection through the insulators to the HgTe.

5. Low-temperature measurement setups

This chapter explains how the samples were measured electrically at low temperatures. It begins with a brief description of the cryostats used. A detailed explanation of the capacitance measurements is then given. The relevant terminology is explained and the necessary electronic hardware, the different measurement setups used and the difficulties encountered are discussed. Finally, the setups for four-point resistance measurements are described.

5.1. Cryostats

Two fundamentally different cryostat types were used in this work: the ^{4}He bath cryostat with variable temperature insert (VTI) and the ^{3}He/^{4}He dilution refrigerator. This section provides a brief overview of the cryostats, with a focus on their potential applications and limitations. For a more detailed understanding of the physical and technical aspects, refer to Enss and Hunklinger [112] or Pobell [113].

5.1.1. ^{4}He bath cryostat with VTI

The measurements of the flux quantisation in niobium antidots presented in this thesis require constant temperatures near its superconducting transition temperature. A ^{4}He bath cryostat with VTI is well suited for this purpose. This VTI vessel is enclosed by a helium bath dewar at 1 bar pressure, with helium at its boiling point of 4.2 K. A continuous flow of helium is let into the VTI via a needle valve. Simultaneously, the VTI is pumped to obtain pressures below 1 mbar. Due to evaporation temperatures of 1.4 K can be achieved. Additionally, the VTI, which is thermally insulated from the helium bath, can be heated by a heating coil. A PID (Proportional–Integral–Derivative) heater control system can adjust the temperature to any required value between 1.4 K and 200 K. The 4.2 K helium bath also contains a superconducting coil for the generation of magnetic fields. The maximum fields that can be achieved are 10 T or 16 T, depending on the system.

5.1.2. ^{3}He/^{4}He dilution refrigerator

To achieve high-precision measurements of the QHE or SdH oscillations in HgTe, mK temperatures are advantageous, since the Landau levels are only resolved if $k_B T < \hbar\omega_c$. For this purpose a dilution refrigerator with a mixture of ^{3}He and ^{4}He atoms is more suitable. This mixture is also called the diluted phase, as the ^{3}He is dissolved in the ^{4}He atoms. At a ^{3}He concentration of 6.5 % the phase is saturated. If there is an excess of ^{3}He in the system, phase separation occurs. The light ^{3}He phase floats on top, and the heavy ^{3}He/^{4}He mixture is located at the bottom. The cooling process operates in the following way: ^{3}He is continuously removed from the ^{3}He/^{4}He-mixture with a still. ^{3}He atoms then cross the phase boundary from the concentrated ^{3}He phase into the mixture. The ^{3}He atoms in the ^{3}He phase have a lower entropy than the ^{3}He atoms in the mixture. During the phase transition, heat is removed from the environment, resulting in the cooling effect. In some systems, temperatures below 2 mK can be achieved [114].

The experimental setup available for the experiments of this thesis is composed of multiple layers. The outermost layer is a vacuum chamber, which encloses a liquid nitrogen shield. Inside the nitrogen shield is a ^{4}He reservoir which houses another vacuum chamber. Only in the central part one can find the mixing chamber where the ^{3}He/^{4}He-mixture is located. It is possible to reach temperatures in the low, double-digit millikelvin range [64]. If the capacitance sample holder is utilised, a temperature of 50 mK is reached owing to heat coupling. The available dilution refrigerator also has the advantage that the highest magnetic field that can be reached is 19 T (without the lambda stage 17 T), exceeding the maximum fields of the ^{4}He bath cryostats.

The physics of a dilution refrigerator has only been touched upon briefly in this section; a more detailed description can be found in in the book by Christian Enss and Siegfried Hunklinger [112].

5.2. Capacitance measurements

The main experimental focus of this work was on magnetocapacitance measurements which allow for the investigation of the uppermost layer of charges [39]. Regardless of the exact measurement technique, parasitic capacitances are inevitable. Coaxial cables are therefore indispensable for capacitance measurements. The inner conductors transport the measurement signal, while the outer conductors are grounded. To be able to conduct capacitance measurements at very high magnetic fields up to 19 T and temperatures down to 50 mK, a sample holder rod with coaxial cables for the ^{3}He/^{4}He dilution refrigerator was designed and built as part of this work. Two different techniques were used to carry out the capacitance measurements, both initially following the same

principle: Between the metallic topgate electrode and the mesa a DC voltage V_g is applied, so that the Fermi energy can be tuned within the electronic band structure. An alternating voltage V_{AC} of fixed frequency is then superimposed. The signal readout is where the difference of the two measurement techniques occurs: When measuring with lock-ins, the capacitance is obtained by measuring the out-of-phase current. Alternatively, the commercially available AH 2700A bridge uses a balancing process similar to the Wheatstone bridge to determine the capacitance [115]. The so-called resistive effects can be minimised with proper measurement technique parameters. All these aspects are discussed in detail below.

5.2.1. Parasitic capacitances

In the samples fabricated for this work, the topgate-insulator-mesa structure was fabricated primarily for two reasons: firstly, to tune the Fermi energy of the system, and secondly, to gain information about the DOS by measuring the quantum capacitance. It is an intentionally integrated capacitor in the sample circuit. Apart from this, however, there are other capacitances that can play a role. In Glisson's Introduction to Circuit Analysis and Design [116] it is stated that "[...] whether we like it or not, capacitance is present wherever current-carrying conductors are separated by an insulating medium". These unwanted capacitances are referred to as either stray capacitances or parasitic capacitances. A distinction is made as follows: stray capacitances are widely distributed in the electronic circuit. This could, for example in a cryostat, be a capacitance from a conductor inside a sample holder to the sample holder itself. Parasitic capacitances are considered to be more localized: A non-ideal resistor can be described by a parallel circuit of this same resistor and a parasitic capacitor. For simplicity, in this thesis no distinction is made and all undesired capacitances are called **parasitic capacitances** [116]. It is very challenging to eliminate these capacitances and it is complicated to calculate their exact value. Nonetheless, with a well-designed construction of an electronic circuit they can be minimized. A crucial step to avoid parasitic capacitance is to utilise coaxial cables.

5.2.2. Capacitance sample holder

For both types of instruments, the ^{4}He bath cryostat with VTI and the ^{3}He/^{4}He dilution refrigerator, capacitance measurements can be performed, but a sample holder with **coaxial cables** is necessary. A suitable sample holder for the ^{4}He bath cryostats was available at the beginning of the experimental research phase of this work, whereas one had to be constructed for the dilution refrigerator.

An existing sample holder rod was equipped with a new cable harness in

order to carry out capacitance measurements on the dilution refrigerator. It was ensured that the cables were coaxial throughout. Therefore, each cable at the top of the sample holder had to be made with a separate shielded vacuum feedthrough. For this purpose, BNC connectors were welded to prevent air from leaking into the vacuum chamber within (see figure 5.1 (a)).

The inner and outer conductors of the coaxial cables are made of stainless steel, the insulating material in between the conductors and the jacket material around the outer conductor is Teflon. Two things were done to minimise the additional heat input of the outer conductors into the sample chamber: Firstly, the maximum number of cables of 20 given by the number of available chip carrier contacts was waived and only 12 cables were laid. Secondly, a thermalisation, i. e. , a gold-plated copper block was installed. The outer jacket material of the cables was removed and the outer conductor was brought into thermal contact with the copper block, as shown in figure 5.1 (b). To prevent ground loops, two-component thermally conductive epoxy encapsulant was used to glue Kapton between the copper block and the outer conductor. Kapton is known to be electrically insulating, but has high thermal conductivity at low temperatures [117]. The thermalisation is exclusive to the sample holder for the dilution refrigerator as it is not required the ^{4}He bath cryostats.

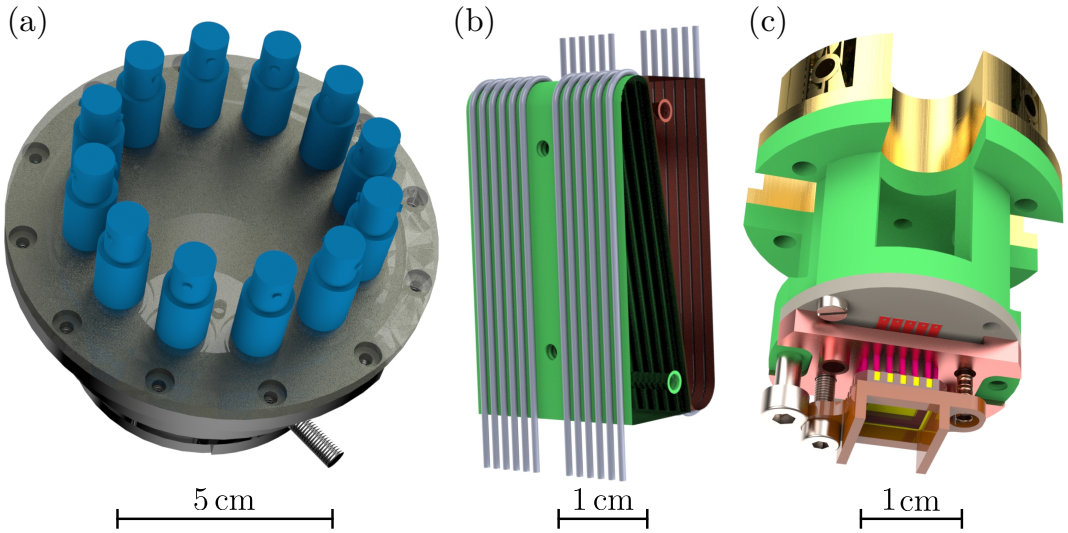

Fig. 5.1.: Rendered 3D CAD (computer-aided design) models of the key components of the capacitance sample holder for the dilution refrigerator. These false colour images highlight specific parts to enhance their visibility. (a) The top of the sample holder features welded BNC connectors (blue) to ensure continuous coaxial shielding. (b) To enhance thermal contact, the outer conductors of the 12 coaxial cables (grey) are in thermal contact with a gold-plated copper block (green/red) and the cables are laid out in an S-shaped loop around this block. (c) The base socket of the sample holder utilizes unshielded pogo pins (pink) to connect the chip carrier (brown/yellow, partially visible) to the coaxial cables. The CAD files were created and rendered by Michael Weigl.

Figure 5.1 (c) shows the base socket, which forms the bottom of the sample holder. It was designed such that the unshielded pins touching the contacts of the chip carrier were as short as possible. Out of a total cable length of about 4 - 5 m from the electronics to the chip carrier, the only remaining unshielded cable paths are these pins, which are about 5 mm long.

The properties of the sample holder were tested, achieving a base temperature of 57 mK that exceeded expectations and fulfilled the requirements. The experimental section of this work includes several capacitance curves which were successfully measured with this sample holder.

5.2.3. Capacitance with lock-in amplifiers

One can measure capacitances using lock-in amplifiers by applying an alternating voltage V_{AC} at a specific measuring frequency f to the capacitor and detecting the resulting current **phase-sensitively**. I_y is the current shifted by 90° with respect to the input alternating voltage signal. A quantity called capacitive reactance X_C can then be defined:

$$X_C = \frac{V_{AC}}{I_y}. \tag{5.1}$$

This reactance is directly related to the capacitance C and is frequency dependent:

$$X_C = \frac{1}{\omega C}. \tag{5.2}$$

By comparing these two equations the capacitance can be determined [116].

Figure 5.2 displays the capacitance measurement setup most frequently used in this work. The alternating voltage is indicated on the left-hand side of the electric circuit diagram and flows through a pre-capacitor labelled C_{pre} to the sample. The topgate stack, consisting of metallisation, insulator and mesa, is itself a capacitor called sample capacitance C_s here. The current is measured phase-sensitively with a lock-in device marked as AC voltmeter. Since C_{pre} and C_s are connected in series, the capacitance value of interest, C_s, can be determined from the measured capacitance C as follows:

$$\frac{1}{C} = \frac{1}{C_s} + \frac{1}{C_{pre}} \quad \Rightarrow \quad C_s = \frac{C_{pre}C}{C_{pre} - C}. \tag{5.3}$$

Furthermore, to enable measuring the capacitance of the sample at a specific Fermi energy E_F, a DC source and a pre-resistor R_{pre} are integrated into the setup. This pre-resistor prevents the AC current from grounding over the DC source output, while the pre-capacitor prevents the DC current from grounding over the AC source output.

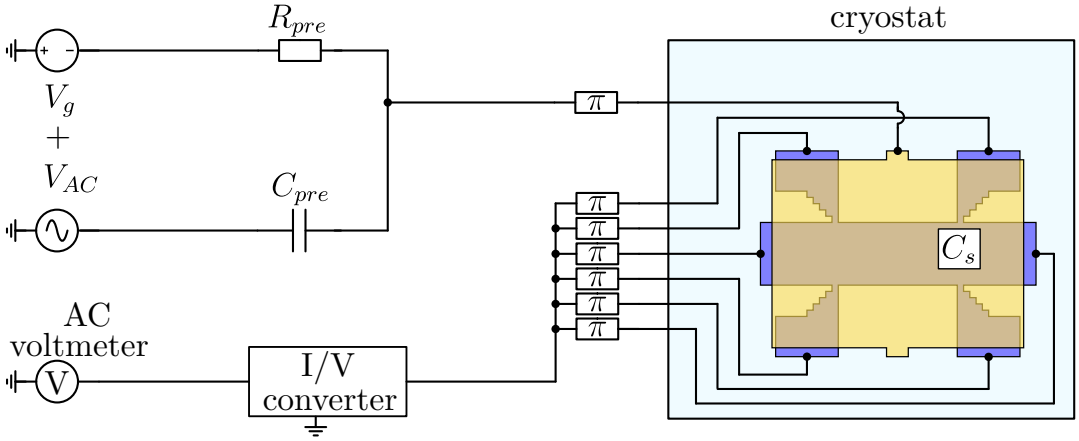

Fig. 5.2.: Electrical circuit diagram of a capacitance measurement using lock-ins. The DC voltage V_g is superimposed to the alternating voltage V_{AC} and is applied to the topgate of the sample. The topgate stack, consisting of metallisation, insulator and mesa, represents the sample capacitance C_s. The DC voltage tunes the Fermi energy E_F in the band structure. The AC current flowing through C_s is conducted out of the cryostat via the mesa contacts, which are connected in parallel to reduce resistive effects. An I/V converter amplifies and converts the signal into a voltage which is then precisely measured by the AC voltmeter. All cable runs and vacuum feedthroughs are completely coaxial. To prevent radio frequency radiation from the environment from affecting the measurement, supplementary 5.5 nF π-filters were installed. The cut-off frequency of these low-pass π-filters is several orders of magnitude higher than the frequencies used. Therefore, they do not need to be taken into account when calculating sample capacitance.

Since R_{pre} and C_{pre} are connected in parallel, they result in a high-pass filter where all frequencies below f_c are cut off:

$$f_c = \frac{1}{2\pi R_{pre} C_{pre}}. \tag{5.4}$$

This means that the values of R_{pre} and C_{pre} must be chosen such that $f_c < f$. Since only frequencies above 1.1 Hz were used for capacitance measurements in this work, values of $R_{pre} = 1\,\mathrm{M\Omega}$ and $C_{pre} = 1\,\mu\mathrm{F}$ satisfy the above condition.

5.2.4. AH 2700A bridge

The Andeen-Hagerling 2700A (AH 2700A) is a commercially available capacitance bridge that can simultaneously measure capacitance and so called losses. Losses are defined as the component of the impedance which is shifted by 90° with respect to the capacitive component. These losses are expressed in siemens, the unit of electric conductance.

The AH 2700A employs stable temperature-controlled fused-silica standard capacitors and pseudo-resistors. The fundamental principle of the bridge is that the unknown impedance of the DUT (device under test), i. e. in this work

the impedance of the topgate-insulator-mesa structure, is **compared** with the known impedance of both the standard capacitor and the pseudo-resistor.

The electrical circuit diagram is displayed in figure 5.3. An AC sine wave generator is used to excite a ratio transformer. The transformer is connected to leg 1 and leg 2. For both legs, a precise voltage can be chosen using a tap changer. The voltage V_1 applied to leg 1 is then transmitted to leg 3 where fused-silica capacitors with capacitance C_0 are located. These capacitors are connected in parallel with the pseudo-resistor R_0 to represent a reference impedance. The voltage V_2 applied to leg 2 is transmitted to leg 4, where the DUT resides. The DUT consists of capacitance C_x and resistor R_x for non-ideal capacitors. Both reference impedance and DUT experience a voltage drop. The resultant signals are superimposed and a detector reads the superimposed signal [115].

The balancing procedure proceeds with the microprocessor controlling the voltage taps of tap 1 and tap 2 on the transformer and altering C_0 and R_0 until the voltage at the detector becomes immeasurably small. In this case, the bridge is **balanced** and C_x and R_x can be calculated using the following ratios:

$$C_x = \frac{V_1}{V_2} \cdot C_0 \tag{5.5}$$

and

$$R_x = \frac{V_2}{V_1} \cdot R_0. \tag{5.6}$$

The bridge reports the capacitance C_x and the losses $1/R_x$ as soon as it is balanced.

The AH2700A is connected to the capacitance sample holder using coaxial

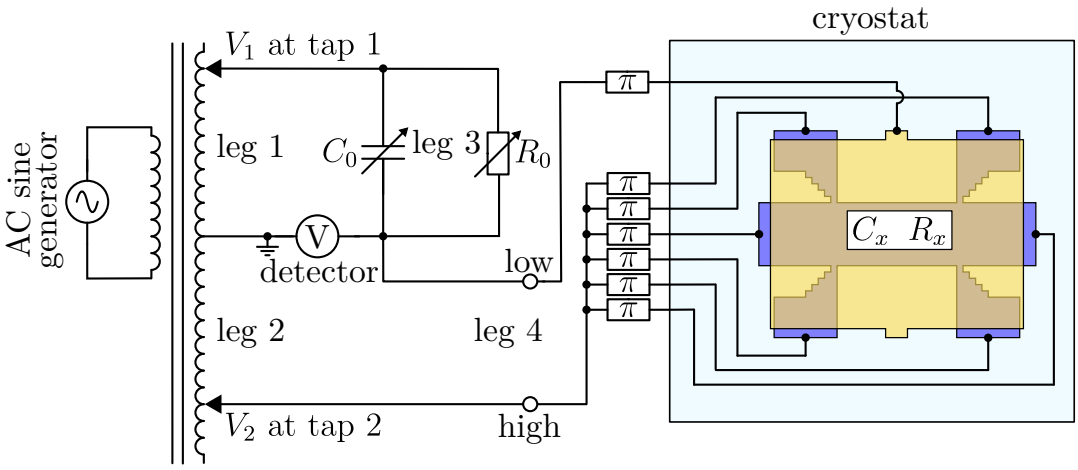

Fig. 5.3.: Electrical circuit diagram of the AH 2700A capacitance bridge. The bridge compares a reference impedance composed of C_0 and R_0 with the impedance of the topgate-insulator-mesa structure comprising C_x and R_x. The exact operation of the bridge is explained in the body text (AH 2700A circuit taken from [115]).

cables. It is a three-terminal measurement, where the signals pass over the the high and low inner conductors, while the outer conductors are grounded to safeguard against parasitic capacitances and noise [115]. Furthermore, similar to the lock-in technique, a DC voltage can be used to tune the topgate, applied via the low contact of leg 4. Moreover, as with the lock-in measurement technique, 5.5 nF π-filters were added to the setup.

The mesa contacts are all short-circuited to minimize resistive effects. Moreover, it is important to use the lowest frequency possible to prevent resistive effects that may arise at higher frequencies. This is a major drawback of the AH2700A for the experiments in this work, as the frequency interval is limited from 50 Hz to 20 kHz. To be able to measure at lower frequencies of down to 1.1 Hz, the lock-in technique described in the preceding section had to be resorted to. Another drawback is the time-consuming balancing process, which, depending on the setting, can take over 1 min per data point.

5.2.5. Resistive effects

If capacitance is measured in a topgate-insulator-mesa stack based on HgTe, so-called resistive effects may occur. This section clarifies these effects and provides solutions for avoiding them.

The resistive effects occur due to the finite conductivity of HgTe. Whenever the AC voltage applied to the topgate changes sign, the charges in the mesa must rearrange themselves. Depending on the frequency, they have only limited time to reach equilibrium. Figure 4.7 shows the topgate-insulator-mesa structure, which can be represented by a complex network of resistors and capacitors in an electrical circuit diagram [118]. However, the circuit can be simplified to include only the resistance R of the mesa and the capacitance C of the insulator in series. The corresponding impedance Z is shown in figure 5.4. It can be expressed as

$$Z = R + \frac{1}{i\omega C}, \tag{5.7}$$

with $i = \sqrt{-1}$ representing the imaginary unit and $\omega = 2\pi f$ representing the angular frequency. Instead of the complex resistance Z, its reciprocal, the

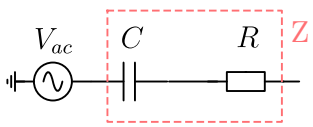

Fig. 5.4.: Electrical circuit diagram. A voltage V_{AC} is applied to the series element consisting of a capacitor C, and a resistor R, forming an impedance Z.

admittance Y, can be computed by

$$Y = \frac{1}{Z} = \frac{\omega^2 RC^2}{1+\omega^2 R^2 C^2} + i\frac{\omega C}{1+\omega^2 R^2 C^2} = G + iB. \tag{5.8}$$

The real part of equation 5.8 is known as the effective conductance G, whereas the imaginary part B is the susceptance [116]. Using $Y = I/V_{AC}$, the real component of the current I_x can be obtained from the effective conductance. The imaginary component I_y, i. e. the component that is phase-shifted by 90° with respect to the voltage, can be obtained from the susceptance [119]:

$$I_x = \frac{\omega^2 V_{AC} RC^2}{1+\omega^2 R^2 C^2} \quad \text{and} \quad I_y = \frac{\omega V_{AC} C}{1+\omega^2 R^2 C^2}. \tag{5.9}$$

I_y is then used to determine the capacitance, as detailed in section 5.2.3. However, a **purely capacitive** signal is obtained only if the condition

$$\omega RC \ll 1 \tag{5.10}$$

is satisfied. Then, $I_y = \omega V_{AC} C$ and $I_x = 0$, meaning the entire current is out of phase. This requirement can be fulfilled by reducing the frequency ω.

In an HgTe sample, the resistance is heavily dependent on the magnetic field because of the QHE and the SdH oscillations. At high fields and low temperatures σ_{xx} approaches zero when the Fermi energy is between two Landau levels. As a result, the system is no longer purely capacitive, and the real component I_x becomes finite rather than vanishing. The resistive effects occur precisely under these conditions, i. e. at low σ_{xx}. Interestingly, due to the tensorial calculation of the conductivity, this corresponds to a vanishing resistivity in ρ_{xx} and a constant value in $\rho_{xy} = R_K/\nu$. Thus, the term "resistive effects" is meaningful only to a limited extent in this context, as the relevant parameter is conductivity, not resistivity. Nonetheless, the term will be used throughout this thesis. Overcoming the occurrence of resistive effects presented a significant experimental challenge.

Describing the ratio of I_x to I_y in Hall bar geometry precisely is difficult. Goodall et al. [119] investigated the relationship between σ_{xx} and capacitance C in their study featuring a Corbino disk geometry. They expressed the radial current I using the equation

$$I = I_0 \frac{\tanh(\alpha)}{\alpha}. \tag{5.11}$$

Here, I_0 is the current in the case of a very high conductivity. The value of the

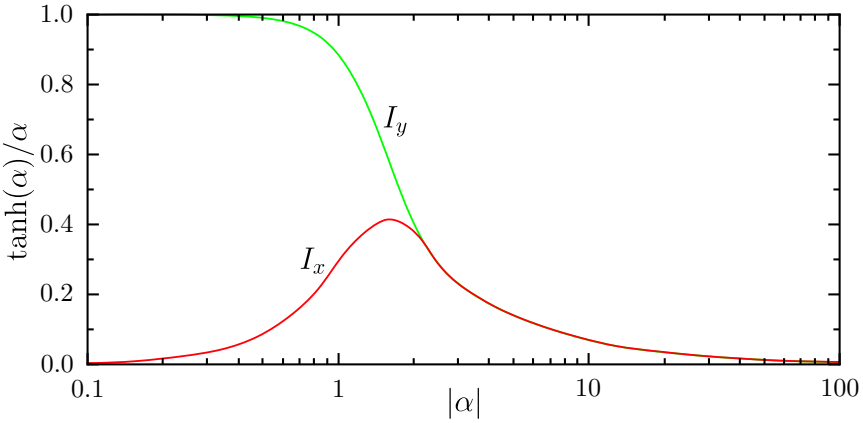

Fig. 5.5.: Dependence of the real and imaginary parts of the capacitance current on frequency and conductivity. A low $|\alpha|$ value implies a high conductivity or low frequency. The current I_y is significantly greater than I_x, indicating a capacitive signal, with resistive effects playing a negligible role. Conversely, a high $|\alpha|$ value implies a low conductivity or high frequency, and resistive effects can no longer be neglected (adapted from [119]).

complex quantity α can be calculated using

$$\alpha = \left(\frac{i\omega C L^2}{\sigma_{xx}} \right)^{1/2}, \tag{5.12}$$

where L is the length of the channel. It should be noted that C is the insulator capacitance and does not include quantum capacitance in this study. These equations cannot be quantitatively applied in this thesis as they were formulated for a Corbino geometry. However, in his doctoral thesis, Dieter Weiss [71] demonstrated that the curves presented in figure 5.5 can provide a qualitative description of the behaviour of I_x and I_y in a Hall bar geometry.

Low conductivity or high frequencies may prevent accurate capacitance measurements, causing the capacitance in the LL gaps to exhibit deep frequency dependent minima. Examples for this can be seen in figure 5.6. Additionally, it is important to mention that at low temperatures, the σ_{xx} minima of the SdH oscillations approach zero. As the temperature increases, the minima become less pronounced, and σ_{xx} assumes a small but finite value. In conclusion, low magnetic fields, high temperatures and low frequencies are suitable conditions for measuring capacitance. As the experimental goals of this doctoral thesis did not allow for the first condition, the remaining two parameters were adjusted. Accordingly, capacitance measurements were carried out at temperatures of up to 5 K and frequencies as low as 1.1 Hz. Additionally, the mesa contacts can be short-circuited, as shown in the electrical circuit diagrams in this chapter. The advantage of such a circuit is that it provides a lower parallel resistance compared to the individual contact and cable resistances.

To experimentally verify a purely capacitive signal, the frequency dependence

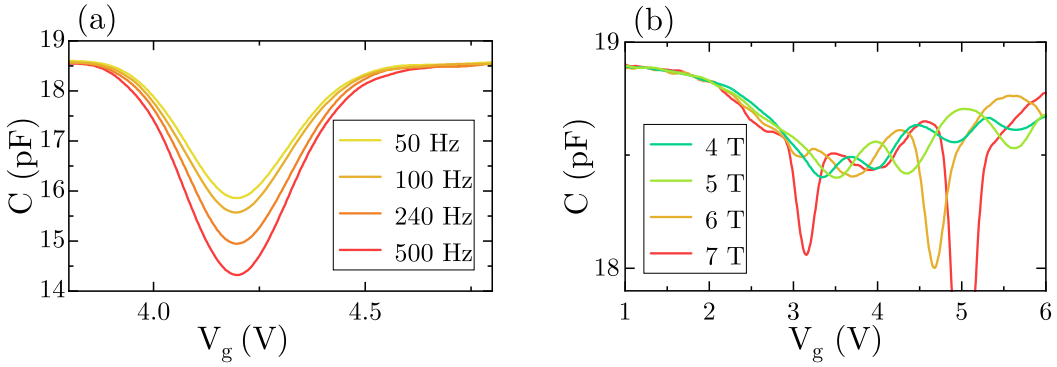

Fig. 5.6.: Resistive effects in the "capacitance" as a function of gate voltage V_g, measured with the AH2700 A bridge. (a) The depth of the capacitance minima (measured within a Landau Level gap) increases with increasing frequency due to resistive effects. To obtain a purely capacitive signal, the frequency needs to be decreased until the signal saturates. The signal outside the Landau Level gap is frequency-independent as the conductivity in this region is large. The data was collected at a temperature of 57 mK and a magnetic field of 10 T. (b) The resistive effects are primarily observed at higher magnetic fields, as the magnetic field strongly affects conductivity. At 4 T and 5 T, the oscillations induced by the Landau levels are primarily capacitive. However, at 6 T and 7 T, frequency-dependent deep minima abruptly emerge. The data was acquired at 57 mK and 60 Hz.

is examined. Only if the signal is **frequency independent** the capacitance can be accurately determined and conclusions can be drawn about the thermodynamic density of states.

5.3. Transport measurements

The other main experimental technique used in this thesis are transport measurements of the longitudinal and transversal resistance. Differential resistance measurements were also carried out using a DC voltage modulated by an AC voltage. The measurements were performed in a Hall bar geometry, as described in section 3.1.1, using four-terminal sensing at a few Kelvin and at mK temperatures.

5.3.1. AC lock-in technique

The transport measurements presented in this work were conducted using standard AC lock-in technique. These measurements were made for both samples containing antidots and samples without. To simplify the electrical circuit diagrams in this and the subsequent section, a Hall bar without antidot structures is consistently depicted.

As can be seen from figure 5.7, an AC voltage source V_{AC} with a 10 MΩ

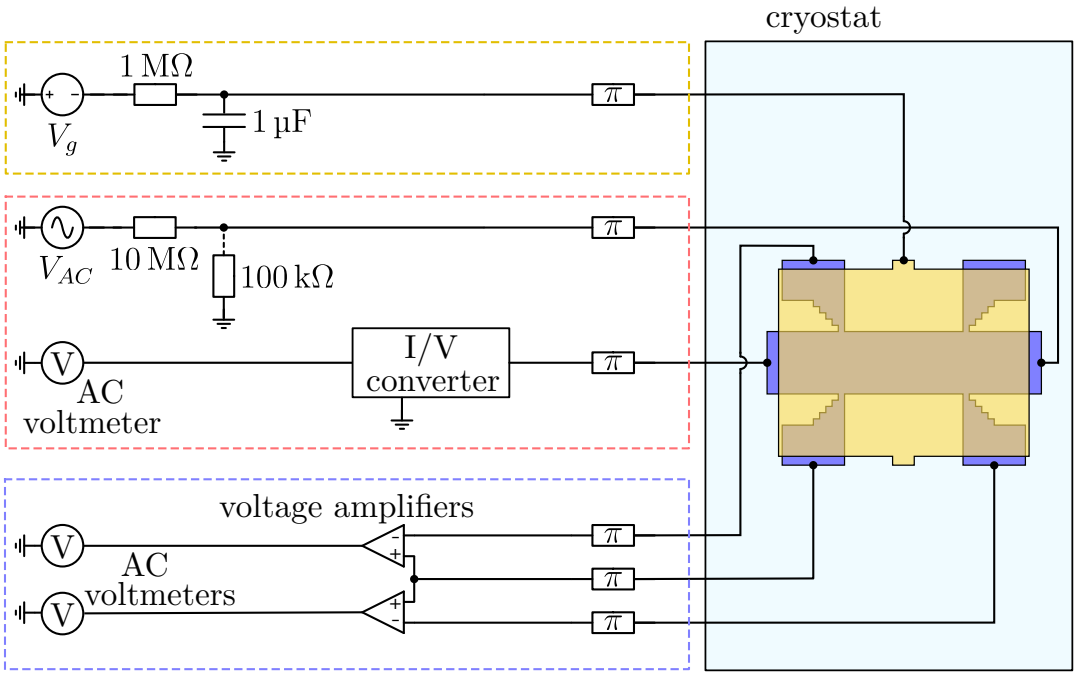

Fig. 5.7.: Measurement setup for the experimental determination of 4-point resistances with lock-in AC technique. The electronic measurement setup can be divided into three distinct parts: In the first part the DC voltage V_g is generated (golden, dashed box) which is applied to the topgate. In the second part, the AC current is generated and measured (red, dashed box), which flows through the Hall bar. In the third part, the four-point voltages are tapped, amplified and measured (blue, dashed box). The π-filters provide protection against interfering radio frequency radiation. For further details on the exact function of the electronic components, please refer to the main text.

pre-resistor was connected in series to the sample resistance. This creates an almost constant current source, with a current given by $I = V_{AC}/R_{pre}$, as the pre-resistance is much larger than the sample resistance. This can be used to ensure that there is a low current flowing through the sample which prevents heating effects. Once the current passes through the sample, it is transformed into a voltage by an I/V converter, which also amplifies the signal for the subsequent measurement.

In some instances, the sample resistance may become notably high. When a constant current is applied, this results in a substantial 4-point voltage drop that could exceed the lock-in measurement range. In order to circumvent this issue an additional, supplementary 100 kΩ resistor can be connected to ground. This setup decreases the current for large sample resistances, and consequently, decreases the 4-point voltage drop at the sample. This allows for a continuous measurement of sample resistance across several orders of magnitude using the same lock-in measurement range.

The transversal and longitudinal voltages are amplified using preamplifiers with 1 TΩ input resistances. This makes any discrepancies caused by high

contact resistances insignificant and ensures that no current flows through the voltage taps. Lock-ins measure the amplified signals, and from ratio of the measured voltages and currents, R_{xx} and R_{xy} are determined.

The voltage V_g at the topgate can be tuned as required. To prevent sudden changes in the voltage, a low-pass filter is utilized, which is composed of a 1 MΩ resistor and a 1 µF capacitor, resulting in a time constant of $\tau = RC = 1\,\mathrm{s}$. This protective measure safeguards the sensitive topgate against electrical breakdown.

5.3.2. Differential resistance

The setup shown in figure 5.8 was used exclusively for some of the measurements in chapter 8. As a result, it allowed the observation of features referred to as "pine trees".

The measurement setup is similar to that described in the previous section. Therefore, only the relevant differences will be discussed below: First, an AC and a DC voltage are coupled using a transformer. This allows for the larger DC voltage to be modulated by the smaller AC voltage. A 10 MΩ series resistor ensures that a current independent of the sample resistance is obtained, which flows through the sample. After the sample, the current is converted to a voltage and the signal is simultaneously amplified. The DC and AC components of the signal can then be separately measured. The alternating current I_{AC} and the direct current I_{DC} are calculated using the current-voltage transformer's known amplification factor.

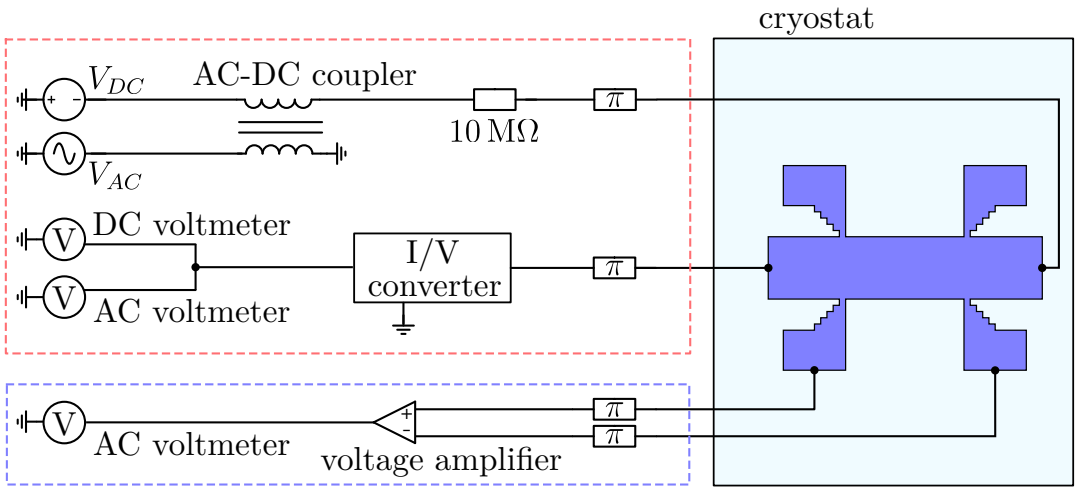

Fig. 5.8.: Measurement setup to determine the differential resistance. As in the previous section, the electronic components which are linked to the current circuit are in the red, dashed box. The components that belong to the four-point voltages detection are in the blue, dashed box. It is also possible to connect π-filters and an additional topgate (not shown).

The AC voltage $V_{AC,\,4pt}$ is tapped via the 4-point Hall bar geometry, amplified and subsequently measured. From the ratio of the four-point AC voltage and the AC current flowing through the sample the differential resistance $R = V_{AC,\,4pt}/I_{AC}$ is determined at a given direct current I_{DC} .

6. Magnetoresistance and capacitance in HgTe

This chapter presents an analysis of capacitance and transport measurements on an HgTe Hall bar made of a modulation-doped wafer. The sample is thoroughly characterized, and a clear electrostatic picture is derived from the observed carrier densities. Subsequently, transport measurements at low magnetic fields and zero-field capacitance measurements are used to define crucial points in the band structure. At higher magnetic fields, a complex pattern of Landau levels (LLs) emerges. The LL have been identified and assigned to the individual 2D electron and hole systems. Finally, capacitance and transport were studied at very high magnetic fields, revealing the merging of the individual systems into a single system. All data in this chapter were measured on a single sample, making them well comparable.

6.1. Wafer characterization

In this section wafer number 190301, which is shown in figure 4.1 (a), is analysed in detail with capacitance and transport measurements. The results of the characterization of the modulation-doped wafer provide information about the position of the valence band (VB) and conduction band (CB) edge. The individual charge carrier densities of the top surface, bottom surface, and bulk can be determined, as well as the carrier mobilities. At $V_g = 0\,\mathrm{V}$, the Fermi energy is located in the CB. As shown in figure 6.1, the charge carrier densities for both the top surface (magenta) and bulk electrons (blue) increase with increasing gate voltage. The **CB edge** E_C^* can be determined by linearly extrapolating the bulk electron density to the intersection with the x-axis. The hole density (red) increases towards negative gate voltages. For these, a similar approach can be used to determine the position of the **VB edge** E_V.

The analysed wafer has a number of unique characteristics, which will be briefly mentioned here. In contrast to the undoped wafers, the bottom of the CB edge is below the top of the VB edge, resulting in the coexistence of bulk electrons and bulk holes. The presence of bulk carriers throughout the entire gate voltage range electrostatically shields the bottom surface, leading to a constant bottom surface (green) charge carrier density. Unlike the wafers characterized

in references [39, 64, 66, 68, 69] the **charge neutrality point** (CNP) is shifted to −2.3 V instead of being at positive gate voltages or around 0 V. Additionally, at 0 V, the electron density of $5.8 \times 10^{11}\,\mathrm{cm}^{-2}$ is significantly higher than in undoped samples, where it is typically below $1 \times 10^{11}\,\mathrm{cm}^{-2}$ [63, 64, 66, 69].

To determine the features and peculiarities briefly listed here, a more detailed analysis is necessary. Due to the complexity of the system, it is necessary to disentangle the different carrier groups and their associated parameters. To achieve this, different experimental techniques were employed, each with unique sensitivities to the respective carrier groups. None of the techniques used provide results of absolute reliability, therefore different approaches are compared. The methods and results will be explained and discussed in the following sections. All charge carrier densities determined in this chapter are reported in figure 6.1, the corresponding mobilities in figure 6.2.

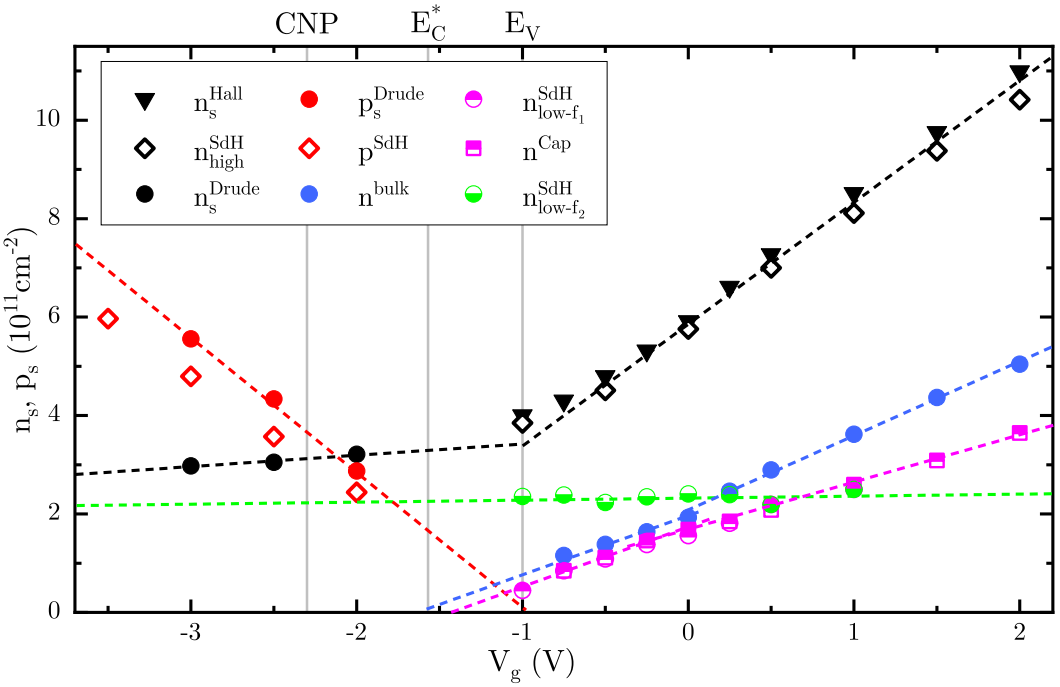

Fig. 6.1.: Electron and hole densities extracted from transport and capacitance measurements. Black data points represent the total electron density, while red data points represent the density of the bulk holes of the valence band. Green and magenta respectively indicate the charge carrier density of the bottom and top surface. The blue data points represent the bulk electrons of the conduction band. CNP stands for the charge neutrality point, E_C^* for the conduction band edge and E_V for the valence band edge. The Dirac point of the top and bottom surfaces lies deep in the valence band. The experimental methods used to determine the individual densities are explained in detail throughout this section.

6.1.1. Densities and mobilities from Drude

At low magnetic fields, transport is completely diffusive and can be described by the Drude model. If only **one type of charge carrier**, in this case electrons, contributes to transport, then the Hall resistivity ρ_{xy} as a function of the magnetic field shows a linear slope in the range of non-quantizing magnetic fields. The total carrier density $\boldsymbol{n_s^{Hall}}$ of the system can be calculated from this slope with the help of equation 3.11. The corresponding mobility $\boldsymbol{\mu_e^{Hall}}$ is an average of the mobilities of all participating electron charge carriers and can be calculated using equation 3.12.

If one drives the topgate to negative gate voltages the Hall slope becomes non-linear beyond a certain point. The reason for this is that if E_F is below the VB edge, holes contribute to the charge carrier transport. Again, the behaviour can be described using Drude, but a **two carrier model** is necessary. The conductivities σ_{xx} and σ_{xy} for electrons (e) and holes (p) then look like this:

$$\sigma_{xx,e(p)} = \frac{q_{e(p)} n_{e(p)} \mu_{e(p)}}{1 + (\mu_{e(p)} B)^2} \qquad \sigma_{xy,e(p)} = \frac{q_{e(p)} n_{e(p)} \mu_{e(p)}^2}{1 + (\mu_{e(p)} B)^2} B. \tag{6.1}$$

Here, $q_{e(p)}$ is the charge, $n_{e(p)}$ is the charge carrier density, $\mu_{e(p)}$ is the mobility and B is the magnetic field. To obtain these expressions, equation 3.11 and equation 3.12 were inserted into equation 3.5. The longitudinal and transversal conductivities are a sum of the respective electron and hole conductivities and

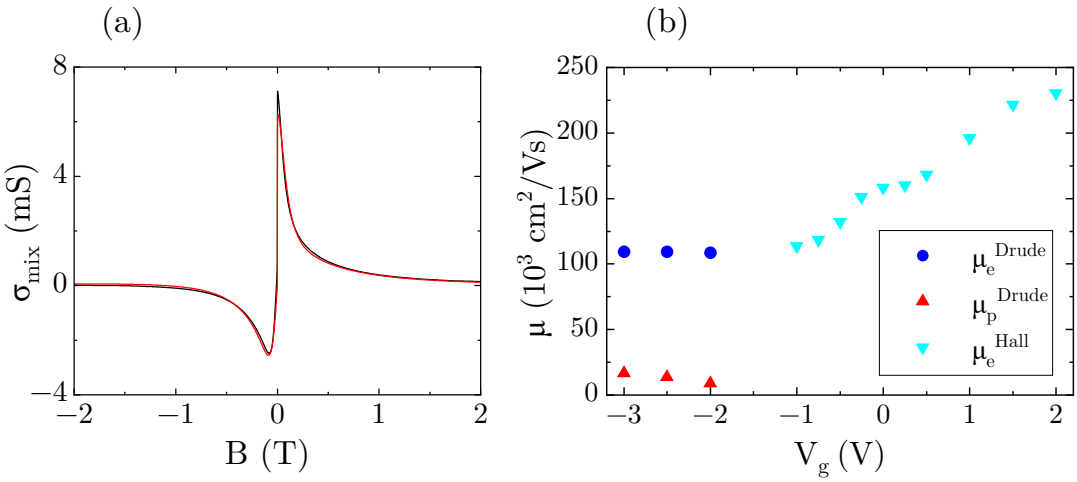

Fig. 6.2.: Electron and hole mobilities in doped wafer. (a) σ_{mix} (black curve) is defined as the longitudinal conductivity σ_{xx} at positive magnetic fields and as the transversal conductivity σ_{xy} at negative magnetic fields. The example shown was obtained at $-2.5\,\mathrm{V}$. The fit (red curve) shows good agreement with the data. (b) The electron and hole mobilities are averages of all charge carriers of the same polarity at the corresponding gate voltage.

given by

$$\sigma_{xx} = \sigma_{xx,e} + \sigma_{xx,p} \quad \text{and} \quad \sigma_{xy} = \sigma_{xy,e} + \sigma_{xy,p}. \tag{6.2}$$

These equations are used to fit the experimentally determined conductivities, as displayed in figure 6.2 (a). Convergence of the fit provides the hole carrier density $\boldsymbol{p_s^{Drude}}$ and the electron carrier density $\boldsymbol{n_s^{Drude}}$, as well as their respective mobilities $\boldsymbol{\mu_p^{Drude}}$ and $\boldsymbol{\mu_e^{Drude}}$ [104, 120].

The hole mobility is almost an order of magnitude smaller than the electron mobility in the valence band. μ_e^{Hall} is the average of top surface, bottom surface and bulk electron mobilities. As the carrier density of electrons increases, mobilities of more than $2 \times 10^5\,\mathrm{cm^2\,V^{-1}\,s^{-1}}$ are reached. The extracted charge carrier densities are reported in figure 6.1, the mobilities in figure 6.2 (b) [59, 64].

6.1.2. Densities from quantum oscillations

At higher magnetic fields, the density of states (DOS) splits into LLs. This is expressed through quantum oscillations as a function of the magnetic field. Figure 6.3 provides examples of these oscillations. From their periodicity, one can determine the respective charge carrier densities.

One of the experimental techniques used in this thesis are capacitance

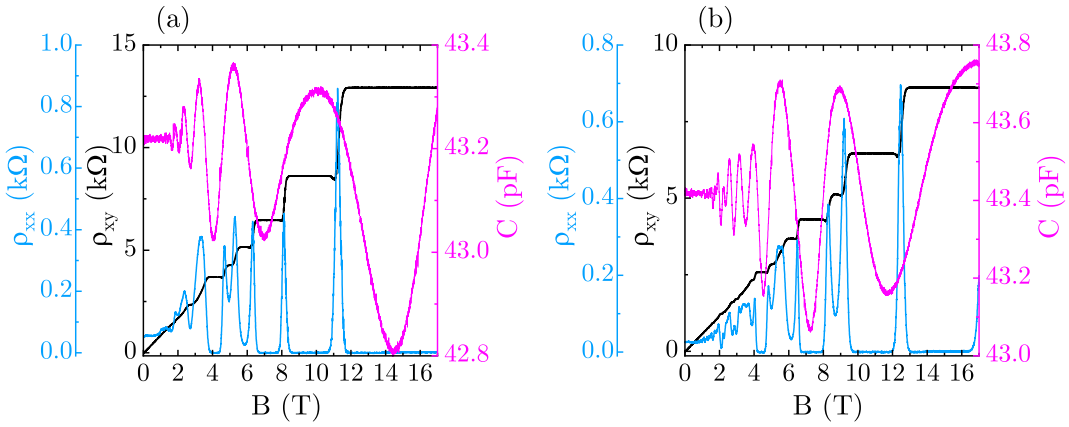

Fig. 6.3.: Example of SdH and capacitance oscillations. (a) The graph displays the Shubnikov-de Haas oscillations observed in the longitudinal resistivity ρ_{xx} (blue) as a function of the magnetic field B, accompanied by QHE plateaus observed in the transversal resistivity ρ_{xy} (black). The capacitance curve (magenta) also exhibits oscillations, but with a different periodicity. The data were obtained at a gate voltage of $V_g = 0.5\,\mathrm{V}$. (b) The graph shows identical measurements and conditions as the left figure, but with an applied voltage of $V_g = 2\,\mathrm{V}$. The transport data (ρ_{xx} and ρ_{xy}) were collected at a low current of 10 nA, at 1.1 Hz and at 57 mK. The capacitance data were collected with the lock-in amplifier setup at 5 K and at a low frequency of 3.1 Hz to minimize any resistive effects.

measurements. Capacitance measurements directly probe the thermodynamic DOS of the uppermost surface [39]. In this section an analysis of the capacitance oscillations was restricted to magnetic fields below 6 T. At this magnetic field range **capacitance oscillations** exclusively reflect the carrier density of the top surface, i. e. the uppermost surface is equal to the topological surface states of the 2DES at the top of the HgTe. The corresponding charge carrier density is denoted by $\boldsymbol{n^{Cap}}$ in figure 6.1.

The resistivity ρ_{xx} as a function of the magnetic field exhibits **SdH oscillations**. At high magnetic fields all charge carriers participate to form these oscillations. If E_F is above the VB edge, the high-field SdH oscillations reflect the total electron charge carrier density $\boldsymbol{n^{SdH}_{high}}$. The situation is similar in the valence band: Here, hole carriers exhibit SdH oscillations. This is described in more detail in section 6.5.3. The corresponding carrier density in figure 6.1 is labelled $\boldsymbol{p^{SdH}}$ [68]. It is noticeable that p^{SdH} and p_s^{Drude} do not match perfectly. A similar discrepancy has been previously observed in HgTe wafers[59, 68]. The feature can be explained by a partial compensation of electrons and holes in the VB [121]. If the V_g dependency of p_s^{Drude} is extrapolated, the approximate position of the VB edge E_V can be determined from the intersection with the x-axis [68, 97].

In previously analysed wafers, the SdH oscillations at low magnetic fields reflected the charge carrier density of the top surface [68]. Here, the analysis of the low-field oscillations in ρ_{xx} yielded conflicting results. The periodicity of the oscillations, in which the minima were determined through visual examination, resulted in a constant carrier density at negative gate voltages. However, for positive gate voltages, it coincided with the linearly increasing n^{Cap} and thus reflected the oscillations of the top surface, as described in Kozlov et al. [39]. Therefore, it was assumed that oscillations of several frequencies overlap at low fields, and only the frequency that dominates at the corresponding gate voltage was observed. To investigate this, **Fourier spectrum of the low-field SdH** was analysed [122]. In order to do this, the data of ρ_{xx} as a function of the magnetic field B were processed as follows: First, to ensure that faintly visible oscillations were amplified, the data were derived twice with respect to B. The data were then plotted as a function of the inverse magnetic field from $1.33 - 0.66\,\mathrm{T}^{-1}$ and subsequently interpolated. Only then an FFT was performed. Figure 6.4 displays the resulting Fourier spectrum, which reveals two peaks for each gate voltage. From a given frequency f_i with peak index i, the corresponding carrier density n_{f_i} can be determined as follows for spin-resolved systems [122]:

$$n_{f_i} = \frac{e}{h} f_i. \tag{6.3}$$

The charge carrier density $\boldsymbol{n^{SdH}_{low-f_1}}$ associated with frequency f_1 coincides with

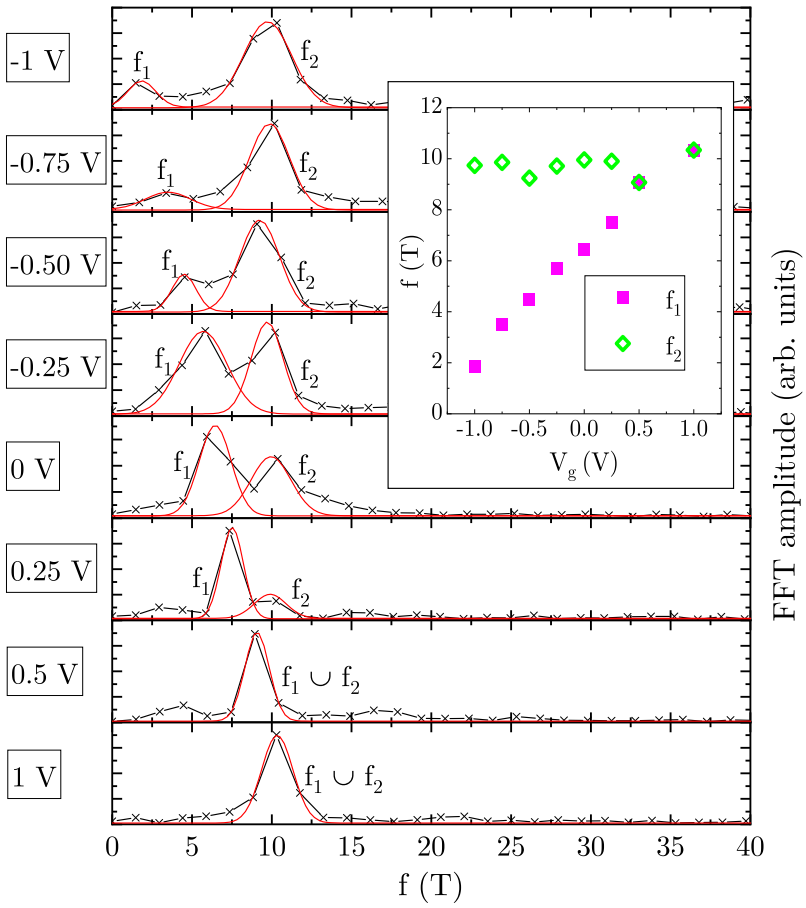

Fig. 6.4.: FFT spectrum and Gaussian fits of low-field SdH. The black crosses connected by lines show the fast Fourier transform spectrum of the low-field SdH oscillations from −1 V to 1 V. Each identified peak has been fit by a Gaussian function (red). The comparison with the capacitance allows the assignment of the peaks marked with f_1 to the top surface. The peaks marked by f_2 are at a constant frequency value and belong to the bottom surface. $f_1 \cup f_2$ symbolizes that both peaks are overlapping. The inset displays the individual peak values as a function of the gate voltage.

the carrier density obtained by the capacitance measurements. Thus, it can be concluded that the low-field SdH oscillations corresponding to this frequency originate from the charge carriers of the top surface. The constant frequency of peak f_2 corresponds to a charge carrier density of $\boldsymbol{n_{low-f_2}^{SdH}} = 2.3 \times 10^{11}\,\mathrm{cm}^{-2}$. In section 6.5.2 it is shown that this reflects the carrier density of the bottom surface. This also explains why the formula for spin-resolved systems was used here, since both top and bottom surfaces are not spin-degenerate.

A comparison of the amplitudes reveals that f_2 is the dominant peak for negative gate voltages. This changes at 0 V and the amplitude of f_1 becomes larger. This confirms that only the dominant frequency was observed during visual examination. At 0.5 V and 1 V only a single peak is observed, which includes both the bottom and top surface peaks, as they have similar carrier densities here. As the gate voltage increases, the charge carrier density of the

top surface also increases, causing the peak to shift to a slightly higher frequency at 1 V.

The total electron charge carrier density (n_s^{Hall}), as well as that of the top surface (n^{Cap} or $n_{low-f_1}^{SdH}$) and bottom surface ($n_{low-f_2}^{SdH}$), are now known. By subtracting the sum of the densities of the top and bottom surfaces from the total electron density, the carrier density of the CB $\boldsymbol{n^{bulk}}$ can be estimated:

$$n^{bulk} = n_s^{Hall} - \left(n^{Cap} + n_{low-f_2}^{SdH}\right). \tag{6.4}$$

In section 6.5.4, the LLs belonging to the bulk are identified.

6.2. Electrostatic model

The carrier density results allow some conclusions to be drawn about the electrostatic situation of the system. This will be substantiated by the upcoming data. The electrostatics are shown here with the help of simple band diagrams. The following paragraphs describe the individual subfigures of figure 6.5:

(a) At −1.5 V Dirac electrons from the bottom surface and bulk holes sitting at the top of the bulk HgTe contribute to the conductivity. Roughly at this gate voltage both Dirac electrons from the top surface and bulk electrons enter the system.

(b) Above −1 V the whole charge transport is carried by electrons. These are located on the top surface, on the bottom surface and in the bulk. At −0.5 V the carrier density of the bottom surface is about twice as high as

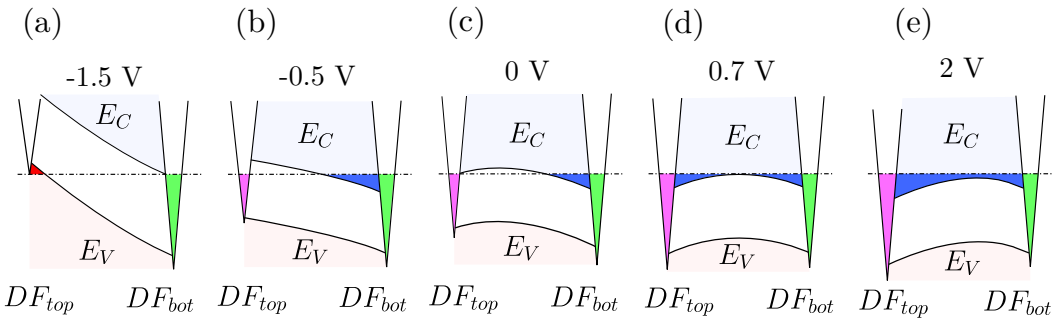

Fig. 6.5.: Cartoon of the cross-sectional band structure of the doped wafer. Each image represents the electrostatic situation at a different gate voltage. The Fermi level is indicated by a dashed horizontal line. Magenta are filled Dirac electron states (labelled with DF for Dirac fermions) in the top surface, green those in the bottom surface. The CB is drawn in bright blue. Filled states in the CB are then coloured with a saturated blue. The valence band is bright red and filled states in the valence band are coloured with saturated red. Poisson's equation of electrostatics suggests that the bulk states are bent toward the surfaces on both sides due to the modulation doping. The individual figures are explained in more detail below.

that of the top surface.

(c) At 0 V, it appears that additional bulk electrons are drawn into the system near the top surface. This is shown in the figure where the Fermi energy intersects the corner of the CB near the top surface. This additional filling of bulk electrons is referred to as the 2nd pocket of the CB in this thesis.

(d) At 0.7 V the top and bottom surface carrier density is equal.

(e) At 2 V the carrier density of the top surface is now higher than that of the bottom surface.

The bottom surface charge carrier density remains almost constant, regardless of the topgate voltage. This indicates that it is electrostatically shielded from the topgate by electrons and holes. The presence of bulk carriers over the entire gate voltage range, as E_V lies above E_C, supports this.

Since the wafer is symmetrically doped with Indium, additional electrons contribute to the conductivity. The negatively charged electrons in the HgTe are attracted electrostatically by the positively charged Indium donors sitting at the CdHgTe. This suggests that the electrons stay in proximity to the respective donor layer [72].

The band bending at negative gate voltages causes the bulk electrons to appear first at the bottom surface. At 0 V, additional bulk electrons from the 2nd pocket of the CB enter the system near the top surface. This is experimentally observable as a kink in n^{bulk} in figure 6.1, a small hump in figure 6.6 (a), and increased conductivity in figure 6.17. This electrostatic model will be underpinned by data presented in the following sections.

6.3. Classical magnetotransport

An additional method of determining the approximate locations of the CNP and CB edge is from the gate voltage dependency of the resistivities ρ_{xx} and ρ_{xy} [68].

In classical Drude theory, the magnetoresistance for a system with two carrier species with mobility μ_i and longitudinal conductivity $\sigma_{xx,i}$ can be described by [68, 97]

$$\frac{d^2\rho_{xx}(B)}{dB^2|_{B=0}} = \frac{\sigma_{xx,1}\sigma_{xx,2}}{(\sigma_{xx,1}+\sigma_{xx,2})^2}(\mu_1 \mp \mu_2)^2. \tag{6.5}$$

Here, the sign that adds the mobilities is negative for groups of carriers with the same polarity, such as electron-electron systems, and positive for electron-hole systems. As the charge neutrality point is approached, the densities of holes and electrons become similar. Consequently, $\sigma_{xx,1} \approx \sigma_{xx,2}$, and it follows directly

that the first term $\sigma_{xx,1}\sigma_{xx,2}/(\sigma_{xx,1}+\sigma_{xx,2})^2$ is at its maximum. Therefore, the magnetic field dependence of the resistivity between $-3\,\mathrm{V}$ and $-2\,\mathrm{V}$ in figure 6.6 (a) indicates the approximate position of the CNP.

Figure 6.6 (b) shows the Hall resistivity ρ_{xy} as a function of V_g. When ρ_{xy} crosses the x-axis, the conductivity of the system switches from n- to p-type as the Fermi level passes the CNP at this gate voltage. The result of approximately $-2.4\,\mathrm{V}$ deviates from the result in figure 6.1. However, it is important to consider the distinct mobilities of electrons and holes, in addition to the differences in charge carrier densities. The mobility of the holes in this wafer is one order of magnitude lower than that of the electrons, resulting in a lower contribution to the conductivity. As a result, the position of the CNP can only be estimated approximately using these methods.

The data in figure 6.6 (a) shows one additional feature: A small hump at $0\,\mathrm{V}$, which is also visible in the data of various papers [59, 68, 69] and theses [64, 66]. It has been concluded that this reflects the bottom of the CB edge. Typically, the CB bulk electrons are located near the top surface, and have a mobility which is significantly below that of the Dirac electrons [68]. Here, the bottom of the CB edge lies at roughly $-1.5\,\mathrm{V}$, and due to the electrostatics of the doped wafer, the electrons are located near the bottom surface. However, at $0\,\mathrm{V}$, the 2nd pocket of the curved CB cross-section is filled with additional bulk electrons,

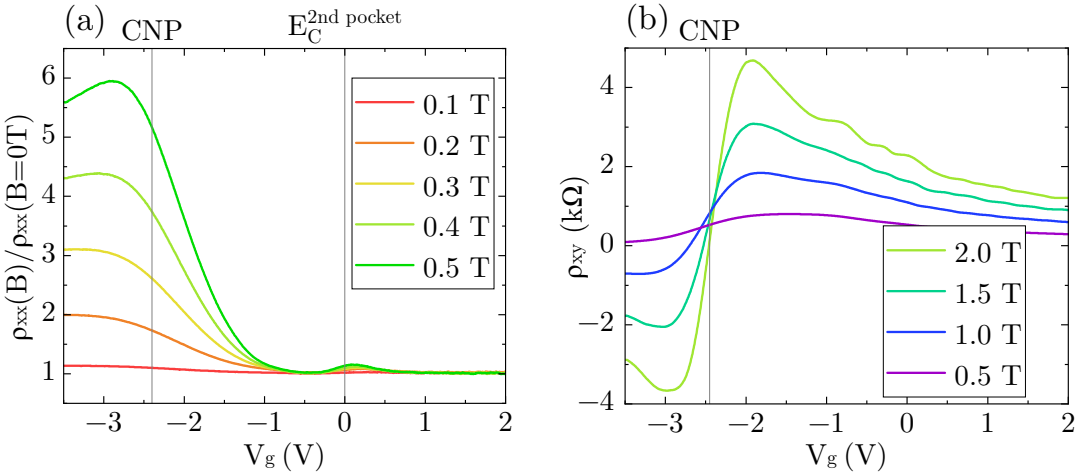

Fig. 6.6.: $\rho_{xy}(B)$ and normalized $\rho_{xx}(B)$ vs V_g. (a) $\rho_{xx}(B)$ normalized to $\rho_{xx}(B=0)$ as a function of gate voltage V_g. The large resistivity between $-3\,\mathrm{V}$ and $-2\,\mathrm{V}$ indicates the approximate position of the CNP. At high magnetic fields the maximum resistivity reaches $1\,\mathrm{M\Omega}$ here. The second, much weaker hump at $0\,\mathrm{V}$ suggests the presence of additional bulk electrons entering the system near the top surface. These electrons originate from the 2nd pocket of the curved CB cross section and the corresponding energy is designated with $E_C^{2nd\ pocket}$. (b) $\rho_{xy}(B)$ as a function of gate voltage V_g. ρ_{xy} approximately changes sign at the gate voltage at which the number of holes and electrons in the system is equal. This occurrence serves as an indication of the CNP. Due to the high electron mobility, quantum Hall plateaus can be seen to the right of the CNP. The measurements were carried out at a frequency of $7\,\mathrm{Hz}$ at $57\,\mathrm{mK}$.

which enter the system near the top surface. Therefore, the hump at 0 V has a similar origin to the one in the given references: It indicates the gate voltage at which bulk electrons from the CB enter the system near the top surface. As two groups of carriers with different mobilities are present, the resistance increases.

6.4. Zero-field capacitance

Figure 6.7 shows the capacitance as a function of the gate voltage at 0 T. Two quantities come into play here: firstly, the quantum capacitance C_Q, exhibiting direct proportionality to the thermodynamic density of states (DOS), and secondly, the geometric capacitance C_{geo}. Both capacitive elements are connected in series. C_Q is much larger than C_{geo}. Due to the series connection of the capacitive elements the smaller geometric capacitance determines the absolute capacitance value. Using equation 3.26 for the capacitance in series and the layer thicknesses of the insulators from figure 4.6, we can estimate the total geometric capacitance. The relative permittivities used for this are taken from the supplemental of reference [39]. The exact values and calculation are recorded in a table in appendix B.1.

The calculation of the **geometric capacitance** yields a result of $C_{geo} = 40.3\,\text{pF}$, which is consistent with the experimental result of 43 pF. The slight difference can be accounted for by various factors: Firstly, the exact layer thicknesses of the insulators (SiO_2 and Al_2O_3) depend on the particular deposition process [111]. The actual values could be different from the assumed values. Even small deviations in insulator thicknesses can cause significant changes in

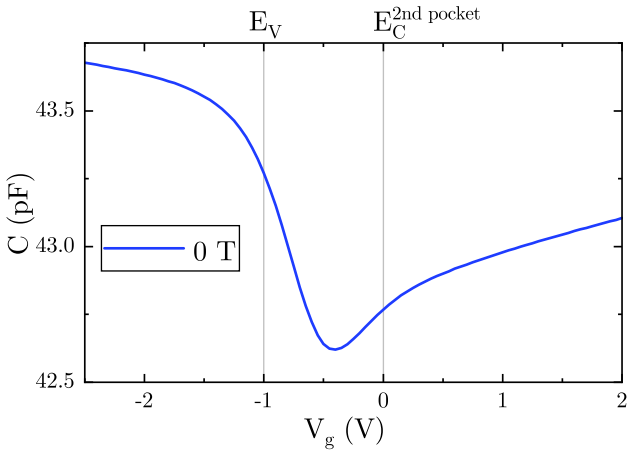

Fig. 6.7.: Zero-field magnetocapacitance as a function of gate voltage. The explanation for the measured capacitance values and the observed shape of the curve results from the different contributions of C_{geo} and C_Q. The measurement for these data were obtained with the AH2700 A bridge at 1.4 K and 60 Hz.

C_{geo}. Secondly, the relative permittivities may differ from the values used. In particular, the value for CdHgTe should be taken with caution since the CdHgTe in the wafer used here is doped. Additionally, there is a finite but unknown contribution from parasitic capacitances, which could explain the difference between experiment and calculation.

In the following, the variation of the capacitance with V_g will be explained. Here the **quantum capacitance** plays a role. The measurement is primarily sensitive to the charge carriers close to the top surface [39]. Coming from negative gate voltages at about $-1\,\mathrm{V}$ the last remaining holes are depleted from the system and the capacitance decreases. The bulk electrons associated with the 2nd pocket of the CB enter the system at $0\,\mathrm{V}$ near the top surface. These additional states, combined with the increasing DOS of the Dirac electrons present on the top surface, lead to a rise in capacitance as a function of positive gate voltage. Therefore, the capacitance displays a minimum at $-0.5\,\mathrm{V}$ and increases towards positive gate voltages. The bulk electrons of the first pocket of the CB, which enter the system at $-1.5\,\mathrm{V}$, sit in close proximity to the bottom surface. Because capacitance measurements primarily probe the uppermost surface, they are not visible in the capacitance of this particular wafer. Furthermore, it is possible that the average centre of the position of the wave function is drawn towards the top surface as the gate voltage increases. The decrease in effective insulator thickness d results in an increase in C_{geo} and, consequently, an increase in the total capacitance.

A comparison can be made between the **filling rate** of the total system and the capacitance. n_{tot} is the average of n_s^{Hall} and n_{high}^{SdH}. The total electron filling rate of the system is then defined as $\alpha_{tot} = {}^{dn_{tot}}\!/_{dV_g}$ which corresponds to the slope of the black, dashed line fit in figure 6.1. A calculation gives $\alpha_{tot} = 2.474 \times 10^{11}\,\mathrm{cm^{-2}\,V^{-1}}$. From this value, the capacitance $C = e\alpha_{tot}A$ can be estimated, with e corresponding to the elementary charge and A to the overlap area of the topgate and mesa (see appendix B.1). The result of $41.8\,\mathrm{pF}$ is consistent with both the experimentally obtained values and the previously calculated geometric capacitance [39].

6.5. Identification of Landau fans

This section provides a qualitative comparison of the QHE and SdH oscillations for both large and small magnetic fields. At high magnetic fields, i. e. above $6\,\mathrm{T}$, only a single Landau fan can be identified, while at lower magnetic fields, the visible features cannot be explained by a single Landau fan.

Despite the fact that an electric current is carried by **different classes of electrons and holes** in HgTe one observes a QHE with well pronounced plateaus at high magnetic fields. The longitudinal and transversal resistivities

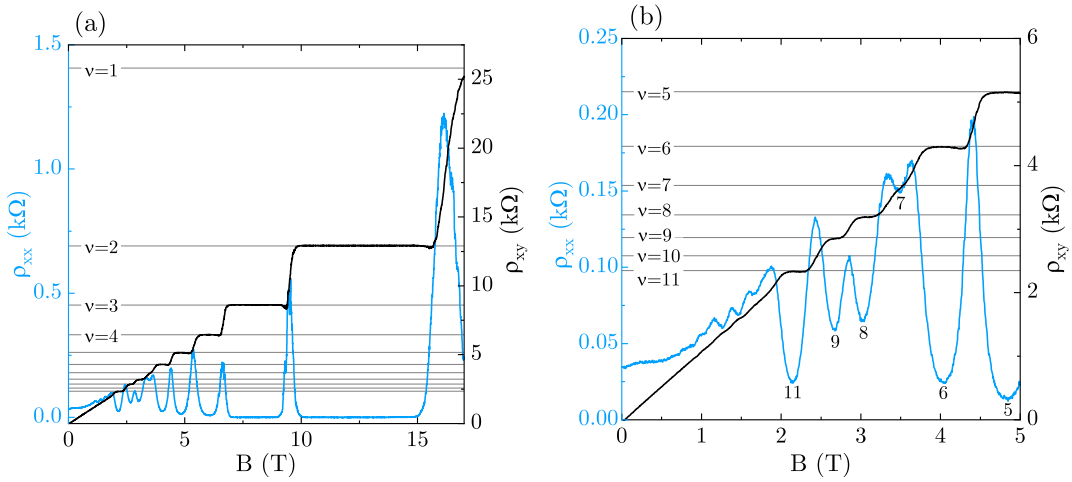

Fig. 6.8.: QHE and SdH oscillations at high and low fields. (a) The black trace shows the ρ_{xy} data. Above 6 T one can see well defined plateaus corresponding to ρ_{xx} minima (blue lines). The filling factor ν is noted on the left side. The grey horizontal lines indicate the theoretical values of R_K/ν. They agree very well with the measured plateaus. (b) At lower magnetic fields the situation becomes more complicated and the clear periodicity of the SdH oscillations is no longer present. Moreover, the peaks sometimes overlap. Some of the quantum Hall plateaus are only faintly visible ($\nu = 7$) or completely missing ($\nu = 10$) while others are still very pronounced. The measurements were obtained at 57 mK, 1.1 Hz and, to prevent heating effects, a current of 10 nA.

vs magnetic field B at $V_g = 0$ V are shown in figure 6.8. Figure (b) is based on the same data as figure (a), but enlarges the range from 0 to 5 T. The distinct periodicity of the SdH oscillations is no longer observed at lower magnetic fields. Additionally, some of the plateaus, including the $\nu = 10$ plateau, are absent. This is due to the corresponding LLs being close to each other. The cyclotron gap between them is too small, resulting in unresolved QHE plateaus and SdH minima. The Fermi level jumps over two LLs simultaneously, causing a change in the filling factor of 2.

Using equation 3.21 for all SdH minima above 2.6 T one obtains a charge carrier density of $5.8 \times 10^{11}\,\mathrm{cm}^{-2}$ at 0 V. This coincides with the result from the Hall slope and therefore reflects the total charge carrier density. At lower magnetic fields three different charge carrier types form Landau fans: top surface, bottom surface and bulk electrons. The different subsystems contribute to the complicated pattern in ρ_{xx} and ρ_{xy} visible in figure 6.8 (b).

The topgate voltage V_g can be varied in order to tune the Fermi energy E_F. This adds a dimension to the graphs and the data can be displayed as **2D colour plots**. Using the tensor inversion of equation 3.5 the conductivity σ_{xx} can be obtained from ρ_{xx} and ρ_{xy}. The colour map shown in figure 6.9 (a) shows the longitudinal conductivity normalized to the respective gate voltage average

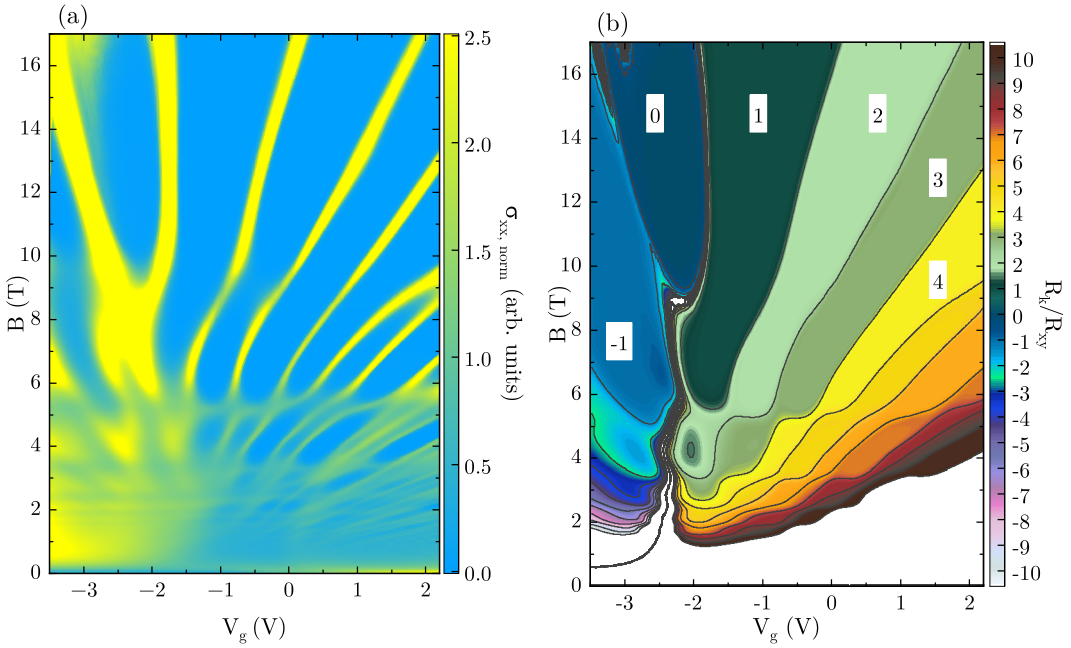

Fig. 6.9.: Colour maps of normalized σ_{xx} and R_K/R_{xy}. (a) 2D colour map of the longitudinal conductivity normalized to the respective gate voltage average as a function of V_g and B. The yellow colour shows area of high conductivity and therefore LLs, blue corresponds to Landau gaps. (b) 2D colour map of R_K/R_{xy}. This allows the determination of the total filling factors ν of the respective Landau gaps. The contour lines, i. e. the black lines which separate the differently coloured areas, are at half-integer filling factors and reflect the centres of the LLs. At low magnetic fields R_K is not quantized anymore. The black line at the bottom left corner of the figure is an artefact of data processing. The data for both graphs were obtained at 57 mK and 1.1 Hz.

$\sigma_{xx,norm} = \frac{\sigma_{xx}}{\bar{\sigma}_{xx}}$[9]. This procedure is done to enhance visibility of the features. The figure reveals a complicated pattern of overlapping Landau fans.

The filling factor, on the other hand, which can be determined from the ratio R_K/R_{xy}, is shown in figure 6.9 (b). For large magnetic fields QHE plateaus with even spacing are well visible. However, similar to the situation in figure (a), the data looks more complicated for small magnetic fields. By comparing the colour maps, one can assign the corresponding filling factors to the Landau gaps.

There is one peculiar feature at about −2.5 V and above 9 T: The filling factor ν is equal to zero in this region. Experimentally, one observes both a very large ρ_{xx} and ρ_{xy}, which yields a transversal conductivity of $\sigma_{xy} = 0$. In Ziegler et al. [69] it is speculated that this could be a magnetic field induced insulator state or a formation of counterpropagating edge states [123–125]. A more detailed investigation of this phenomenon is not part of this work.

Both colour maps show a single well-defined Landau fan at high magnetic

[9]The average $\bar{\sigma}_{xx}$ is calculated by the arithmetic mean: $\bar{\sigma}_{xx} = \frac{1}{n}\left(\sum_{i=1}^{n} \sigma_{xx,i}\right)$ [73].

fields, but a complex situation at low magnetic fields, consisting of several Landau fans. To understand this behaviour, this complicated structure will first be disentangled in the next sections.

6.5.1. Top surface

The fact that the capacitance primarily measures the uppermost layer of charges can be used to determine the LLs belonging to this layer in the conductivity colour map. In this section, it is concluded that below 6 T the capacitance reflects the top surface 2DES of the 3D TI and the corresponding LL in the conductivity are identified.

The capacitance oscillations below 6 T show a clear $1/B$ periodicity. This can be observed, for instance, in the capacitance colour map in figure 6.10. The observed capacitance maxima (yellow) indicate that E_F is in a LL, the capacitance minima (blue) that E_F is in a Landau gap. Towards higher magnetic fields the LLs exhibit increased separation which reflects the $1/B$ periodicity of the oscillations. This periodicity implies that these LLs belong to the same 2DES. The corresponding charge carrier density at 0 V is $1.7 \times 10^{11}\,\mathrm{cm}^{-2}$ which

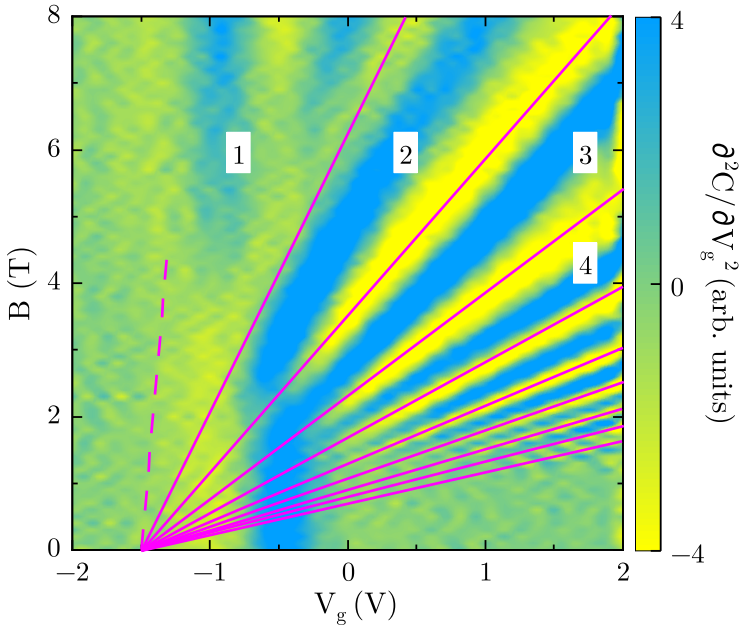

Fig. 6.10.: Colour map of the capacitance. Here, capacitance is shown as the second partial derivative to enhance the visibility of the features. Yellow coloured areas correspond to capacitance maxima which in turn correspond to maxima in the DOS. The numbers in front of the white background are the partial filling factors of the top surface. The magenta lines indicate the LL centres. The lowest LL (dashed magenta line) is not resolved, possibly due to its proximity to the VB edge. The data were collected with the lock-in amplifier setup at 3.1 Hz and at 5 K, to prevent resistive effects.

is less than 30 % of the total charge carrier density. All of this suggests that the primarily probed surface is the top surface, similar to the results in Kozlov et al. [39].

There are two other features in the colour map: Firstly, the capacitance minimum described in section 6.4 becomes visible at −0.5 V and 0 T. Secondly, in the filling factor $\nu = 1$ region, two capacitance minima (blue regions) appear above 6 T, indicating the onset of hybridisation in the system which is discussed in section 6.6.

To identify the LLs in the conductivity colour map that belong to the top surface, it was **compared with the capacitance** colour map. For this purpose, the maxima in the capacitance corresponding to the centres of the LLs were traced with continuous lines (magenta). These lines were then transferred to the conductivity colour map in figure 6.11 (a). The lines indicate LL centres which are present in both plots. These are periodic in V_g and $1/B$ and converge to a point at −1.5 V.

The point of origin at −1.5 V is the virtual Dirac point. As the Fermi level enters the valence band at −1 V, the filling rate of the top surface inevitably

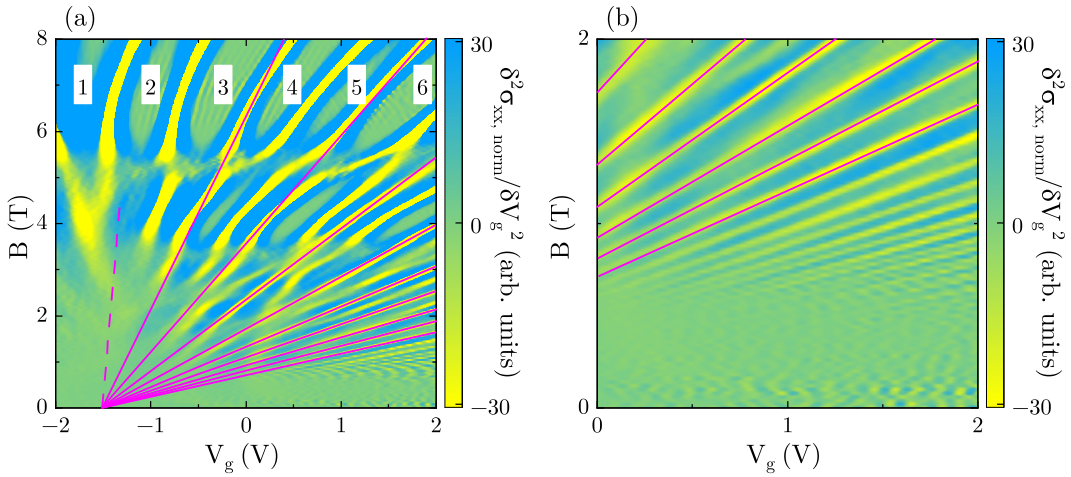

Fig. 6.11.: Identification of top surface LL by capacitance. (a) Colour map of the second partial derivative of the longitudinal conductivity normalized to the gate voltage average. Yellow lines correspond to the centres of the LLs, blue and greenish striped regions are Landau gaps where one measures the quantum Hall plateaus. The striped areas (such as at 0 V and 8 T) appear due to data processing and are not present in the original data. The magenta lines indicate the LL centres that can be observed in both this colour map and the capacitance colour map. The numbers in front of the white background differ from the capacitance colour map as they represent the total filling factor here. (b) Enlargement of a section of the graph on the left-hand side reveals additional well-resolved LLs that were not resolved in the capacitance colour map. As explained in the subsequent text, all of these are $1/B$ periodic and pertain to the top surface. The data for both graphs were obtained at 57 mK and 7 Hz.

changes. This leads to a kink in the Landau fan, which however cannot be observed here due to lack of resolution. The actual Dirac point of the top surface is buried deep in the valence band [69]. To highlight this fact, the point at −1.5 V is referred to as virtual.

For magnetic fields below 1.5 T, the LLs are not resolved in the capacitance colour map. For the conductivity colour map, the resolution limit is approximately 0.6 T. If the strict periodicity in $1/B$ is used, the expected positions of the top surface LL can be extrapolated towards lower magnetic fields. This was done here and confirms that all LL visible in the conductivity at positive gate voltages and magnetic fields below 1.5 T, as shown in figure 6.11 (b), stem from the top surface.

When measuring capacitance as a function of magnetic field, oscillations are observed, as shown in figure 6.3. The minima occur at integer filling factors of the top surface. Plotting these minima as a function of the inverse magnetic field should ideally result in a straight line, as seen in figure 6.12 (a). This allows for extraction of the charge carrier density of the probed 2DES. Additionally, the phase δ of the quantum oscillations can be determined by [59]

$$\frac{1/B_{min,\nu}}{\Delta_{1/B}} = \nu + \delta, \tag{6.6}$$

where $B_{min,\nu}$ is the minimum of the oscillation corresponding to filling factor ν and $\Delta_{1/B}$ is the oscillation period on a $1/B$ scale. For a conventional 2DES

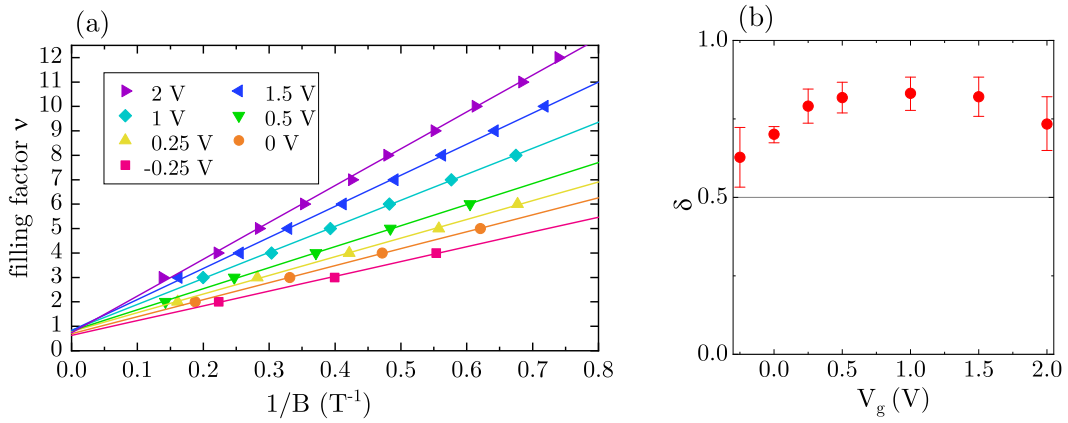

Fig. 6.12.: Capacitance minima and quantum phase. (a) Capacitance minima as a function of the inverse magnetic field. Only data below 8 T were used. A linear fit confirms that for a fixed gate voltage the data points lie on a straight line. The minima above 8 T were deliberately not considered here. These lie below the linear fit due to the hybridization of the system discussed in section 6.6. (b) The quantum phase δ and the corresponding standard error of the capacitance oscillations as a function of V_g. The data were obtained from the intersection of the linear fit with the y-axis in the left-hand plot. Due to the topological nature of the top surface electrons and a small contribution from the bulk electrons the result here is $\delta > 0.5$ [39].

one expects a phase of $\delta = 0$. However, for Dirac fermions the phase is ideally $\delta = 0.5$, since electrons acquire a Berry phase in the magnetic field [126].

The observed values here are slightly above 0.5 due to the topological nature of the top surface electrons and a small contribution from the bulk electrons. This result is consistent with the findings in Kozlov et al. [39]. Additionally, this paper shows that the phase drops to 0 when the Fermi energy enters the valence band. The absence of this feature in the data presented in figure 6.12 (b) is in line with the fact that the VB edge is at $-1\,\mathrm{V}$, which is below the gate voltage at which the first oscillations in the capacitance become visible.

Overall, these results confirm that below 6 T the capacitance primarily probes Dirac-like states and consequently the 2DES of the top surface.

6.5.2. Bottom surface

Figure 6.13 displays a 2D colour map of the second derivative of the longitudinal conductivity. The data were derived with respect to the magnetic field instead of the gate voltage, revealing horizontal lines that we ascribe to LLs stemming

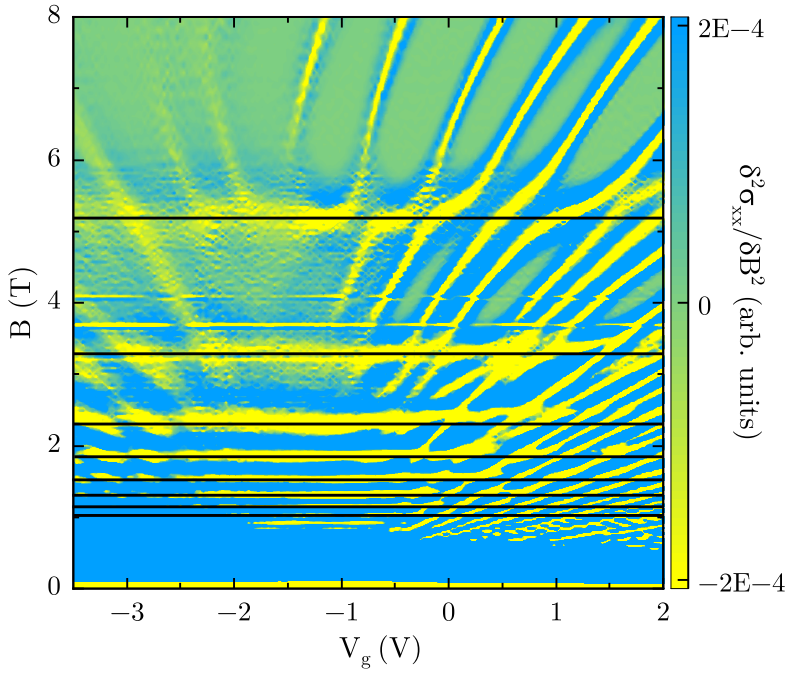

Fig. 6.13.: Identification of the bottom surface LLs. The colour map shows the longitudinal conductivity, differentiated twice with respect to the magnetic field. The LL (yellow) belonging to the bottom surface were indicated with black lines. Two horizontal lines at 3.65 T and 4.05 T can also be seen which are visually distinct from the LLs. These are artefacts that occurred during the measurement and are of no further concern. The data were obtained at 57 mK and 7 Hz.

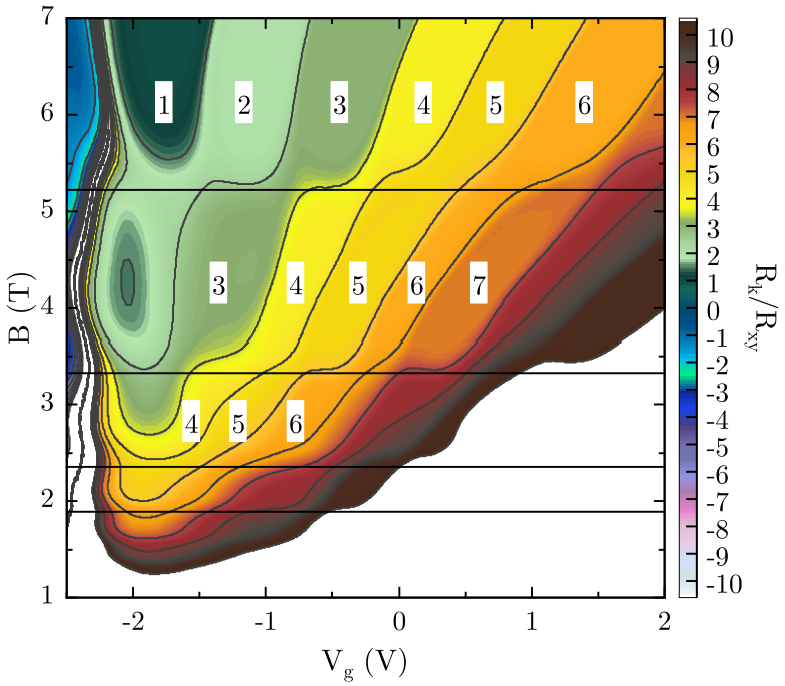

Fig. 6.14.: Colour map of R_K/R_{xy} to determine the filling factors. The black horizontal lines indicate the LL centres and were copied from figure 6.13. The bottom surface LLs are accompanied by a change in the filling factor which, together with the other LLs, results in the visible parallelogram-like pattern. The data were obtained at 57 mK and 7 Hz.

from the bottom surface[10].

Due to the electrostatics of the doped wafer the bottom of the CB is below the top of the valence band. There are always mobile charge carriers available from the top surface or bulk. These **electrostatically shield** the bottom surface LLs from the influence of the topgate. Therefore, the LLs appear at constant magnetic fields.

The horizontal features in the conductivity are accompanied by a change in the filling factor, as shown in figure 6.14. This confirms the existence of horizontal LLs, which, together with the LL of top surface and bulk electrons, create a parallelogram-like pattern. The pattern is particularly visible between 3.3 T and 5.2 T.

In the conductivity colour map in figure 6.13, the LLs of the bottom surface at positive gate voltages are partially concealed by the LLs of the top surface and the bulk. Figure 6.15 compares the conductivities at constant magnetic fields. The curve at 5.2 T corresponds to the magnetic field strength at which E_F is in the last visible LL associated with the bottom surface. Therefore, at this configuration there is a large DOS stemming from the bottom surface and,

[10]The visibility of the horizontal LLs is not improved by taking a derivative with respect to the gate voltage, as this makes them parallel to the derivative direction.

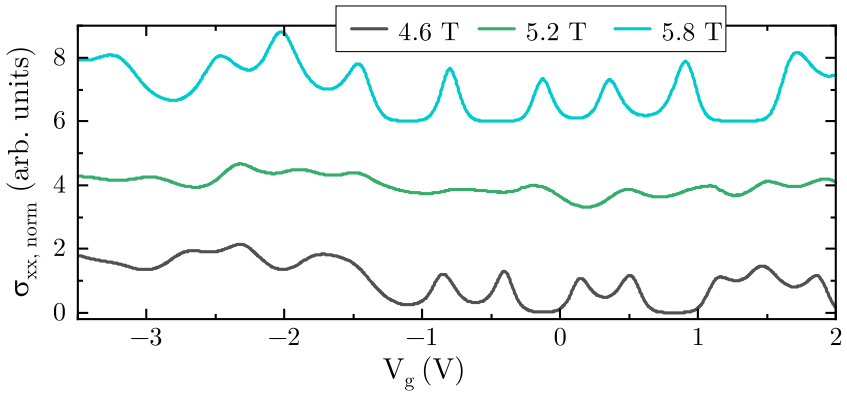

Fig. 6.15.: Waterfall plot of the normalized conductivity as a function of gate voltage at fixed magnetic fields. The curves have been shifted vertically to increase visibility. The curves were measured at 57 mK and 7 Hz.

consequently, a high conductivity of the electrons residing on the bottom surface. To obtain the total conductivity, the conductivities of the respective 2D systems are summed up. The high conductivity of the bottom surface attenuates the visibility of the oscillations of the top surface and bulk. In conclusion, at 5.2 T one moves along the LL resulting in a rather constant conductivity value. At 4.6 T and 5.8 T, on the other hand, one sees curves that are significantly more modulated by LLs stemming from other 2D electron systems or the 2D hole system. This suggests that the bottom surface LLs extend over the entire gate voltage range.

The filling rate of the bottom surface is below an experimentally determinable value which implies a constant charge carrier density. The carrier density was calculated by evaluating the $1/B$ periodicity of the LLs in figure 6.13. The result of $2.3 \times 10^{-11}\,\mathrm{cm}^{-2}$ coincides with the result $n^{SdH}_{low-f_2}$, which was obtained by the Fourier spectroscopy in section 6.1.2.

The bottom surface LL only become clearly visible after a number of data processing steps, such as differentiating twice with respect to the magnetic field. As a result, it was not possible to determine the exact positions of the minima. A determination of the carrier density is still possible, as explained in the preceding paragraph. However, the precision required to determine the Berry phase of the bottom surface is not given.

Equation 3.20 can be used to determine the magnetic field values at which the bottom surface LLs should lie based on the known charge carrier density. It is expected that one more LL of the bottom surface will appear between 9 T and 10 T, but it is not visible in any of the conductivity colour plots. Furthermore, there is no change in the filling factor at this magnetic field interval. This is believed to be a result of the ongoing hybridisation of electron systems at these high magnetic fields, as the LL is already part of the merging system. More information can be found in section 6.6.

6.5.3. Bulk holes

The analysis so far has focused on the LL of the electron systems. Additionally, the density of states of the valence band's **two-dimensional hole system** (2DHS) forms hole LLs when subjected to a perpendicular magnetic field. These LLs are spin-degenerate at low magnetic fields [69]. Analysing the LLs at high magnetic fields is challenging due to the occurrence of spin splitting and the hybridization of the system. The objective of this section is to estimate the hole carrier density. Therefore, the focus is on low magnetic fields below 4 T, where the LL exhibit a clear pattern.

Figure 6.16 (a) displays the second derivative of the longitudinal conductivity at negative gate voltages, revealing the LL originating at the VB edge at −1 V and fanning out towards negative gate voltages. Figure 6.16 (b) presents the corresponding filling factors in this region. The black contour lines at half-integer filling factors indicate the centres of the LLs. Between −2.5 V and −3.5 V it is noticeable that the filling factor changes by 2 for each LL, supporting the spin degeneracy of the bulk holes from the CB in the displayed regime. Additionally, the LL exhibit periodicity in $1/B$. Taking into account the spin degeneracy, the charge carrier density p^{SdH} can be determined using equation 3.20. This yields the results shown in figure 6.1.

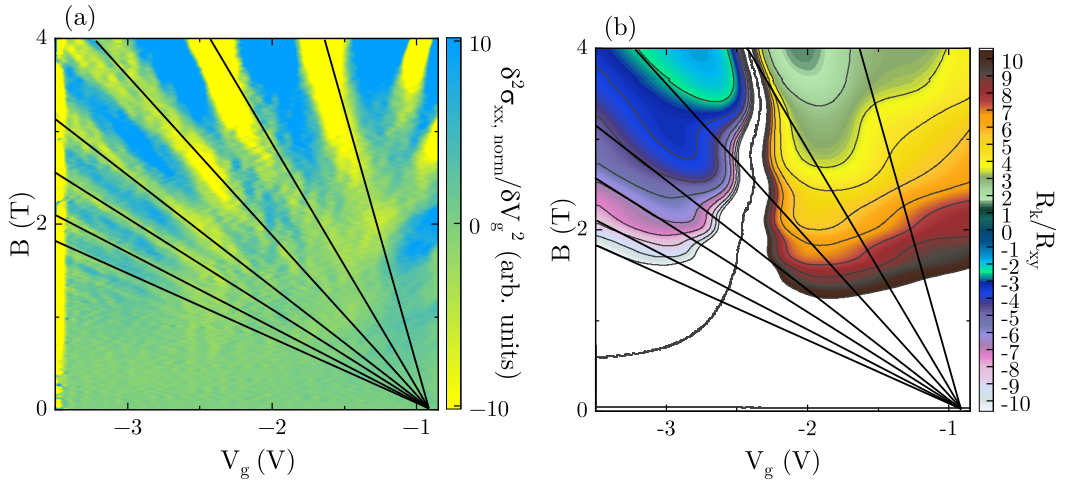

Fig. 6.16.: Identification of bulk hole LL. (a) Colour map of the second partial derivative of the longitudinal conductivity normalized to the gate voltage average. The LL stemming from the 2DHS are indicated by black lines. These originate from the VB edge at −1 V. (b) Colour map of R_K/R_{xy}. At −3.5 V the filling factor changes by 2 for each LL. This is due to the spin degeneracy of the 2DHS at low fields. The black line in the centre of the figure is an artefact of data processing. The data for both graphs were obtained at 57 mK and 7 Hz.

6.5.4. Bulk electrons

Identifying the LLs stemming from the bulk electrons turns out to be a challenging task due to close proximity of E_C^* and the virtual Dirac point of the top surface.

Figure 6.17 displays the second derivative of the longitudinal conductivity. The magenta lines represent the LL which coincide with the capacitance, and therefore belong to the top surface. The horizontal LL of the bottom surface are not visible, since the data has been derived with respect to the gate voltage. The LLs that have not yet been identified are ascribed to the bulk electrons of the CB. They are marked with black lines.

The position of the CB edge E_C^* can be determined by extrapolating the LLs of the bulk carrier electrons towards $B = 0$, similar to how the virtual Dirac point of the top surface was determined. It is expected that the filling rate of the bulk electrons will decrease when entering the VB at $-1\,\mathrm{V}$. Therefore, linear extrapolation of the data for the bulk electrons is of limited use, and the actual position of E_C is unknown in this doped wafer. To emphasize this point, the corresponding abbreviation E_C^* is marked with an asterisk [59, 64].

Furthermore, there is a region of increased conductivity in the centre of the figure, indicated by a single black line. This is likely the second pocket of the CB emerging at 0 V. A Landau fan pattern cannot be identified for it.

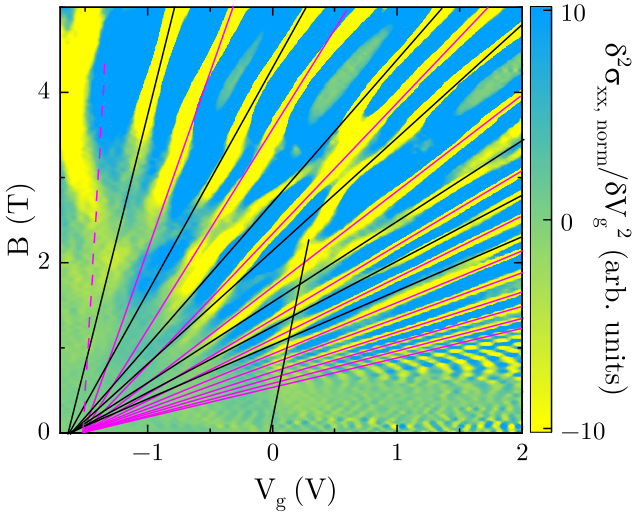

Fig. 6.17.: Identification of bulk electron LL. The colour map shows the second partial derivative of the normalized longitudinal conductivity. The black continuous lines mark the LL which belong to the bulk and have their origin at the virtual CB edge $E_C^* = -1.6\,\mathrm{V}$. These were identified using a simple exclusion principle, since they cannot be assigned to either the top surface (magenta) or the bottom surface. In addition, a region of increased conductivity which originates at 0 V can be seen. It originates from the 2nd pocket of the CB. The data were obtained at 57 mK and 7 Hz.

The LL above 3 T are $1/B$ periodic. Below 3 T they exhibit some imperfections. It is assumed that this is due to the inconsistent separation between the LL of the bulk and the LL of the top surface, resulting in complete or partial overlap. Therefore, the carrier density analysis has been conducted for the four visible LL lowest in energy. This corresponds to the LL at the highest magnetic fields in the figure. A comparison with figure 6.14 reveals that at 5 T, the filling factor changes by 1 for each bulk electron LL. This suggests that the LL are spin-resolved, which allows for an estimation of their carrier density. The obtained values are slightly lower than the data reported in figure 6.1, which was calculated using the electron density difference $n^{bulk} = n_s^{Hall} - \left(n^{Cap} + n_{low-f_2}^{SdH}\right)$. The small difference of 10 % may be attributed to the second pocket of the CB.

6.6. Merged system at high fields

This section investigates the behaviour of the conductivity and capacitance at high magnetic fields, specifically above 6 T.

Figure 6.18 shows the second derivative of the longitudinal conductivity as a 2D colour map, with data analysed up to a magnetic field of 17 T. At high magnetic fields, the complicated and overlapping Landau fans are no longer visible. Instead, only a few LLs with regular spacing can be observed. The LL centres are marked with dashed lines. These lines can be extrapolated to $B = 0$ T using straight, black continuous lines. The point of origin, roughly at -2.3 V, is the CNP. The single Landau fan reflects the total charge carrier density. In section 6.5.1, the LLs marked with magenta were assigned to the top surface, and it was concluded that they reflect its charge carrier density.

Figure 6.19 displays the second derivative of the capacitance for high fields up to 17 T. The magenta lines indicate the top surface LL. The dashed black lines represent the three LL centres determined by the conductivity, while the continuous lines show their extrapolation to $B = 0$ T. These lines were directly copied into the capacitance colour map.

Interestingly, above 14 T, the dashed lines indicating conductivity maxima coincide with the capacitance maxima, suggesting that the capacitance follows the transport data. At high magnetic fields, the capacitance Landau fan now reflects the total charge carrier density, not just that of the top surface. The bottom line is: In the regime of low magnetic fields, approximately between 0 and 6 T, distinct electron **carrier subsystems coexist**. These subsystems weakly interact, contributing almost independently to the total conductivity. As a result, each subsystem generates its own Landau fan, which can be observed as complex patterns in the conductivity colour map. As the magnetic field increases, the charge carriers are **redistributed**, approximately between 6 and

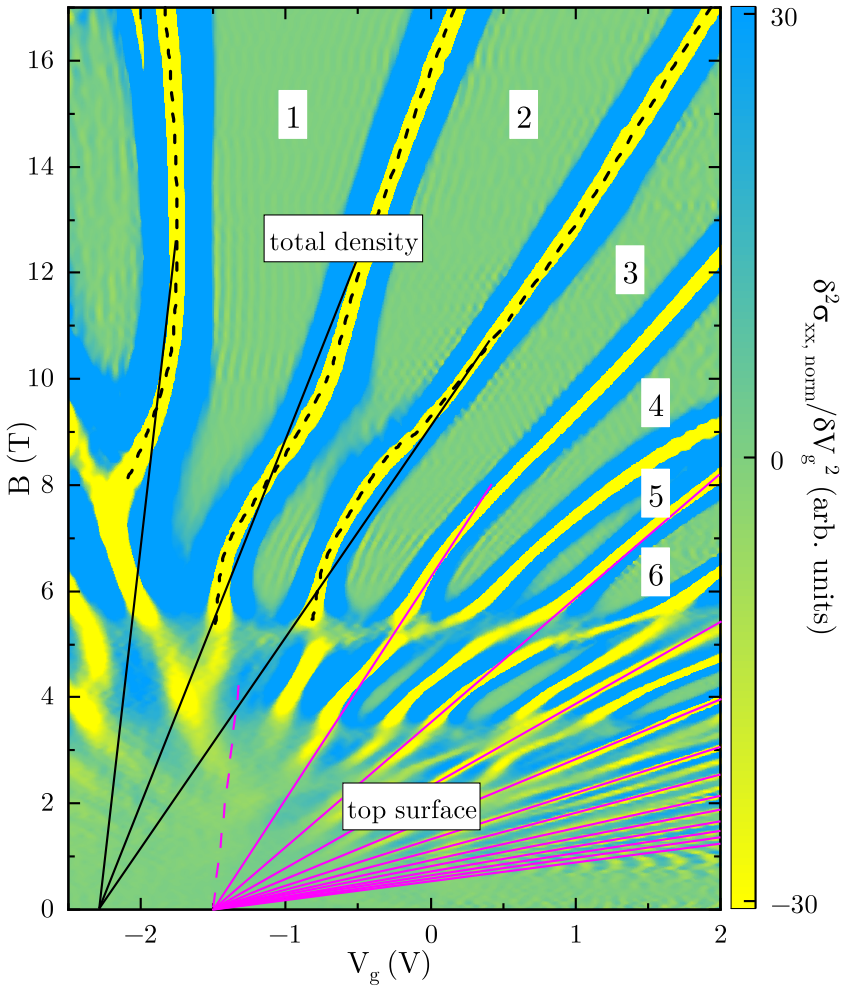

Fig. 6.18.: Colour map of the second partial derivative of the longitudinal conductivity normalized to the gate voltage average for high fields. At the bottom right is the top surface Landau fan, which originates −1.5 V (magenta). The centres of the three visible LLs at large magnetic fields are indicated by black, dashed lines. These lines are extrapolated towards 0 T and −2.3 V by black continuous lines. The resulting Landau fan originates from the CNP and reflects the total charge carrier density. The numbers on the white background indicate the total filling factor. The data were obtained at 57 mK and 1.1 Hz.

14 T. Finally, above 14 T, **all electron systems are merged** and only a single Landau fan survives, which originates from the CNP. This Landau fan reflects the total charge carrier density.

The behaviour described above is also evident in the filling factor. At low magnetic fields, the conductivity filling factor is determined by R_K/R_{xy}, as shown in figure 6.9 (b). This is the total filling factor, i. e. the number of filled LLs of all 2D electron and hole systems. In contrast, the filling factor of the top surface at low fields is determined by the intersection of the linear fit of the capacitance minima with the y-axis, as shown in figure 6.12 (a). There, the successive minima are plotted as a function of the inverse magnetic field.

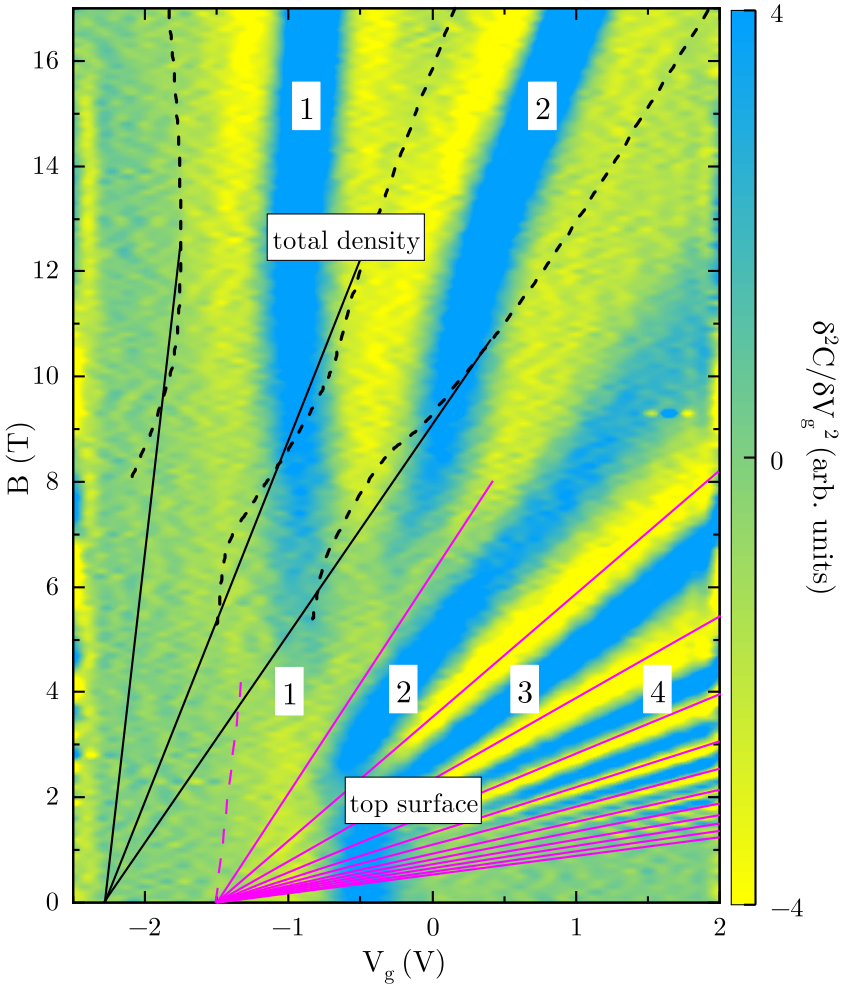

Fig. 6.19.: Colour map of the second partial derivative of the capacitance for high fields. The dashed and continuous lines from figure 6.18 have been transferred to this colour map. The numbers on the white background within the magenta indicate the partial filling factor of the top surface, while the numbers at large fields indicate the filling factor of the merged 2D system. To prevent resistive effects that can occur in the presence of large magnetic fields, the entire measurement was carried out using the lock-in amplifier setup at low frequencies of 3.1 Hz and at 5 K.

Additionally, the minima are assigned sequential integer filling factors. The filling factors of the top surface can then be determined as the linear fit of the data points must intersect the Y-axis between 0 and 1, given that the quantum phase for the Dirac fermions of the top surface is 0.5 (as shown in figure 6.12 (b)). In the event that the intersection point falls outside the specified range, all data points are collectively shifted by an integer value until the required condition is met. This procedure was utilized to determine the filling factors of the top surface from the capacitance at low fields. In conclusion, at low magnetic fields, the LL gaps observed in the capacitance are associated with the partial filling factor of the top surface, whereas the LL gaps observed in the conductivity are associated with the total filling factor of all 2D systems. However, at high

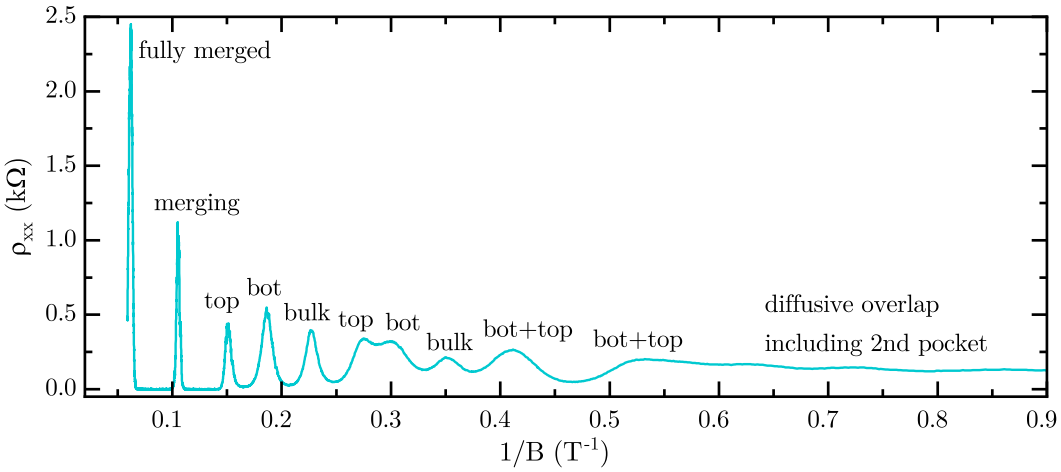

Fig. 6.20.: Assignment of SdH peaks to the 2DES of origin. Shown is ρ_{xx} as a function of the inverse magnetic field $1/B$ at 0 V. For each peak in the graph the corresponding origin was denoted. At 0.41 T^{-1}, the colour maps show both the presence of a bottom surface LL and a top surface LL. This agrees with the statement in section 6.5, where it was concluded that the filling factor here increases by two, from 9 to 11. For magnetic fields smaller than 2 T (or larger than 0.5 T^{-1}) the resolution of the colour maps is no longer sufficient for a definite assignment of the peaks to their respective origin. In addition, the electrons of the 2nd pocket of the CB contribute to the conductivity. At even smaller magnetic fields the system becomes diffusive. The data were obtained at 57 mK and 1.1 Hz.

magnetic fields, the filling factors for both the conductivity and capacitance coincide, reflecting the same number of filled LL of the remaining single 2D system.

Capacitance measurements below 6 T probe the top surface, while above 14 T, the system is fully merged and capacitance probes the total carrier density of the merged system. In between, the capacitance does not follow any of the black, dashed LL centres determined by the conductivity. This reflects the redistribution of charge carriers in this magnetic field interval. However, the exact behaviour of the capacitance is unclear at present. Furthermore, the merging of the electron systems above 6 T explains the missing lowest bottom surface LL. It was expected to appear between 9 T and 10 T, but the system is already merging at these fields.

Figure 6.8 displayed the QHE and SdH oscillations from $0-17$ T at $V_g = 0$ V. The data revealed well-pronounced plateaus and peaks at high fields, but a complex pattern at low fields. In this and the previous sections, all LLs were identified, and the merging process of the systems was revealed. This allows each SdH peak to be assigned its corresponding origin, i. e. the 2D system of origin. This is shown in the figure 6.20.

7. Superconductivity

A good introduction to superconductivity can be found in the book by Rudolf Gross and Achim Marx [43]. A more theoretical but very precise description is provided by Michael Tinkham [127]. Wördenweber et al. [128] writes specifically about "Superconductors at the Nanoscale", and Victor Moshchalkov and Joachim Fritzsche about "Nanostructured Superconductors" [33]. All four books were consulted when writing this chapter. The first section on Ginzburg-Landau theory primarily uses the book by Gross and Marx, while the other two sections on vortices and flux pinning are strongly orientated towards the work by Moshchalkov and Fritzsche.

Superconductivity is a quantum mechanical phenomenon that, interestingly, can be observed on macroscopic length scales. Below a critical temperature T_c, the electrical resistance in a superconductor drops to absolutely zero. The niobium (Nb) used in this work has, provided an appropriate degree of purity, the highest critical temperature of all elements at normal pressure, which is $T_c = 9.25\,\mathrm{K}$ [129]. Superconductors have a second important property: they completely displace an external magnetic field and are therefore perfect diamagnets. This effect is called the Meißner-Ochsenfeld effect and distinguishes superconductors from ideal conductors that only exist in theory [130]. However, just like the temperature, a magnetic field that is too strong can also break the

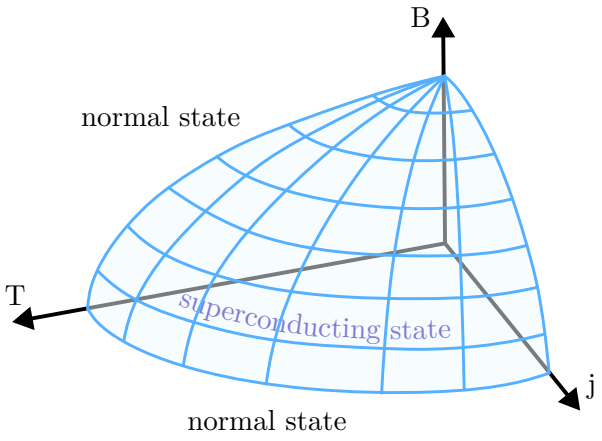

Fig. 7.1.: 3D phase diagram of the critical surface as a function of temperature T, magnetic field B, and current density j. The superconducting state can only exist within the envelope (light blue, transparent), while outside the envelope, conductivity is normal, resulting in a finite resistance (completely redrawn, the original comes from [33]).

superconductivity. Finally, superconductivity can also be broken by electric currents. Above a critical current density the superconducting state is lost. The 3D phase diagram of the critical surface as a function of the mentioned quantities is sketched in figure 7.1.

This chapter is divided into three sections. The first section discusses the Ginzburg-Landau theory and the results obtained from it. The second section describes the structure and behaviour of vortices in the superconductor. The third section covers the pinning of vortices, i. e. confining them to specific positions, and the physical effects involved.

7.1. Ginzburg-Landau theory

The physical phenomena observed in this work can be well described by the Ginzburg-Landau (GL) theory, named after Vitaly Ginzburg and Lev Landau and published in 1950 [8]. It is sometimes also referred to as the GLAG theory to acknowledge the contributions of Alexei Abrikosov and Lev Gor'kov.

In this thesis this description of superconductivity is suitable because, on the one hand, it can be used to describe situations with spatially varying density of superconducting electrons and supercurrents. Such a situation can be found, for example, in type-II superconductors, in the investigated Nb antidot lattices, or at the interface between Nb and HgTe. On the other hand, the macroscopic GL theory constitutes a limiting case of the microscopic BCS (Bardeen-Cooper-Schrieffer) theory near the superconducting transition temperature T_c. Since the effects observed in chapter 8 have largely been measured near the transition temperature, the GL theory is applicable in this case [43].

The derivation of the GL theory is described in detail and comprehensibly in the books mentioned in the introduction to this chapter. A summary would not do justice to this complex topic. However, a detailed description would again go beyond the scope of this work, so it is not included here. Instead, the important results are presented directly and the conclusions are drawn.

7.1.1. Ginzburg-Landau equations

Although the GL theory is based on a fundamentally phenomenological approach, it proved to be highly successful. Ginzburg and Landau calculated an expression for the free energy F of a superconductor using a **complex order parameter** Ψ. This order parameter can vary spatially and its absolute square $|\Psi(\mathbf{r})|^2$ is a measure for the density of the superconducting electrons $n_s(\mathbf{r})$. For a normal conductor, Ψ would be zero, whereas for a superconductor it is finite. Ψ_0 describes the order parameter in field-free space, for example infinitely deep in the superconductor.

If F is minimised with respect to variations in Ψ, this results in the **1. Ginzburg-Landau equation** [128]:

$$\alpha\Psi + \beta|\Psi|^2\Psi + \frac{1}{2m^*}\left(-\mathrm{i}\hbar\boldsymbol{\nabla} + 2e\mathbf{A}\right)^2\Psi = 0. \tag{7.1}$$

Here, α and β are phenomenological parameters, where $\alpha = \alpha(T)$ is linearly dependent on temperature, while β is temperature independent. Moreover, m^* is the effective mass of a Cooper pair[11], $2e$ corresponds to the charge of a Cooper pair and $\mathbf{A}$ is the magnetic vector potential. Minimising F with respect to this vector potential $\mathbf{A}$ leads to the **2. Ginzburg-Landau equation**, which describes the electric current density $\mathbf{j}$ [128]:

$$\mathbf{j} = -\frac{2e}{m^*}\,\mathrm{Re}\left\{\Psi^*\left(-\mathrm{i}\hbar\boldsymbol{\nabla} + 2e\mathbf{A}\right)\Psi\right\}. \tag{7.2}$$

The real part of the complex function in the curly brackets is denoted by Re. The Ginzburg-Landau equations can be used to describe superconductivity with local variations of the magnetic field $\mathbf{B}$ and local variations of n_s.

7.1.2. Characteristic length scales

The abstract, phenomenological parameters α and β can be replaced by two actually observable, characteristic length scales. The first is the Ginzburg-Landau **coherence length**, ξ_{GL}, which represents the length scale over which the superconducting order parameter can vary. It is found that [43]

$$\xi_{GL}(T) = \sqrt{\frac{\hbar^2}{2m^*\alpha(T)}} = \frac{\xi_{GL}(0)}{\sqrt{1-\frac{T}{T_c}}}. \tag{7.3}$$

As can be seen from the second part of the equation, the coherence length depends on the temperature T and the transition temperature T_c.

The second characteristic length scale is the Ginzburg-Landau **penetration depth** λ_{GL}. It is a measure of the length at which an external magnetic field decays in a superconductor. λ_{GL} is also temperature-dependent and the following applies [43]

$$\lambda_{GL}(T) = \sqrt{\frac{m^*\beta}{4\mu_0 e^2\alpha(T)}} = \frac{\lambda_{GL}(0)}{\sqrt{1-\frac{T}{T_c}}}, \tag{7.4}$$

where μ_0 is the vacuum magnetic permeability. The magnetic field and order parameter at a superconductor-normal conductor interface are shown in figure 7.2.

[11] A Cooper pair consists of two electrons that interact with each other via phonons. It is used in the BCS theory to explain the occurrence of superconductivity.

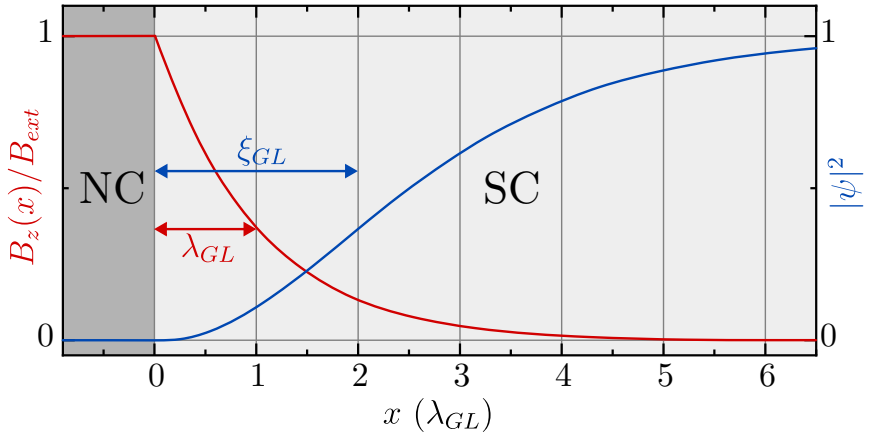

Fig. 7.2.: Behaviour of the magnetic field and the order parameter at a superconductor (SC, light grey) - normal conductor (NC, dark grey) interface. The magnetic field, which is perpendicular to the superconducting plane and normalised to the external field B_{ext}, decays with λ_{GL} (red). $\psi = \Psi/\Psi_0$ is the normalised order parameter. Its absolute square $|\psi|^2$ (blue) changes with ξ_{GL}. For the purpose of illustration, this figure shows $\xi_{GL} = 2\lambda_{GL}$. The so-called proximity effect, i. e. that the superconductivity can enter the NC to a certain extent, is neglected here (adapted from [43]).

It can be noted that if $\frac{\alpha(T)}{\beta} = |\Psi_0|^2 = n_s$ is inserted in equation 7.4, the London penetration depth λ_L is obtained, which was already derived in 1935 by Fritz and Heinz London [131].

7.1.3. Type-I and type-II superconductors

With the two characteristic length scales described in the previous section, the **Ginzburg-Landau parameter** κ can be defined:

$$\kappa \equiv \frac{\lambda_{GL}(T)}{\xi_{GL}(T)} = \sqrt{\frac{\beta}{2\mu_0}}\frac{1}{\mu_B}, \tag{7.5}$$

where μ_B is the Bohr magneton. The purpose of this parameter is that two different types of superconductors can be distinguished:

$$\kappa \leq \frac{1}{\sqrt{2}} \qquad \textbf{type-I} \text{ superconductor} \tag{7.6}$$

$$\kappa \geq \frac{1}{\sqrt{2}} \qquad \textbf{type-II} \text{ superconductor} \tag{7.7}$$

Type-I superconductors have a thermodynamic critical field B_{cth} that separates the superconducting state from the normal conducting state. The field-free superconducting state is also known as the Meißner state, named after Walther Meißner.

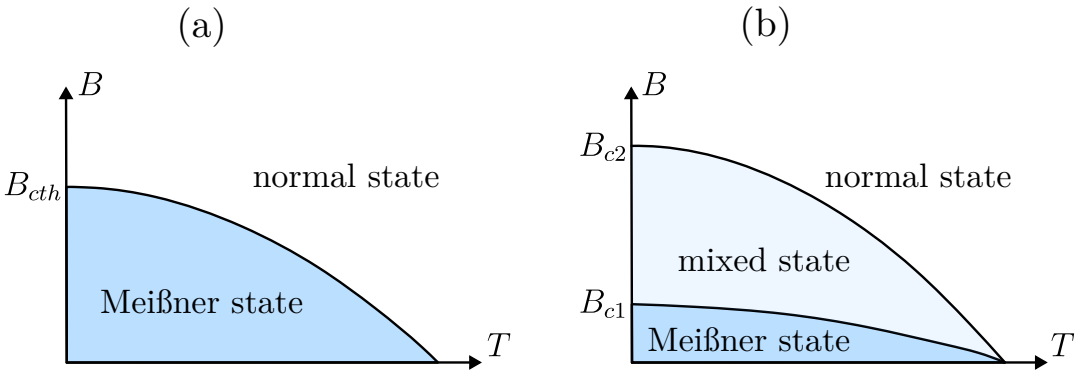

Fig. 7.3.: (a) Phase diagram of a type-I superconductor. The thermodynamic critical field separates the Meißner state from the normal state. (b) Phase diagram of a type-II superconductor: there is an additional mixed state between the upper and lower critical field.

In type-II superconductors, on the other hand, there is a lower critical field B_{c1} and an upper critical field B_{c2}. Below B_{c1} is the Meißner state and above B_{c2} is the normal conducting state. In these regimes, type-I and type-II superconductors behave analogously. It becomes interesting when the field lies between the lower and upper critical field: This regime is also called **mixed state** or Shubnikov phase after Lev Shubnikov.

The calculation of the SC/NC interfacial energy reveals a negative value for type-II superconductors in the mixed state. This implies that the superconductor can minimise its total energy by creating as many interfaces as possible. It is therefore energetically favourable for type-II superconductors in this regime to behave in an interesting way: There are still connected, superconducting areas. In these, however, separate areas are formed in which the superconductor is penetrated by magnetic flux. This was recognised by Alexei Abrikosov and published in 1957 [9, 43, 128]. The phase diagrams of type-I and type-II superconductor are sketched in figure 7.3.

The magnetic flux that penetrates the superconductor is quantized, resulting in **superconducting flux quanta**, i. e. $\Phi_0 = h/2e$[12]. The double elementary charge in the denominator corresponds to the charge of the Cooper pairs in the BCS theory, which consist of two electrons. This quantization of the magnetic flux was experimentally demonstrated by Doll and Näbauer [132] and by Deaver and Fairbank [133], independently of each other. Both Abrikosov's work and the behaviour of the superconducting flux quanta will be discussed in detail in the next sections of this chapter. However, before that, the critical fields will be briefly discussed. The two critical fields B_{c1} and B_{c2} are related to the physical quantities described so far as follows: The **lower critical field** B_{c1} is given

[12] in contrast to $\Phi_0^m = h/e$, which is referred to as magnetic flux quanta in this work and plays a role in the Landau levels in the QHE.

by

$$B_{c1} = \frac{\Phi_0}{4\pi\lambda_L^2}(\ln\kappa + 0.08). \tag{7.8}$$

It occurs when the first flux quantum enters the superconductor. The **upper critical field** B_{c2} is given by

$$B_{c2} = \frac{\hbar}{2e\xi_{GL}^2} = \frac{\Phi_0}{2\pi\xi_{GL}^2}. \tag{7.9}$$

The temperature-dependent Ginzburg-Landau coherence length $\xi_{GL}(T)$ can therefore be determined directly from measurements of the upper critical magnetic field with

$$\xi_{GL}(T) = \sqrt{\frac{\Phi_0}{2\pi B_{c2}(T)}}. \tag{7.10}$$

7.2. Vortices

This section provides a detailed description of superconducting flux quanta in type-II superconductors, which are also known as vortices. The term 'vortex' is appropriate as it refers to the fact that a single vortex consists not only of the magnetic flux but also of the associated circular shielding currents.

7.2.1. Structure of a single vortex

As previously stated, the magnetic flux within a vortex is quantized, with its value corresponding to the superconducting flux quantum Φ_0. The local magnetic field $\mathbf{B}(\mathbf{r})$ decreases with increasing distance from the vortex centre over the length λ_{GL}, as shown in figure 7.4 (b). The exact mathematical description of the radially symmetric function contains modified Bessel functions and is highly complex. The same applies to the current distribution $\mathbf{j}(\mathbf{r})$, shown in figure 7.4 (a). It is also radially symmetrical. However, it initially increases with increasing distance from the vortex centre and then decreases again after reaching a maximum. The superconducting electron density is far away from the vortex centre $|\Psi|^2 = |\Psi_0|^2 = n_s$ and decreases to zero in the vortex core over a distance that is given by the coherence length ξ_{GL}. It is therefore also said that the normal core of the vortex has a diameter of $2\xi_{GL}$ [33].

A terminological clarification should now be made. Sometimes, instead of speaking of flux quantization the term **fluxoid quantization** is used. This can be explained by assuming a superconducting hollow loop, through which magnetic flux passes. It is not the magnetic flux from the external magnetic field that is quantized, but the fluxoid, which is the sum of both components:

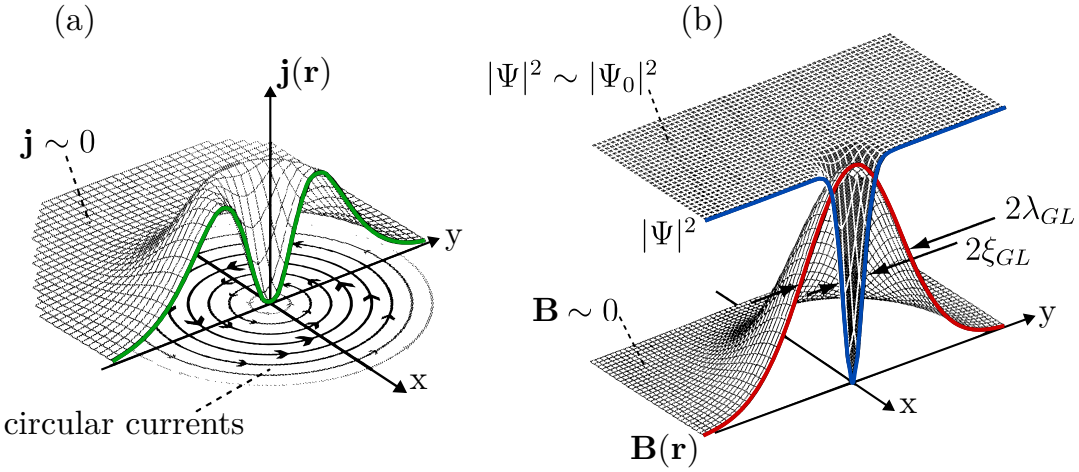

Fig. 7.4.: Structure of a single vortex. (a) The circular ring current density $\mathbf{j}(\mathbf{r})$ (green) is shown. It initially increases with radial distance from the vortex centre and then decreases. (b) The density of the superconducting electrons $|\Psi|^2$ (blue) drops to 0 in the centre of the vortex core. The magnetic field (red) is at its maximum in the centre of the vortex core and decreases with λ_{GL} (adapted from [33]).

the magnetic flux from the external field $\mathbf{B}$ and the magnetic flux generated by the superconducting ring current through the loop [43, 127]:

$$\underbrace{\oint_\gamma \frac{m^*}{n_s(2e)^2}\,\mathbf{j}\,\mathrm{d}\mathbf{r}}_{\text{flux from ring current}} + \underbrace{\int_F \mathbf{B}\cdot\hat{\boldsymbol{n}}\,\mathrm{d}F}_{\text{flux from external field}} = n\Phi_0. \tag{7.11}$$

Here, $\mathbf{j}$ represents the superconducting current density, γ is a closed curve surrounding the area F, and $\hat{\boldsymbol{n}}$ is the unit vector perpendicular to the area F. Regardless of the origin of the magnetic flux through the superconducting loop, it always corresponds to a multiple $n \in \mathbb{N}_0$ of the flux quantum Φ_0. This is why the term flux quantum is still appropriate and therefore used in this work.

7.2.2. Vortex interaction energy

In type-II superconductors, parallel vortices, i. e. vortices with the magnetic flux pointing in the same direction, repel each other due to electromagnetic interaction. The distance between vortex 1 and vortex 2 is denoted as r_{12}. The interaction energy $W_{12}(r_{12})$ per unit length of the vortex lines is then a complicated expression that includes the modified zero-order Bessel function [43]. However, $W_{12}(r_{12})$ can be reduced to two limiting forms.

For large distances $r_{12} \gg \lambda_L$ it holds that [33]

$$W_{12}(r_{12}) = \frac{\Phi_0^2}{2\pi\mu_0\lambda_L^2}\sqrt{\frac{\pi\lambda_L}{2r_{12}}}\exp\left(-\frac{r_{12}}{\lambda_L}\right). \tag{7.12}$$

The interaction energy therefore decreases exponentially with the distance of

the vortices. For small distances $\xi_{GL} < r_{12} \ll \lambda_L$ [33]

$$W_{12}(r_{12}) = \frac{\Phi_0^2}{2\pi\mu_0\lambda_L^2} \ln\left(\frac{\lambda_L}{r_{12}}\right) \tag{7.13}$$

is obtained. The interaction energy therefore increases with decreasing vortex distance.

In both cases, the interaction energy $W_{12}(r_{12})$ is positive for two parallel flux lines in a type-II superconductor. The superconductor can therefore minimise its energy by moving the vortices as far away from each other as possible, which results in **vortex-vortex repulsion**.

7.2.3. Abrikosov lattice

This repulsive force ensures that the vortices maintain a distance from each other. However, as the externally applied magnetic field B increases, the vortex density also increases and the average vortex spacing decreases [33].

If it is assumed that the positions of the vortices form a **square lattice** with the lattice constant $a_\square$ (see figure 7.5 (a)), then the area of the unit cell is $A_\square = a_\square^2$. This area accounts for exactly one flux quantum Φ_0. With $B = \frac{\Phi_0}{A_\square}$, the lattice constant $a_\square$ follows directly as a function of the magnetic field:

$$a_\square = \sqrt{\frac{\Phi_0}{B}}. \tag{7.14}$$

If we now consider a **triangular lattice** as in figure 7.5 (b), the area of the primitive grid cell, more precisely the Wigner-Seitz cell, can also be determined here with $A_\Delta = 1.5 a_\Delta^2 \tan(30°)$. Here too, with an applied magnetic field B, a flux quantum occupies exactly this area, i. e. $B = \frac{\Phi_0}{A_\Delta}$. This directly determines the lattice constant a_Δ of the triangular lattice as a function of the magnetic field:

$$a_\Delta \approx 1.075\sqrt{\frac{\Phi_0}{B}}. \tag{7.15}$$

A comparison now immediately shows that the distance between the flux lines for the same applied magnetic field is greater for the triangular lattice than for the quadratic lattice, namely

$$a_\Delta \approx 1.075 \cdot a_\square. \tag{7.16}$$

As the flux lines repel each other, as mentioned at the beginning, this greater distance is energetically more favourable. The energetic advantage of the triangular lattice over the quadratic lattice is approximately 1.7 % and is therefore

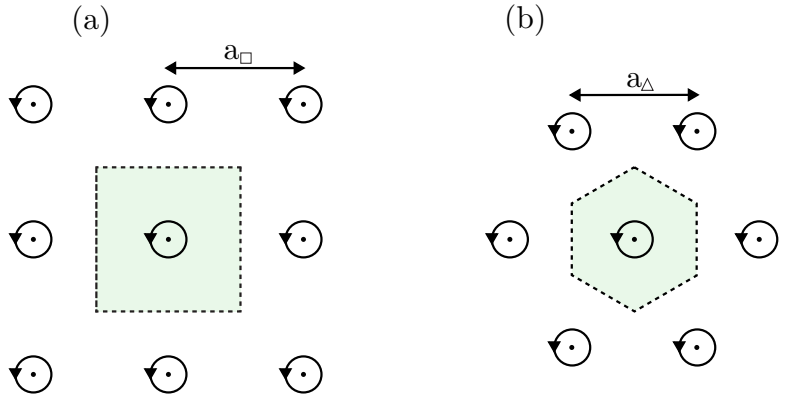

Fig. 7.5.: Quadratic and triangular flux lattice. (a) Quadratic flux line lattice with lattice constant $a_\square$. The Wigner-Seitz cell is shown in light green. (b) Triangular flux line lattice with lattice constant $a_\triangle$ and hexagonal Wigner-Seitz cell. This configuration is energetically more favourable compared to the square lattice, as there is a greater distance between the individual vortices for the same magnetic field B.

quite small [43].

The fact that vortex-vortex repulsion leads to this hexagonal lattice was recognised by Alexei Abrikosov. It is therefore also called the Abrikosov lattice after him. His solution approach is based on the relationship between induction and field strength and utilises the Ginzburg-Landau theory. It is mathematically far more complicated than the simple geometric approach shown here [9, 10].

Thus, in a type-II superconductor, a periodic arrangement of vortices is obtained between the lower and upper critical field. Most of the samples in this work have antidots with a square lattice. In the further course of this thesis it will be shown that the small energetic advantage of the hexagonal arrangement is not decisive here and that the vortices are forced into the square arrangement.

7.2.4. Current transport in the mixed state

The physical effect described in this section is essential for understanding the measurement data in chapter 8. If a current $\mathbf{j}$ smaller than the critical current density flows through a type-II superconductor, this initially occurs without losses. However, if the superconductor is in the mixed state due to an external homogeneous magnetic field $\mathbf{B}$, a force acts on the vortices[13]. This force is the **Lorentz force** $\mathbf{f}_L$, which is given per unit length of the flux line for a single superconducting flux quantum $\mathbf{\Phi}_0$ by [33]

$$\mathbf{f}_L = \mathbf{j} \times \mathbf{\Phi}_0. \tag{7.17}$$

[13]The vortex density is determined by $\mathbf{B}/\mathbf{\Phi}_0$.

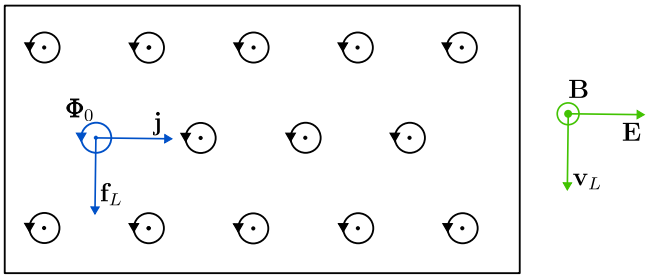

Fig. 7.6.: Vortex motion in mixed state. Shown is a lattice consisting of flux quanta $\mathbf{\Phi}_0$ in a type-II superconductor loop under the influence of the current $\mathbf{j}$. The Lorentz force $\mathbf{f}_L$ points perpendicular to the current and perpendicular to the direction of the flux lines (shown schematically for one flux quantum with blue vectors). As a result, the flux quanta move in the direction of $\mathbf{v}_L$. However, the total flux in the conductor loop remains constant, as the flux quanta exiting at the bottom are compensated for by flux quanta entering at the top. Due to the Faraday's law of induction, an electric field $\mathbf{E}$ builds up, which is perpendicular to the magnetic field $\mathbf{B}$ pointing out of the plane and perpendicular to $\mathbf{v}_L$ (drawn in green to the right of the conductor loop for the sake of clarity). This can be observed experimentally as a voltage drop.

The vortices therefore start to move perpendicular to the current and perpendicular to the magnetic flux $\mathbf{\Phi}$ in the sample geometry shown in figure 7.6 and dissipate energy in the process. The physics behind this dissipation will be explained in section 7.3 under the term 'flux flow' [134].

The Lorentz force naturally also acts on the circular currents. However, as these move in a circle around the flux quanta, the force effect is radial and cancels out.

As soon as they reach the end of the superconductor, the vortices leave it. According to the law of induction, a change in the magnetic flux over time leads to a voltage[14] $\mathcal{E}$ [43]:

$$\mathcal{E} = -\frac{\mathrm{d}}{\mathrm{d}t}\int_A \mathbf{B}\ \mathrm{d}\mathbf{A} \tag{7.18}$$

$$= \frac{1}{e}\oint_{\partial A}\left[e\mathbf{E} + e\mathbf{v}_L \times \mathbf{B}\right]\mathrm{d}\mathbf{l}. \tag{7.19}$$

Here, $\mathrm{d}\mathbf{l}$ is a path element of the conductor loop, A is the area of the conductor loop, $d\mathbf{A}$ is an oriented element of its surface, and ∂A is its edge. Additionally, Stokes' theorem was applied. However, vortices re-enter the superconductor at the opposite side of the sample geometry. The total flux in the system therefore remains constant over time. The integral in equation 7.19 must therefore become zero, which is why an electric field builds up:

$$\mathbf{E} = -\mathbf{v}_L \times \mathbf{B} = \mathbf{B} \times \mathbf{v}_L. \tag{7.20}$$

[14]The induced voltage here is an electromotive force. For this, the notation with the symbol $\mathcal{E}$ is usually used.

This electric field is perpendicular to the magnetic field (i. e. also perpendicular to the magnetic flux) and perpendicular to the direction of movement of the vortices, meaning that it is parallel to the transport current **j**. This results in a voltage drop that can be observed by measuring the electrical resistance [43, 127].

7.3. Vortex pinning

In order to achieve higher values for the critical current, the vortices can be prevented from moving. This process, which corresponds to an enlargement of the envelope in figure 7.1, can be achieved by so-called pinning. The Lorentz force $\mathbf{f}_L$ is then counteracted by a **pinning force** $\mathbf{f}_P$. It cannot be described with a general equation, as the pinning force depends on a number of parameters, such as the geometry of the pinning centre.

In principle, the vortices can pin to defects of all kinds. The sputtered Nb used in this work inevitably results in irregularities on the surface. Although these spatial variations only function weakly as pinning centres, they exist in large numbers. Another form of pinning centres are nano-engineered columnar defects, i. e. antidots. These are used specifically in this work to hold the vortices in place. They are very strong pinning centres, but only exist in small numbers compared to other material defects. Both irregularities in the Nb and antidots can be recognised on the SEM images in figure 4.4 [33].

Different regimes can be distinguished depending on the strength of the pinning when a current flows through the sample. If the **flux pinning** is very strong, the flux quanta are perfectly pinned, and there is no vortex propagation through the superconductor. As Tinkham [127] states, the superconductor behaves "very much like a perfect conductor".

Thermally activated flux quanta may jump from pinning centre to pinning centre as a result of a flux-density gradient. This is called **flux creep**. The flux-density gradient decays over time, and the flux creep decreases logarithmically. Experimental observation of flux creep is very demanding and any potentially occurring flux creep can be neglected in the experiments of this thesis[135].

In the absence of pinning or if the pinning is weak, the vortices move rather uniformly, the superconductor is in the **flux flow** regime. The superconductor has a finite resistivity resulting from the viscous drag of the vortices. The Bardeen-Stephen model [136] describes this phenomenon and assumes that the vortices have a normal conducting core with a radius of $\sim \xi_{GL}$, in which the complex order parameter Ψ disappears completely. The vortices are therefore normal conducting in the core, and dissipation occurs due to resistive processes, similar to the physics in a normal conductor [43, 127].

7.3.1. Saturation number and integer matching fields

There are numerous experimental and theoretical publications on the pinning of flux quanta in antidots. This includes both older research articles [137–144] and recent studies from the past few years [134, 145–151][15].

Depending on the size of the antidot, not only one but multiple flux quanta can be pinned. The **saturation number** n_{sat} represents the maximum number of flux quanta per antidot. In 1972 Mkrtchyan and Schmidt [152] estimated its value for a single cylindrical antidot of radius r_a:

$$n_{sat} \simeq \frac{r_a}{2\xi_{GL}(T)}. \tag{7.21}$$

In this work, however, not individual antidots are analysed, but a large number of them. These can be arranged in a grid and periodic pinning arrays are obtained. In 2000, Doria et al. [153] calculated the saturation number for such a regular arrangement of pinning centres and came to the conclusion that due to vortex-vortex interactions [154]:

$$n_{sat} \approx \Big(\frac{r_a}{\xi_{GL}(T)}\Big)^2. \tag{7.22}$$

Determining the best size of an antidot to pin the flux is difficult, but Moshchalkov et al. [155] comes to the general conclusion that pinning centres with a size greater than $\xi_{GL}(T)$ are more efficient than those with a size approximately equal to $\xi_{GL}(T)$.

In these periodic pinning arrays, there are various ways in which the vortices can be arranged. The simplest arrangement is known as the first matching field B_1. It occurs when the flux within the area A of the primitive unit cell corresponds to exactly one flux quantum, i. e.

$$B_1 = \frac{\Phi_0}{A}. \tag{7.23}$$

In this case, the number of flux quanta in the superconductor is equal to the number of antidots. If there is one or more flux quanta per primitive unit cell, than the corresponding magnetic field is referred to as an **integer matching field**:

$$B_n = n \cdot B_1, \tag{7.24}$$

with $n \in \mathbb{N}$.

[15] This selection of literature has played a role in the author's research, but it is not a complete list.

7.3.2. Flux periodic oscillations

As the pinned vortices no longer move through the superconductor when a current is applied, this reduces the flux motion and therefore also the dissipation. The antidots can thus reduce the resistivity of the sample. In experiments, this can be observed just below the transition temperature T_c, as this is when the flux quanta can be depinned more easily. If all (or most) of the vortices are trapped in the antidots, the resistance is zero (or low). However, if the vortices move, the superconductor enters the flux flow regime, resulting in an increase in resistance. As a result, flux **periodic oscillations of the resistance** as a function of the magnetic field can be observed [33].

The resistance oscillations are related to the **Little-Parks effect**, which was published by William Little and Ronald Parks in 1962 [156, 157]. However, the Little-Parks oscillations were measured in a single loop, specifically a superconducting hollow cylinder. They obtained flux periodic oscillations in the $T_c(B)$ phase boundary with a sharp maximum and a parabolic minimum (red curve in figure 7.7). In a superconducting network consisting of many loops, i. e. many antidots, the opposite will be observed. The maxima will be flat, and the minima will be cusp-shaped (blue curve in figure 7.7). The evolution of the $T_c(B)$ boundary gradually transforms from one to the other as the number of loops increases [33, 158].

Two lattice structures were analysed in this work: The main focus was on square lattices. Here, the flux quanta can no longer assume an Abrikosov lattice but are forced onto the square lattice structure. However, triangular lattices, which correspond to the Abrikosov lattice structure, were also investigated. The

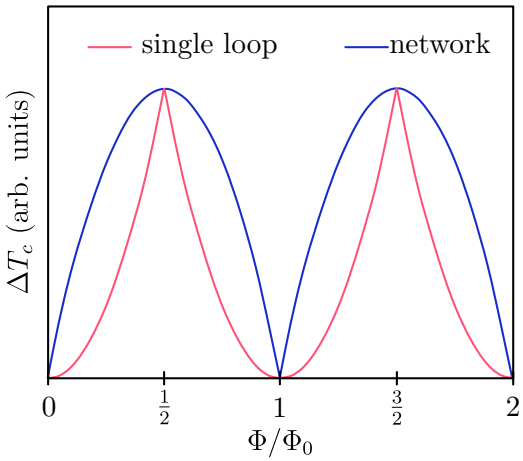

Fig. 7.7.: Schematic representation of the difference in the phase boundary ΔT_c as a function of Φ/Φ_0 when the number of superconducting loops is changed from one to a large number. The curve for a single loop (red) is reminiscent of Little and Parks' observations, the other curve (blue) is for a superconducting network. The shape of the oscillations is similar to the resistance oscillations in chapter 8 (adapted from [33]).

number of antidots ranged from 10 000 to several 100 000, depending on the lattice period. Occasionally, samples with 2 000 000 antidots were also studied.

7.3.3. Hofstadter butterfly and fractional matching fields

The matching fields can be not only integer but also fractional in nature. Whenever there is commensurability between the periodicity of the flux quantum lattice and the periodicity of the antidot pinning array, these matching fields can occur. The **fractional matching fields** are defined as [33]

$$B_{p/q} = \frac{p}{q} \cdot B_1, \tag{7.25}$$

with $p, q \in \mathbb{N}$. At the fractional matching fields, the flux quanta can be in particularly stable lattice configurations, which reduces the flux motion and results in dips in the resistance at the corresponding fractions.

Fascinatingly, the fractional matching fields are related to the Hofstadter butterfly graph, which was described by Douglas Hofstadter in 1976 and named

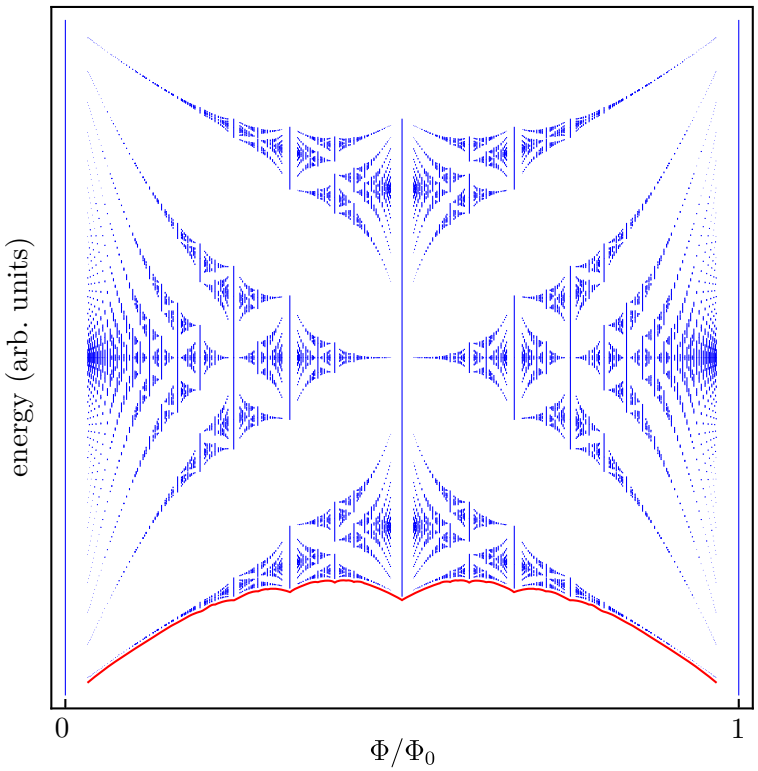

Fig. 7.8.: Simulation of a Hofstadter butterfly. Shown is the energy spectrum (blue) for Bloch electrons in a square 2D lattice potential with a homogeneous magnetic field. The large gaps in the graph resemble a butterfly, hence the name. The lower edge of the spectrum (indicated in red) corresponds to the $T_c(B)$ phase boundary of a square superconducting network with fractional matching fields. The energy spectrum was originally calculated by Hofstadter [13] (adapted from [159]).

after him [13]. Figure 7.8 shows such a graph, which illustrates the fractal energy spectrum of a 2D electron system with a periodic potential in a perpendicular magnetic field [160]. The fractional matching fields are connected to the Hofstadter butterfly since the $T_c(B)$ phase boundary is equal to the **lowest edge of the spectrum**. This was shown by shown by Pannetier et al. [12], who investigated a superconducting network made of aluminium. He obtained a fractal fine structure of $T_c(B)$ with dips at $\Phi/\Phi_0 = \frac{1}{3}, \frac{2}{5}, \frac{1}{2}, \frac{3}{5}, \frac{2}{3}$ and very faintly at $\frac{1}{4}$ and $\frac{3}{4}$.

It is important to note that in this thesis, the resistivity was measured rather than the critical temperature phase boundary. The main objective of this thesis was not to observe a Hofstadter butterfly, but rather to evaluate the effectiveness of flux pinning. Therefore, the fractional features in chapter 8 do not precisely represent the lower edge spectrum of the Hofstadter butterfly. Nonetheless, the dips in resistance at fractional values reflect the commensurability of the antidot lattice period with the vortex lattice.

7.3.4. Vortex arrangement

Another interesting question is whether the flux quanta are located in the antidots or pinned to material defects in the Nb. The exact position of the flux quanta can be determined using Lorentz microscopy [161]. In the experiments in this doctoral thesis, however, it is a priori not clear where exactly the flux quanta are located. Nevertheless, assumptions can be made based on the matching fields, the lattice structure, the antidot diameter, the saturation number and the temperature. Therefore, a few terms should be clarified here.

If there are several flux quanta in an antidot, these are called **multiquanta vortices**. This phenomenon is more likely to occur when the diameter of the antidots is large, i. e. if the number of vortices per primitive unit cell n is smaller than the saturation number n_{sat} [155, 162].

If the vortices are located in places between the antidots, they are called **interstitial vortices**. Examples for this can be seen in figure 7.9. This occurs for instance when the surrounding antidots are occupied by vortices and $n > n_{sat}$. They are said to be caged or quasi-bound due to the repelling nature of the vortices [138, 163, 164]. However, these interstitials are not as effectively pinned as the vortices in the antidots and already a weak Lorentz force $\mathbf{f}_L$ is enough to depin them.

The exact position of the vortices also depends on the temperature: Since the Ginzburg-Landau coherence length ξ_{GL} diverges with increasing temperature (see equation 7.3), the saturation number n_{sat} becomes smaller. Close to T_c, the vortices no longer fit into the antidots and become interstitial vortices [33].

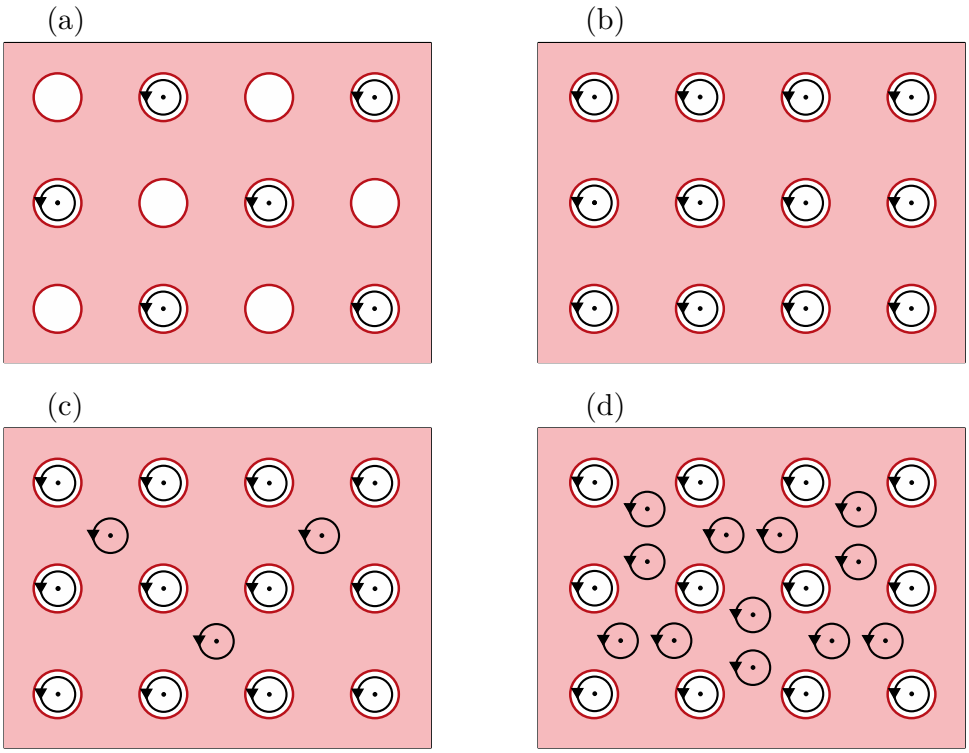

Fig. 7.9.: Schematic of the possible vortex configurations in a square antidot lattice. The configurations depicted were observed by Harada et al. [161] using Lorentz micrographs. In configuration (a), every second antidot in the superconductor (red) is occupied by a vortex (black). This lattice configuration is known as a checkerboard pattern, its corresponding matching field is $B_{1/2}$. (b) Matching field B_1: Each antidot hosts exactly one vortex, resulting in a highly stable configuration. (c) Matching field $B_{3/2}$: In the case of small antidots, interstitial Abrikosov vortices may occur between them. Here, there is one interstitial vortex for every two antidots. (d) Matching field B_3: The vortex-vortex repulsion allows for the formation of complicated patterns. Possible multiquanta vortex configurations are not shown here.

8. Pinning effects in antidots

The motivation for the experiments described in this chapter was to ensure that the flux quanta were inside the antidots. This would allow for the detection of Majorana bound states by capacitance measurements.

Several interesting effects related to the pinning properties of the antidots were observed. This chapter starts with a characterisation of the sputtered Nb, followed by pinning experiments showing the observation of integer matching fields. Subsequently, the dependence of the pinning properties on the current amplitude is analysed. In the last section, measurements showing fractional matching fields are presented and an attempt is made to assign the Hofstadter butterfly fractions to the observed features. The samples were fabricated on wafer number 150213, which is shown in figure 4.1 (b). A brief characterization of the wafer is provided in appendix B.2.

To investigate the effect of HgTe on the pinning characteristics, Nb antidots were fabricated on the trivial insulator SiO_2 for comparison. The fabrication procedures were kept as similar as possible to those on HgTe[16]. The Nb-SiO_2 samples were prepared by Benedikt Kopyciok and the data were obtained in collaboration with him. The thickness of Nb is between 30 nm and 40 nm for all samples and the magnetic field is always applied perpendicular to the sample geometry.

8.1. Niobium characterization

By measuring the longitudinal resistivity ρ_{xx} as a function of the magnetic field B at low temperatures, one can directly observe the breakdown of superconductivity at the upper critical field B_{c2}. By repeating this measurement at several fixed temperatures T, it is possible to determine the critical temperature at zero magnetic field T_c and the temperature dependent Ginzburg-Landau coherence length $\xi_{GL}(T)$. The latter parameter is particularly useful as it enables comparison of experimental results with the existing theory in later sections of this chapter.

As the measurement data from the Nb-HgTe samples revealed a number

[16]It should be noted that for HgTe the CdTe cap layer was removed by Ar^+-etching, which was not necessary for the SiO_2 wafer.

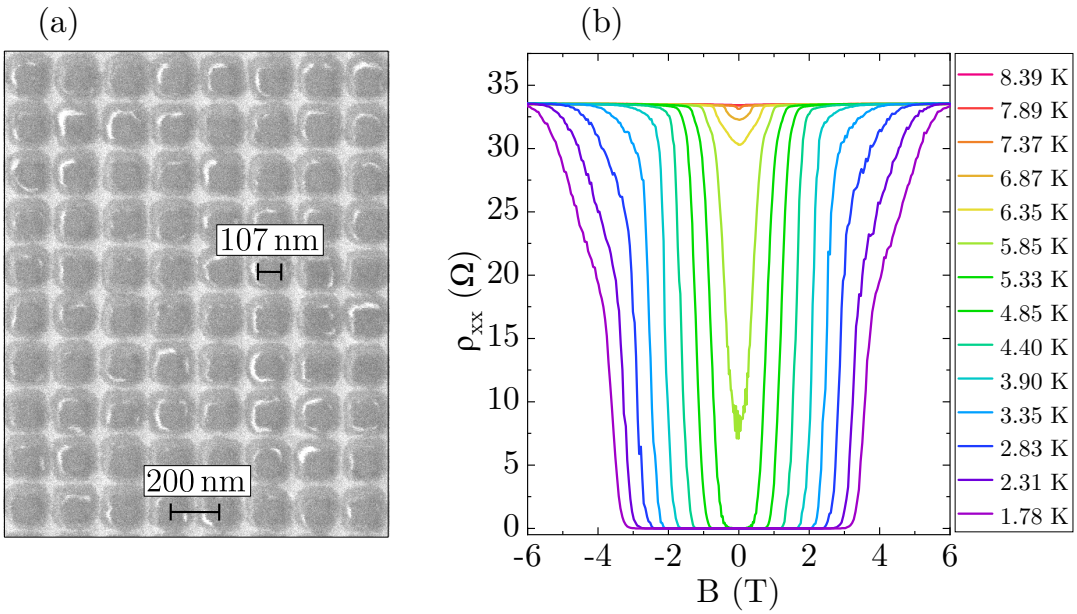

Fig. 8.1.: SEM image of Nb antidots on SiO_2 and ρ_{xx} vs B. (a) The antidots have a periodicity of $a_\square = 200\,\text{nm}$ and a rather squared shape. The average of several measurements yields a horizontal and vertical diameter of $d_a = 107\,\text{nm}$. (b) The resistivity ρ_{xx} vs magnetic field B is shown for different temperatures T. From the data, B_{c2} can be determined as a function of T. The measurement was obtained using the AC lock-in technique at a current of 100 nA at 43 Hz.

of atypical characteristics, a comparison was made with data from Nb-SiO_2 samples. The two samples compared in this section have very similar Nb antidot geometries. The similarities and differences have also been observed in samples with other antidot periodicities and diameters, as well as samples with unpatterned Nb. Therefore, the effects described in this section are not caused by the geometry of the antidots, but rather by the quality of the sputtered Nb and by the underlying insulator.

First, the measurement data of an Nb-SiO_2 sample with $a_\square = 200\,\text{nm}$ periodic antidots is shown. The antidots form a square lattice and also tend to be square rather than round in shape, as can be seen in figure 8.1 (a). Figure 8.1 (b) shows the corresponding measurement of ρ_{xx} vs B. The resistivity is zero at low magnetic fields and temperatures. Both of these two parameters contribute to the breakdown of superconductivity. The resistivity at the normal conducting state, ρ^n_{xx}, is constant at $\rho^n_{xx} = 33\,\Omega$. Figure 8.2 (a) shows an SEM image of Nb antidots on HgTe. These are also 200 nm periodic and have a very similar shape to the antidots on SiO_2. Figure 8.2 (b) shows the corresponding measured data, which differ in several aspects from the data of the Nb-SiO_2 sample.

The first notable observation is that the absolute value of the normal resistivity ρ^n_{xx} differs by an order of magnitude between the two samples. All

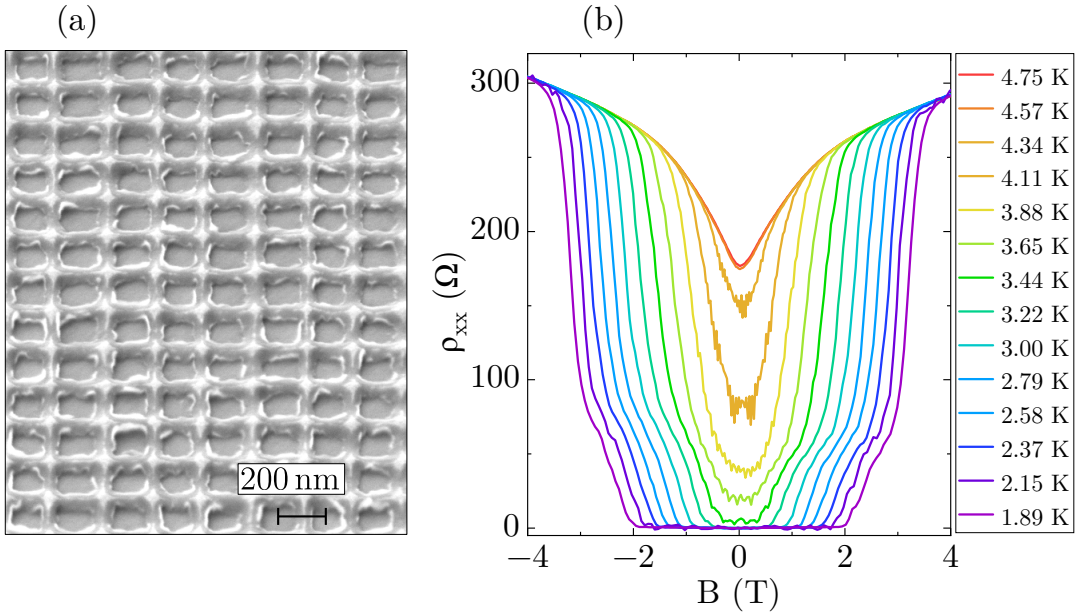

Fig. 8.2.: Tilted SEM image of Nb antidots on HgTe and ρ_{xx} vs B. (a) The antidots are very similar to those on SiO_2 as they have a periodicity of 200 nm, a square shape and an average diameter of $d_a = 106$ nm. (b) ρ_{xx} vs B exhibits several features that were not observed in the sample on SiO_2. These are described in the main text. The measurement was obtained using the AC lock-in technique at a current of 100 nA at 53 Hz.

samples have shown a **large fluctuation** in ρ^n_{xx}. This is presumably due to the varying quality of the sputtered Nb. The samples were fabricated over a period of several years, and the quality of the Nb can vary significantly depending on the sputtering process parameters and the regular replacement of the Nb target [165]. Additionally, the exact thickness of the Nb is unknown, and it has been demonstrated that for thin Nb films, the sheet resistance is highly dependent on the film thickness [166].

The second aspect is that ρ^n_{xx} is **not constant**, which may be due to the additional contribution to conductivity from the HgTe. Equations 3.5 and 3.6 demonstrate that all four conductivity components, i. e. the transversal and the longitudinal components of both Nb and HgTe, contribute to the signal. For instance, this includes the transversal conductivity σ_{xy} of HgTe which can appear due to the QHE. Explaining the qualitative shape of the curve of ρ_{xx} is difficult as the contribution of the individual components is not known.

The third feature can be seen in figure 8.2 (b), between $2-3$ T and $0-100\,\Omega$, in the curve which was obtained at 1.89 K. The resistivity increases gradually with increasing field until it reaches a kink, after which it increases more rapidly. These **shoulder-like features** are only present in the samples on the HgTe topological insulator, and their origin remains unclear. The first feature described, i. e. the fluctuation of the absolute value of ρ^n_{xx}, appeared in both

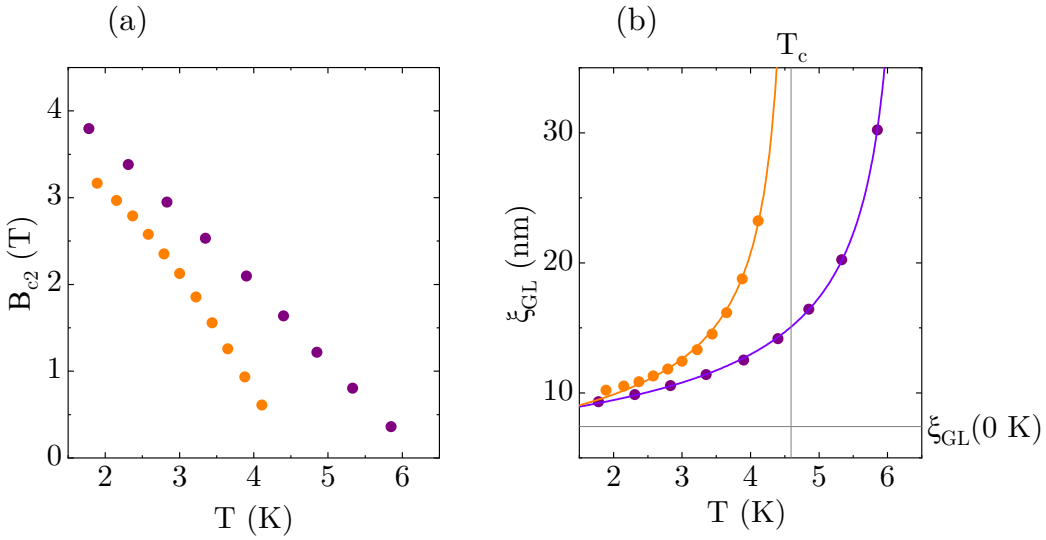

Fig. 8.3.: Comparison of upper critical field B_{c2} and Ginzburg-Landau coherence length ξ_{GL} vs temperature T for Nb-HgTe and Nb-SiO_2. (a) B_{c2} increases as T decreases, with Nb-SiO_2 (purple) exhibiting a larger B_{c2} than Nb-HgTe (orange). (b) The data for ξ_{GL} can be fitted and extrapolated with equation 7.3 to extract T_c and $\xi_{GL}(0\,\mathrm{K})$. The extraction of the two parameters is indicated for the Nb-HgTe sample data. ξ_{GL} has shown a similar value for all measured samples, while T_c varied significantly. This is presumably due to quality and thickness of the sputtered Nb [165, 166].

Nb-SiO_2 and Nb-HgTe samples. The second and the third feature occurred only in Nb-HgTe samples, but for both samples with antidots and samples with unpatterned Nb.

The temperature-dependent upper critical field $B_{c2}(T)$ is reflected by the magnetic field at which the sample becomes normal conducting. It is conventional to determine $B_{c2}(T)$ at half of ρ^n_{xx}. Figure 8.3 (a) shows $B_{c2}(T)$ for Nb-HgTe (orange) and Nb-SiO_2 (purple). $B_{c2}(T)$ increases linearly with decreasing temperature for both samples. This is in agreement with equations 7.3 and 7.9 from the Ginzburg-Landau theory. Additionally, the latter equation can be used to determine the temperature-dependent coherence length $\xi_{GL}(T)$ from $B_{c2}(T)$. The corresponding data are shown in figure 8.3 (b). The data points can be fitted with the temperature dependence of $\xi_{GL}(T)$, which is known from equation 7.3. The intersection point from the extrapolation of the fit with the y-axis at $T = 0\,\mathrm{K}$ allows for the determination of $\xi_{GL}(0\,\mathrm{K})$. As $\xi_{GL}(T)$ diverges at T_c, the value of T_c can be determined from the vertical asymptote on the diverging curve.

The results reveal another difference between the two samples: T_c is higher for the Nb-SiO_2 sample. The fit showed that $T_c = 6.27\,\mathrm{K}$ for Nb-SiO_2 and $T_c = 4.59\,\mathrm{K}$ for Nb-HgTe. However, T_c varied across all samples, regardless of the underlying insulator, ranging from $3.9 - 7.5\,\mathrm{K}$. This is presumably also due to the different quality of the sputtered Nb. It has been shown that T_c

depends on number of parameters, such as residual gases in the evaporator and evaporation rate [165]. Furthermore, T_c is dependent on film thickness for thin Nb films [166].

The measured samples consistently showed a coherence length $\xi_{GL}(0\,\mathrm{K})$ within the range of $6.3 - 8.9\,\mathrm{nm}$, indicating a high reproducibility. For the Nb-SiO_2 sample shown here $\xi_{GL}(0\,\mathrm{K}) = 7.79\,\mathrm{nm}$, and for Nb-HgTe sample shown $\xi_{GL}(0\,\mathrm{K}) = 7.41\,\mathrm{nm}$.

8.2. Integer pinning effects

This section presents the pinning experiments on the Nb antidots, focusing on the data where oscillations in ρ_{xx} were observed as a function of magnetic field corresponding to integer matching fields. The theory behind this is described in detail in chapter 7. The results discussed here have all been obtained in Nb-HgTe heterostructures.

8.2.1. Integer matching fields

Firstly, pinning effects obtained on the Nb-HgTe sample with $a_\square = 200\,\mathrm{nm}$ periodic antidots characterised in section 8.1 are studied. Figure 8.4 displays the resistivity ρ_{xx} as a function of the magnetic field B. Unlike the previous measurements, this plot focuses only on the regime just below the transition temperature T_c at low magnetic fields. Oscillations with a periodicity of approximately $52\,\mathrm{mT}$ can be clearly seen. This agrees with the first matching field B_1 that can be calculated from the geometric antidot periodicity:

$$B_1 = \frac{\Phi_0}{a_\square^2} \approx 51.68\,\mathrm{mT}. \tag{8.1}$$

The measurement displays dips in the resistivity at multiple integer matching fields $B_n = n \cdot B_1$ with $n \in \mathbb{N}$, specifically at $\pm B_2$ and, due to the limited magnetic field interval only partially visible, at $\pm B_3$. These observations were made over a wide temperature range below $T_c = 4.59\,\mathrm{K}$. Specifically, the oscillations were observed from $T = 4.45\,\mathrm{K}$ to $T = 3.43\,\mathrm{K}$. These measurements reflect a **pronounced pinning** behaviour of the vortices, which can be observed down to a reduced temperature of

$$\frac{T}{T_c} = 0.75. \tag{8.2}$$

The available literature suggests that this tends to be the lower limit at which pinning can be observed by resistivity measurements[148, 167–169]. A comparison with the pinning properties of the Nb-SiO_2 samples is made in section 8.3.

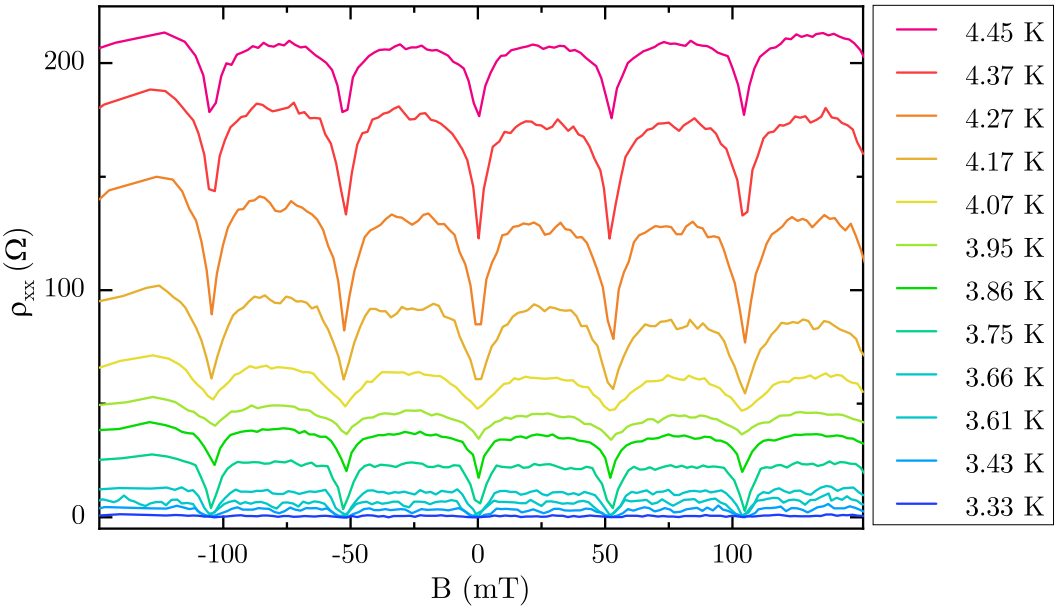

Fig. 8.4.: Integer matching fields at different temperatures. Shown is ρ_{xx} vs B in the range of small magnetic fields below $T_c = 4.59\,\mathrm{K}$. The oscillations' periodicity corresponds well to $B_1 = 51.68\,\mathrm{mT}$, which can be calculated from the antidot periodicity. The pinning of the vortices is evident over a wide temperature range. The measurements were conducted on the 200 nm periodic Nb-HgTe sample from section 8.1 using the AC lock-in technique at 300 nA and 53 Hz.

8.2.2. Flux quanta saturation

Now, data are analysed in which the magnetic field interval is wide enough to count the number of visible oscillations, allowing a comparison with the saturation number n_{sat}. Figure 8.5 (a) shows an SEM image of antidots with a periodicity of 400 nm and a square shape with a diameter of $d_a = 244\,\mathrm{nm}$. The corresponding $\xi_{GL}(T)$ data are presented in figure 8.5 (b).

This sample also exhibits oscillations in resistivity with respect to the magnetic field, as shown in figure 8.6. A clear pinning behaviour is evident up to matching field $\pm B_{20}$, very weakly even up to approximately $\pm B_{27}$. The experimentally observed periodicity $B_1 = 13.1\,\mathrm{mT}$ agrees very well with $B_1 = \Phi_0/\mathrm{a}_\square^2 \approx 12.92\,\mathrm{mT}$. Equation 7.22 gives the theoretical **maximum number of flux quanta** per antidot, represented by the saturation number n_{sat}. For the average antidot radius $r_a \approx 122\,\mathrm{nm}$ and $\xi_{GL}(4.8\,\mathrm{K}) = 29.4\,\mathrm{nm}$ one obtains [153, 154]

$$n_{sat} \approx \left(\frac{r_a}{\xi_{GL}(4.8\,\mathrm{K})}\right)^2 \approx 17. \tag{8.3}$$

Therefore, according to theory up to 17 vortices can fit into one antidot. However, this does not necessarily mean that only 17 oscillations will be observed. As explained in section 7.3.4, interstitial pinning becomes likely at large matching

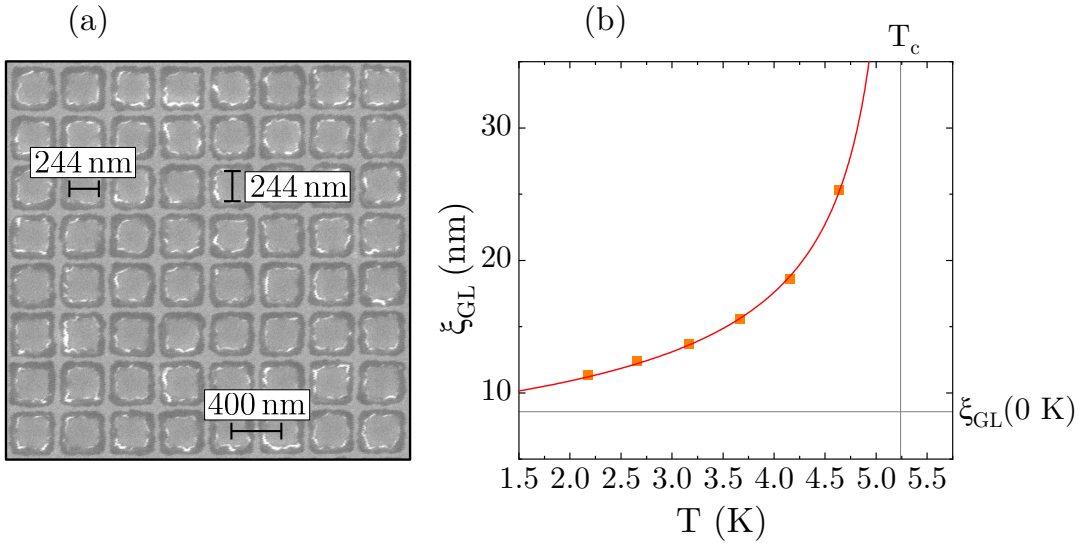

Fig. 8.5.: SEM image of 400 nm periodic antidots and ξ_{GL} vs T. (a) The top view SEM image displays square antidots on HgTe with a periodicity of $a_{\square} = 400\,\text{nm}$. The horizontal and vertical average diameter is $d_a = 244\,\text{nm}$. The edges of the Nb appear slightly darker in this image. (b) The coherence length vs temperature data points are fitted with equation 7.3, yielding $\xi_{GL}(0\,\text{K}) = 8.57\,\text{nm}$ and $T_c = 5.24\,\text{K}$.

fields. In addition to the vortices pinned inside the antidots, these interstitial vortices can be caged between the antidots due to vortex-vortex repulsion. As long as the pinning configurations remain stable, the resistivity decreases at the corresponding matching fields. This could cause oscillations above the matching field given by n_{sat}. The data show that the resistivity minima at the matching fields become less pronounced with increasing magnetic field. This may indicate weaker pinning of the interstitial vortices as these are not as effectively pinned as the vortices in the antidots [169].

Moreover, two possible inaccuracies in the determination of n_{sat} should be noted. Firstly, ξ_{GL} diverges at T_c. Therefore, a small difference in T near T_c can lead to a potentially large difference in $1/\xi_{GL}^2$, which will significantly affect the calculated value of n_{sat}. Secondly, the formula for n_{sat} was derived for antidots with a circular shape [153, 154]. However, the antidots analysed here have a square shape, which increases the antidot area by a total of 27 %[17]. This allows the conclusion that with this antidot geometry, more flux quanta can fit into one antidot.

Most samples with antidots showed integer pinning effects. In particular, antidots with a small periodicity of $200 - 400\,\text{nm}$ but a relatively large diameter of around $100 - 300\,\text{nm}$ showed pronounced pinning behaviour. This mainly concerns the antidots fabricated with CSAR and PMMA resists (see section 4.3).

[17] A square with the same diameter as a circle has an area that is 27 % larger than the area of the circle.

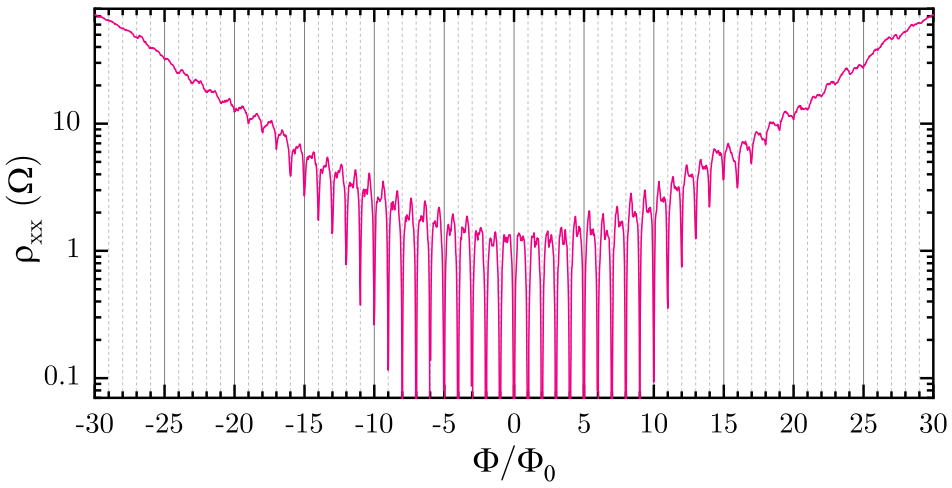

Fig. 8.6.: ρ_{xx} on a logarithmic scale as a function of the reduced magnetic flux Φ/Φ_0. Shown is a measurement of the sample with the 400 nm periodic antidots on HgTe of figure 8.5, revealing oscillations up to matching field $\pm B_{20}$, very weakly even up to approximately $\pm B_{27}$. Fractional features at $B_{1/2}$ were also observed, but are not discussed in this section. The curve was recorded at 4.8 K, corresponding to $T/T_c = 0.92$. The data were obtained using the AC lock-in technique at 100 nA and 53 Hz.

Antidots fabricated with negative resist had larger periods of 800 nm and smaller diameters of around $40 - 70$ nm. No flux pinning effects were observed in any of the samples fabricated with negative resist. There could be several reasons for this. Firstly, it is possible that $n_{sat} < 1$, due to the small antidot radius. This is the case when the antidot radius $r_a < \xi_{GL}(T)$. Pinning should theoretically still be possible as $\xi_{GL}(T)$ decreases with decreasing temperature, but only at low temperatures. At these temperatures the pinning effects may not be observed as the resistance of the sample drops to zero. However, it is worth noting that this argument may not always be applicable. For example, in the sample shown in appendix B.3, the antidot radius is $r_a \approx 30$ nm. The coherence length at 4 K, i. e. just below $T_c = 4.36$ K, is $\xi_{GL}(4\,\mathrm{K}) = 22$ nm. This suggests that one flux quantum should fit into each antidot, since the calculated value for $n_{sat} = 1.86$ is above 1. However, no pinning effects were observed during the experiment.

Alternatively, it is possible that the vortex-vortex repulsion described in section 7.2.2 is too weak due to the large distance between the vortices. The vortex configuration no longer adapts to the configuration of the square antidot lattice. As a result, the vortices become pinned to the defects of the sputtered Nb, resulting in interstitial vortices in a disordered and unstable configuration. Consequently, they can be depinned very easily, and no oscillations can be observed.

8.2.3. Depinning by current

The pinning behaviour can also be studied as a function of a DC current passing through the sample. This is achieved using the differential resistance measurement setup described in section 5.3.2. The resistivity ρ_{xx} calculated from the AC voltage and AC current can then be plotted as a function of DC current I and magnetic field B in a 2D colour map. The data displayed in this way has a visual resemblance to a pine tree. During the course of this work it was discovered that this type of measurement can reveal pinning behaviour that is not apparent in the line plots obtained with the AC lock-in technique.

The sample shown in figure 8.7 (a) features 300 nm periodic antidots. The antidots have an irregular shape with an average diameter of $d_a = 132\,\text{nm}$. Figure 8.7 (b) displays the corresponding $\xi_{GL}(T)$ data.

The theoretical first matching field is given by $B_1 = \Phi_0/a_\square^2 \approx 22.96\,\text{mT}$. The measured data shown in figure 8.8 are consistent with this value. These data were obtained using the AC lock-in technique. The lowest temperature at which oscillations can be clearly observed is $T = 4.44\,\text{K}$, which corresponds to $T/T_c \approx 0.95$.

Figure 8.9, on the other hand, shows ρ_{xx} obtained with the differential resistance setup as a function of DC current I and the reduced magnetic flux Φ/Φ_0. At low currents and magnetic fields, ρ_{xx} is low and the sample is superconducting (black). However, with increasing DC current and magnetic field, the sample tends to have finite resistivity (green). The integer matching

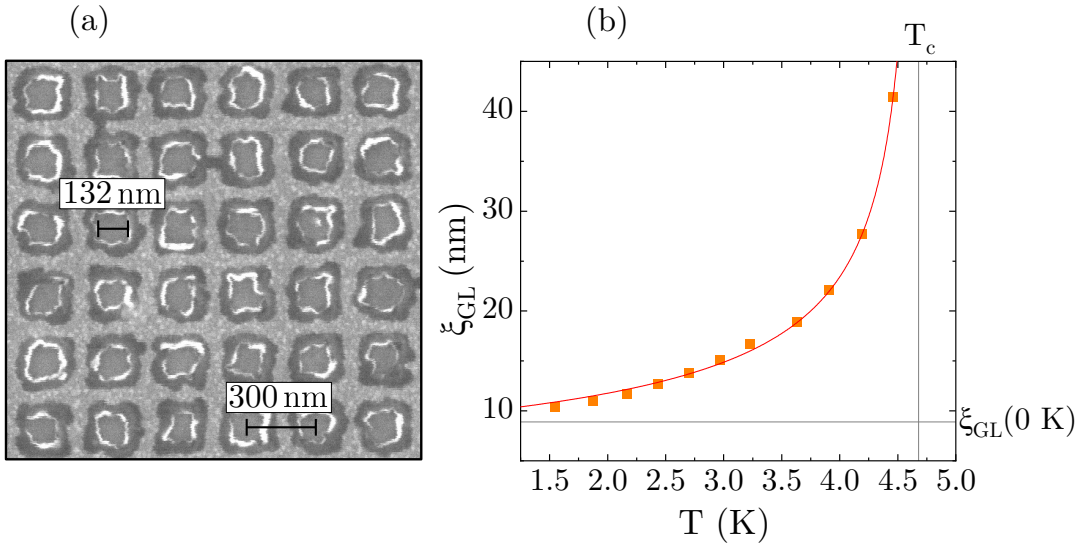

Fig. 8.7.: SEM image of 300 nm periodic antidots and ξ_{GL} vs T. (a) The top view SEM picture reveals irregularly shaped antidots on HgTe with a periodicity of $a = 300\,\text{nm}$ and an average diameter of $d_a = 132\,\text{nm}$. (b) The coherence length vs temperature is shown. The fit converges and yields $\xi_{GL}(0\,\text{K}) = 8.90\,\text{nm}$ and $T_c = 4.68\,\text{K}$.

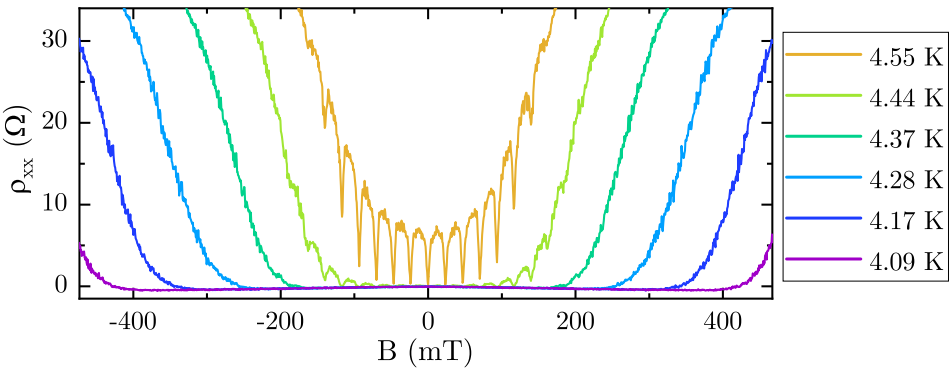

Fig. 8.8.: ρ_{xx} vs B below $T_c = 4.68\,\mathrm{K}$. The oscillations at 4.55 K and 4.44 K are clearly visible. The periodicity of the oscillations corresponds to the expected integer matching fields. At lower temperatures, the sample transitions directly from the superconducting state to the normal conducting state without any noticeable oscillations. The data were obtained using the AC lock-in technique at 150 nA and 13 Hz.

fields are an exception to this. At these fields, the sample exhibits a low ρ_{xx} even at DC currents up to $I = 30\,\mu\mathrm{A}$, and black horizontal lines become visible.

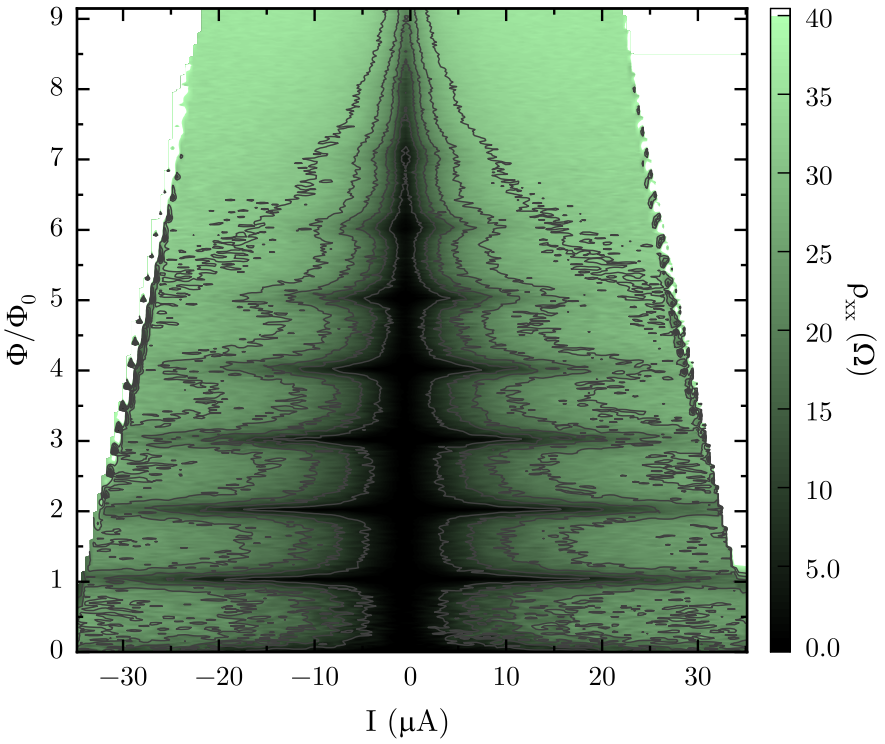

Fig. 8.9.: 2D colour map of ρ_{xx} as a function of DC current I and the reduced magnetic flux Φ/Φ_0 at 4.44 K. The colour black indicates low resistivity or superconductivity, whereas green indicates finite resistivity. The black area resembles a pine tree with 6 branches. One drawback of this measurement method is that the curves become increasingly noisy towards higher DC currents. This is reflected by the black contour lines, which are spaced at 5 Ω intervals. The measurement was taken at 13 Hz with the differential resistance setup.

The data representation resembles a pine tree, hence the name. The value of the pre-resistor was not large enough to ensure a constant current, which causes the roof shape of the visible data points. The rippled edges are an artefact of data processing. The measurement was taken at 4.44 K, which is the same temperature at which the light green curve in figure 8.8 was obtained.

Figure 8.10 shows another 2D colour plot. These data were recorded at 4.17 K, i. e. $T/T_c = 0.89$, corresponding to the dark blue curve in figure 8.8. The colour plot shows a pine tree with pronounced 'branches', reflecting stable pinning. This is in contrast to the line plot where the resistivity increases from zero to a finite resistivity with no discernible oscillations. The differential resistance measurements therefore allow for the detection of pinning effects at low temperatures due to large DC currents.

The **depinning currents** in the second pine tree plot reach up to 120 µA, which is approximately four times higher than the depinning currents of the first pine tree plot. This indicates that vortex pinning is stronger at lower temperatures. The resistivity obtained depends on the current, magnetic field, and temperature. This is similar to the schematic 3D phase diagram shown in figure 7.1, where the superconducting state also depends on these parameters.

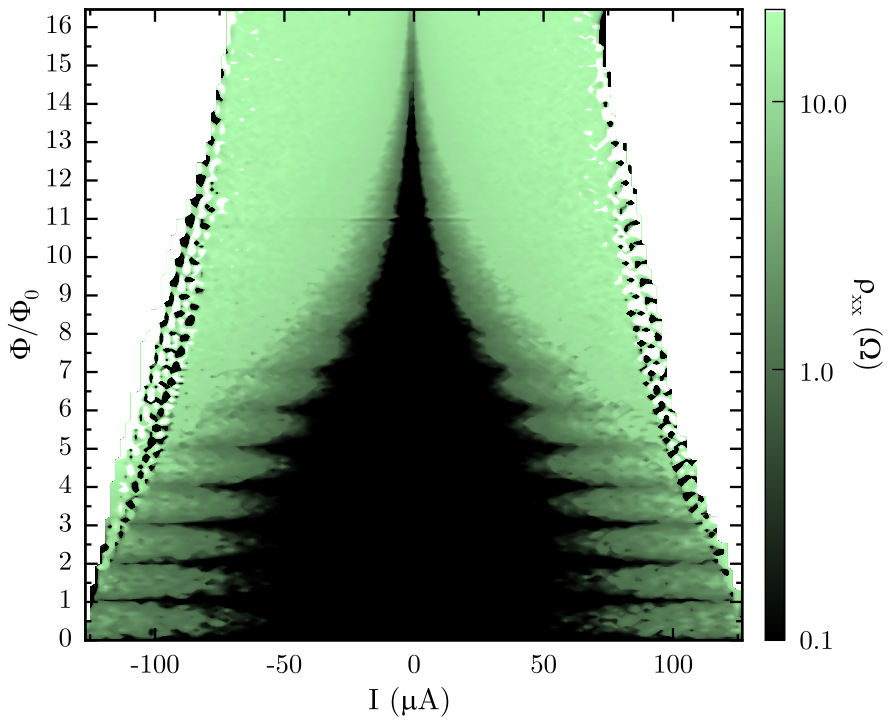

Fig. 8.10.: 2D colour map of ρ_{xx} as a function of I and Φ/Φ_0 at 4.17 K. ρ_{xx} is shown on a logarithmic scale to increase the visibility of the features. The data resemble a pine tree with a total of 8 branches. This measurement allows for the observation of pinning effects, which were not discernible at the same temperature in figure 8.8. No contour lines are shown in this figure for clarity. The measurement was taken at 13 Hz with the differential resistance setup.

By using the known radius $r_a \approx 66\,\mathrm{nm}$ and values for $\xi_{GL}(T)$, n_{sat} can be calculated. The coherence length for the first pine tree figure is $\xi_{GL}(4.44\,\mathrm{K}) = 39.5\,\mathrm{nm}$. The result for the calculated saturation number is $n_{sat} \approx 2.8$. The coherence length for the second pine tree figure is $\xi_{GL}(4.17\,\mathrm{K}) = 27\,\mathrm{nm}$, which yields $n_{sat} \approx 6$. In both cases, n_{sat} is lower than the number of countable branches in the pine tree colour plots. Possible reasons for this are described in section 8.2.2. These include interstitial pinning, the irregular antidot shape or the exact value of $\xi_{GL}(T)$, which is strongly dependent on the temperature.

The differential resistance measurements enable the observation of flux pinning that may not be visible in the line curves obtained with the AC lock-in technique. They also demonstrate that the flux remains pinned for currents of up to several µA. This implies that the vortices will not be depinned by the AC currents that flow through the sample during capacitance measurements, as these currents are typically of the order of nA or less. It should be noted that no fractional matching fields were observed in the differential resistance measurements.

8.3. Fractional pinning effects

During the measurements of the antidot samples, in addition to the resistivity dips corresponding to the integer matching fields, distinct fine structures were occasionally observed. These structures were identified as fractional matching fields $B_{p/q}$ and are discussed in this section.

8.3.1. Checkerboard pattern

The most pronounced fractional matching fields observed were at

$$\pm B_{n+1/2} \quad \text{with} \quad n \in \mathbb{N}_0. \tag{8.4}$$

An example of such a measurement is shown in figure 8.11. The features were observed in the $a_\square = 400\,\mathrm{nm}$ periodic Nb antidots on HgTe which are shown in figure 8.5 (a). The specific case of $\pm B_{1/2}$ is also called a checkerboard configuration. Here, every second antidot is occupied by a vortex, as shown in figure 7.9 (a). The configuration resembles a checkerboard pattern, hence the name. This vortex configuration is usually **very stable** [33, 42, 143]. The Hofstadter butterfly graph shown in figure 7.8 reveals a pronounced dip at the lower edge of the spectrum at $\Phi/\Phi_0 = 1/2$, consistent with the obtained data.

The first integer matching field is represented by $\pm B_1$, corresponding to the configuration shown in 7.9 (b). Additionally, there are fractional dips at 1/2 towards higher integer matching fields, such as $\pm B_{3/2}$. There, the

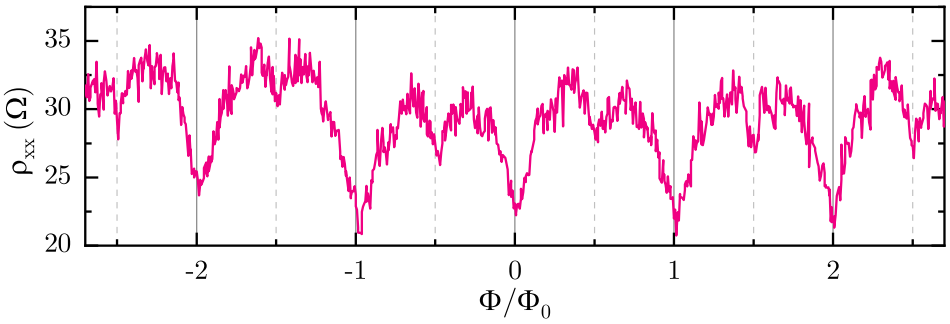

Fig. 8.11.: Fractional matching fields at $\pm B_{n+1/2}$ with $n \in \mathbb{N}_0$ in a Nb-HgTe sample. The antidot periodicity $a_\square = 400\,\text{nm}$ corresponds to $B_1 = \Phi_0/a_\square^2 \approx 12.92\,\text{mT}$. The data were obtained with the AC lock-in technique at 4.9 K, 43 Hz, and 300 nA.

vortex configuration is unknown, but one possibility is that each antidot is singly occupied and half of all vortices are interstitials between the antidots, as shown in figure 7.9 (c). However, it is more probable that **multiquanta vortices** are present and every second antidot is doubly occupied [144]. This is supported by the average antidot radius $r_a \approx 122\,\text{nm}$ and the coherence length $\xi_{GL}(4.9\,\text{K}) = 33.4\,\text{nm}$, which results in $n_{sat} \approx 13$. This also suggests the presence of multiquanta vortices in the antidots at the matching fields $\pm B_2$ and $\pm B_{5/2}$.

8.3.2. Identification of fractions

Detailed fractional matching fields were observed in the measurements on the Nb-HgTe samples, as shown in figure 8.12. The data were obtained at 3.61 K and 3.64 K, both corresponding to $T/T_c \approx 0.79$. To ensure that the visible features are not due to noise, both curves were recorded multiple times and then averaged over the available number of measurements. Both curves show pronounced dips at the integer matching fields $\pm B_1$, as well as several additional smaller resistivity dips. These smaller dips have been assigned to the fractional matching fields shown in the figure.

Fractional matching fields with denominators $q = 2$, 3, and 6 have been identified. These are displayed at the bottom of the graph. Additionally, fractional matching fields with denominators $q = 4$, 7, 8, and 9 have been identified and are shown at the top of the graph. The matching fields $\pm B_{1/8}$ and $\pm B_{7/8}$ appear as weakly visible shoulders rather than dips, but their magnetic field value corresponds exactly to the expected value of the fraction.

The following peculiarities can also be observed. The most pronounced fractional matching field is $\pm B_{1/2}$. There is no discernible difference in the depth of the resistivity dips of the other matching fields. Intriguingly, a small peak can be seen exactly in the centre of the larger dip at $\pm B_{1/2}$. The reason for this feature remains unclear.

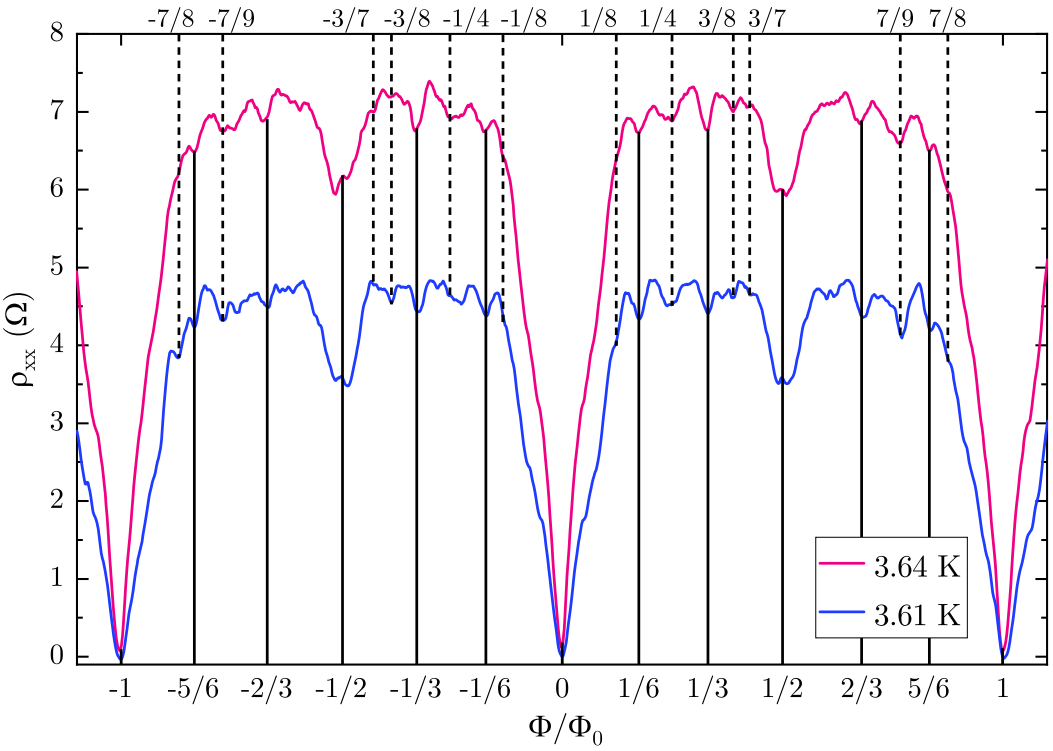

Fig. 8.12.: Analysis of fractional matching fields in Nb-HgTe. The curves show ρ_{xx} vs reduced flux Φ/Φ_0 obtained on the 200 nm periodic antidots shown in figure 8.2 (a). The data are shown from $-B_1$ to B_1 for 3.61 K (blue, data averaged over 8 curves) and 3.64 K (magenta, data averaged over 15 curves). The curves are symmetrical around $B = 0$ T. Fractional matching fields $B_{p/q}$ are assigned to the dips in ρ_{xx}. The absolute deviation of the mathematical value of the indicated fraction p/q to the experimentally determined magnetic field value B of the resistivity minimum is less than 1 mT for all fractions. The data were measured with the AC lock-in technique at 53 Hz at 300 nA.

A comparison with a sample containing Nb antidots based on SiO_2 will now be shown. In the 200 nm periodic antidots shown in figure 8.1 (a), integer matching fields and fractional matching fields at $\pm B_{n+1/2}$ with $n \in \mathbb{N}_0$ could be observed. Figure 8.13 demonstrates that the number of observable fractional dips is limited to this and there are no fractions with a denominator other than 2.

The cause of the numerous fractional matching fields observed in the Nb-HgTe samples, but not in the Nb-SiO_2 samples, is unclear and can only be hypothesized. Section 8.1 showed significant differences in the normal resistivity ρ^n_{xx} and the critical temperature T_c of the two samples. As described there, this indicates that the quality of the Nb in the Nb-HgTe sample is significantly poorer than the Nb quality of the Nb-SiO_2 sample [165, 166]. The sputtered Nb in the Nb-HgTe sample may therefore have more material defects or surface irregularities. These defects can weakly pin interstitial vortices [33]. This could stabilise the complicated configurations of the fractional matching fields and

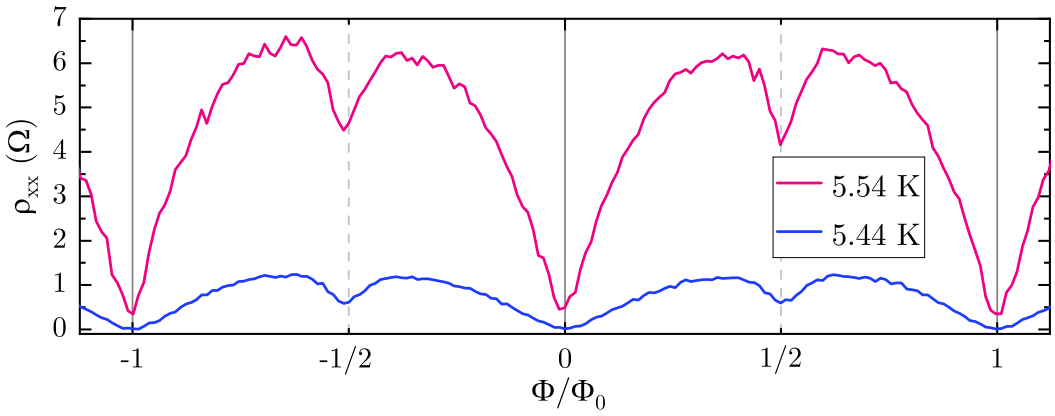

Fig. 8.13.: Analysis of fractional matching fields in Nb-SiO_2. The curves show ρ_{xx} vs reduced flux Φ/Φ_0 obtained on the 200 nm periodic antidots shown in figure 8.1 (a). The data are shown from $-B_1$ to B_1 for 5.44 K (blue) and 5.54 K (magenta). No Nb-SiO_2 samples exhibited any fractional matching fields other than $\pm B_{n+1/2}$ with $n \in \mathbb{N}_0$. The data were measured with the AC lock-in technique at 100 nA and 43 Hz.

enable their observation.

It would be interesting to see a connection to the underlying insulator. In contrast to the trivial insulator SiO_2, the topological insulator HgTe also has conductive topological surface states in the band gap. If the HgTe is proximitized by the superconducting Nb, the vortex lattice may expand into the underlying topological insulator, similar to the effect observed by Stolyarov et al. [170]. However, a clear explanation linking this idea to the observed features has not yet been established.

8.3.3. High-field fractional matching effects

The pronounced fractional pinning could be observed in the Nb-HgTe samples not only within the first integer matching field but also within higher integer matching fields. Figure 8.14 illustrates this phenomenon with data up to B_5. The specific assignment of fractions to resistivity dips is not provided here. This is due to the inadequate spacing of the data points as a function of the magnetic field, which does not allow definitive conclusions to be drawn. Nevertheless, several features can be observed.

The resistivity curve shows very pronounced fractional dips. The curve was recorded at 3.46 K, i. e. $T/T_c = 0.75$. The temperature was close to 3.33 K, which is the temperature at which the resistivity drops to zero within the observed magnetic field interval. During the course of this thesis such pronounced dips have often been observed in this low temperature regime, as opposed to at higher temperatures near T_c. This is unexpected, given that the lower edge of the Hofstadter butterfly spectrum corresponds to the T_c phase boundary. One would therefore expect the strongest fractional features to appear close

to T_c. Moreover, there are regions with high resistivity, suggesting that the corresponding pinning configurations are particularly unstable at these fields. These can be seen, for example, at $\Phi/\Phi_0 = 2.63$, 3.63, and 4.63.

The cyan curve was recorded at positive magnetic fields. The dark blue curve was recorded at negative magnetic fields, and then mirrored on the ordinate axis. The measurements overlap well, demonstrating that the data are symmetrical around $B = 0$. However, the fractal fine structures of the individual integer oscillations are not perfectly symmetrical around their respective centres $\pm B_{n+1/2}$ with $n \in \mathbb{N}_0$. This is in contrast to the symmetrical Hofstadter butterfly [13].

Some differences to the experiment of Pannetier et al. [12] described in section 7.3.3 should be noted. Pannetier's data were obtained from superconducting aluminium antidots, rather than Nb. These were fabricated on SiO_2, which is a trivial insulator and not a topological insulator. The antidots had a periodicity of 6 µm with a square shape and a diameter of 4 µm. This is 30 times larger than the 200 nm periodic antidots with the observed fractional matching fields analysed in figure 8.12. The measurement technique used was also different. The resistance was kept at a constant value of 0.1 Ω by regulating the temperature. Therefore he was able to keep the temperature at $T = T_c(B)$. This allowed for the critical temperature curve to be obtained at a fixed resistance rather than

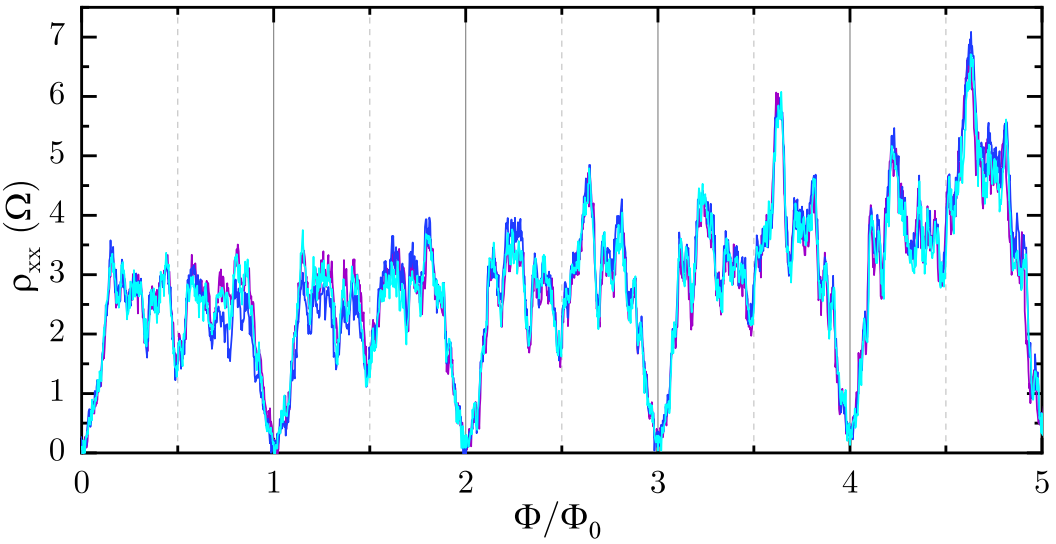

Fig. 8.14.: High-field fractional matching fields up to B_5. The data were obtained on a sample with 200 nm periodic antidots on HgTe (see figure 8.2 (a)). Three curves are presented: one was recorded from B_0 to B_5 (cyan), and another from B_5 to B_0 (magenta). Both overlap well, demonstrating that the observed features are not random resistance fluctuations and that the apparently noisy data are in fact highly reproducible. The third curve (dark blue) was obtained at negative magnetic fields and mirrored on the y-axis at $B = 0$. This curve also overlaps with the other two curves, demonstrating excellent axis symmetry. The data were obtained using the AC lock-in technique at 53 Hz and 3.46 K.

the resistance curve at a fixed temperature. The measurements in this thesis demonstrate significantly more pronounced fractional matching fields compared to those reported in Pannetier's paper. It is possible that all of these factors contribute to this difference.

It can be concluded that the fractional fine structure of the resistivity indicates complex but stable lattice configurations of the pinned vortices. The influence of the HgTe on the pinning effects remains unclear. Furthermore, it is worth noting that some antidot samples had a topgate, but no influence of the topgate voltage on the pinning properties was observed.

9. Summary and outlook

This thesis presents two different experiments. The first experiment investigates a 3D TI based on HgTe at high magnetic fields and millikelvin temperatures using transport and capacitance measurements [19]. For the second experiment, a Nb film is additionally deposited on this 3D TI. The Nb film is perforated with a lattice of periodically arranged antidots and becomes superconducting at low temperatures [129]. This heterostructure consisting of TI and superconductor was investigated with magnetotransport measurements.

The first experiment involved tuning the Fermi energy in the HgTe by applying a voltage to a top gate. By obtaining the conductivity in a Hall bar geometry through transport measurements and plotting it on a 2D colour plot against gate voltage and magnetic field, a complex pattern of overlapping Landau fans can be observed [69]. In contrast to transport, capacitance measurements only probe the uppermost charge carrier layer, specifically the top surface of the 3D TI [39]. Therefore they display only a single Landau fan corresponding to the top surface. By comparing the complex pattern from transport with the single Landau fan from capacitance, the LLs corresponding to the top surface can be identified. Throughout the entire gate voltage range, bulk electrons from the CB or bulk holes from the VB are present due to the electrostatics of the analysed wafer. These bulk carriers also form LLs and are therefore 2D systems. The bulk carriers shield the bottom surface carriers from the influence of the topgate. Consequently, the LLs of the bottom surface reflect a constant carrier density, which can be seen from their appearance as horizontal lines in the transport colour plots. The carrier densities were determined for all carrier systems. These observations were made below a magnetic field of 6 T, but for magnetic fields above 14 T the situation changes fundamentally. The transport measurements show only a single remaining Landau fan. The capacitance also shows LLs at these high magnetic fields, which are in good agreement with the transport LLs. The electron carrier density above 14 T can be determined from the 1/B periodicity of the LL. It corresponds well to the sum of the carrier densities of the top surface electrons, the bottom surface electrons and the bulk electrons obtained below 6 T. The conclusion is that below 6 T several 2D carrier systems coexist. As the magnetic field increases, i. e. between $6 - 14$ T, the carriers are redistributed. Finally, above 14 T, only a **single 2D system remains**, reflecting the total electron carrier density. The transport measurements are sensitive to all charge carrier types at each of the

three magnetic field intervals, while the capacitance exclusively probes the top surface below 6 T and the remaining 2DES above 14 T.

The mechanism of carrier redistribution between $6 - 14$ T remains unclear. Within this magnetic field range, the LLs observed in the capacitance measurements do not correspond to any of the LLs observed in the transport measurements, which is surprising. Rather, it is expected that the LLs visible in the capacitance measurements represent a subset of the LLs visible in the transport measurements. Only the extended states of the LL, i. e. the LL centres, contribute to the longitudinal conductivity in the transport measurements [66, 77]. On the other hand, the capacitance measurements are directly proportional to the thermodynamic density of states of the system at the Fermi energy, which includes the localised states of the LL [41, 94, 95]. This may explain the discrepancy between capacitance and transport between $6 - 14$ T, as capacitance may reveal localised states not detected by transport measurements. However, a comprehensive theory describing this and explaining the exact process of carrier redistribution has not yet been developed.

In a second experiment, a layer of Nb, which is a type-II superconductor at low temperatures, was deposited on the 3D TI. The Nb layer is perforated with an array of antidots, i. e. periodically arranged, cylindrical cavities. When a magnetic field is applied perpendicular to the Nb layer and the temperature is below the superconducting transition temperature, vortices form with the flux of the superconducting flux quantum [132, 133]. In an unperforated superconductor, these vortices can arrange themselves in a flux quantum lattice [9]. Here, however, the vortices can become trapped in the antidots, a phenomenon known as pinning [33]. This pinning property is particularly pronounced at the so-called matching fields, which occur whenever there is commensurability between the periodicity of the flux quantum lattice and the periodicity of the antidot pinning array [171]. These matching fields indicate the number of flux quanta per unit cell of the antidot lattice. The pinning property is evident in the transport measurements as oscillations of the longitudinal resistivity of the Hall bar with respect to the magnetic field. The magnetic field values of the resistivity minima of the oscillations are in very good agreement with the theoretically predicted matching fields. Pronounced integer pinning was observed up to matching fields in the low double-digit range. At higher matching fields, interstitial vortices may form between the antidots due to vortex-vortex repulsion [144, 163, 164]. However, the analysis indicates that multi-quanta vortices, in which several flux quanta are located together in one antidot, are preferentially formed [162]. Additionally, the current dependence of the pinning was investigated. The results, displayed in a 2D colour plot, show a pattern resembling a pine tree, demonstrating that the vortices still pin in the antidots even at currents in the microampere range. Furthermore, besides the integer matching fields, **pronounced fractional matching fields** were

observed. These indicate complex but stable lattice configurations of the vortices. Intriguingly, the observed fractional fine structure of the resistivity oscillations is related to the lower edge of the Hofstadter butterfly energy spectrum [12, 13]. To investigate the influence of the TI HgTe beneath the Nb, samples with Nb antidots on the trivial insulator SiO_2 were prepared for comparison. However, the fractional matching fields observed in these samples were limited to a few simple fractions.

Nevertheless, it remains unclear whether the observation of the pronounced fractional features in the Nb-HgTe samples are a consequence of the 3D TI. The comparison samples on SiO_2 exhibit fewer fractional matching fields, but they also possess a higher quality of Nb. This was demonstrated by measurements of normal resistivity and critical temperature [165, 166]. The lower quality of the Nb on the HgTe samples may indicate the presence of an increased number of material defects or surface irregularities. These defects can pin interstitial vortices, which could stabilise complex lattice configurations of the vortices and thus enable the observation of fractional matching fields [138, 161]. To investigate this, one option is to fabricate samples based on HgTe and SiO_2 with identical Nb antidot geometries using the same sputtering process.

In addition, it is worth noting that no signs of MBS were observed in the pinning experiments. It is expected that MBS will occur only when the superconducting Nb proximitizes the HgTe [28]. Our research group has demonstrated that the superconducting proximity effect takes place at millikelvin temperatures for the wafers and sample fabrication techniques employed [34, 35, 104]. However, the vortex pinning measurements were made just below the superconducting transition temperature, in the range of a few kelvins. Therefore, it is not expected that the HgTe is proximitized by the superconducting Nb, and as a result, no MBS are expected to occur.

The question that remains is whether there are any **indications of MBS in the capacitance** measurements. The experiments described in this thesis were initially motivated by this objective. For MBS to occur in this experiment, a number of prerequisites are necessary. First, a 3D TI with TSS is required [26, 28]. The HgTe based TIs, which are theoretically described in chapter 2 and experimentally analysed in chapter 6 of this thesis and other publications of our research group, fulfil these criteria [39, 68, 69]. Furthermore, the sample fabrication process needs to be developed and optimised to create a superconducting antidot array on the HgTe, as described in chapter 4. In addition, a magnetic field perpendicular to the sample geometry must be applied with a value corresponding to the first integer matching field. The theory behind this is explained in chapter 7. This implies that there is exactly one vortex with one flux quantum in each antidot. Moreover, the AC currents used in the capacitance measurements must not depin the flux quanta. Both requirements can be met as shown in the experiments in chapter 8. On top of that, the superconducting

Nb must proximitize the 3D TI. With the fabrication steps and wafers used, this is achievable and occurs at millikelvin temperatures [34, 35, 104]. According to theory, MBS can form in the antidots when all these conditions are met [36, 37]. The additional density of states from the MBS lies at zero energy [28]. Chapter 3 explains that the density of states is reflected in the quantum capacitance. The quantum capacitance can be detected through capacitance measurements using a top gate, as detailed in chapter 5. Chapter 6 successfully demonstrated the feasibility of the measurement techniques to obtain the quantum capacitance, but only on HgTe Hall bars without Nb. Therefore, an additional test was carried out on a sample where half of the surface area was covered with Nb. The results reported in appendix B.4 demonstrate that the quantum capacitance can still be detected when half of the capacitor plate is a metal. However, the signal is attenuated accordingly. Although all of the above prerequisites have been met successfully, the capacitance measurements of the samples of HgTe with Nb antidots do not show any significant signal modulation, as reported in appendix B.5.

There could be several reasons for this. Firstly, it is possible that the capacitance signal is too attenuated due to the ratio of Nb area to HgTe area, resulting in a poor signal-to-noise ratio. However, this is contradicted by the fact that even in samples where the antidots are large compared to the Nb area, no MBS were observed.

Furthermore, the amplitude of the excitation voltage used in capacitance measurements may be too high, leading to an averaging of states over a wide energy interval in the band structure. This could be problematic for the following reason: The MBS are located at the centre of the gap of the induced superconductivity [28]. Fischer et al. [34] estimated the induced gap to be approximately half the size of the superconducting gap, with a lower limit of one-eighth. To selectively detect only the MBS in the gap of the induced superconductivity, a correspondingly small voltage amplitude is required. However, reducing the voltage amplitude increases the noise in the measured signal. To address this issue, a cold amplifier, such as an integrated capacitance bridge, can be used to amplify the signal in the cryostat [172, 173]. As part of this thesis, an attempt was made to construct such a bridge. The corresponding electronic circuit is shown in appendix B.6. However, the technical progress did not go beyond the results presented in the references, and the capacitance signals obtained when testing the integrated capacitance bridge were no better than those obtained using lock-ins or the AH 2700 A bridge.

Another issue is that at millikelvin temperatures the flux quanta are strongly pinned, either in the antidots or as interstitials. To measure capacitance as a function of magnetic field, it is not sufficient to simply sweep the external magnetic field. Instead, after obtaining the capacitance data at a fixed magnetic field, the sample must be heated above the critical temperature, the magnetic

field changed, the sample cooled and the next capacitance data measured. This process must be repeated for each desired magnetic field. For example, comparing capacitance data at millikelvin temperatures with and without flux quanta in the antidots, i. e. with and without MBS, is only possible using this method. However, the ^{3}He/^{4}He dilution refrigerator used makes this method a very challenging task, as the ^{3}He/^{4}He mixture would have to be condensed and stored separately in tanks each time. Alternatively, the sample could be heated using a heating element such as a resistor. However, this would also heat the ^{3}He/^{4}He mixture, which would presumably evaporate before the critical temperature of Nb could be reached.

In conclusion, this thesis has demonstrated that the 3D TI based on HgTe provides a platform for various exciting effects. Additionally, the antidot lattice based on superconducting Nb also offers a wide range of potential experiments. If capacitance measurements can be achieved that reveal MBS in the heterostructure of the two material layers, the next exciting step would be to braid the non-Abelian MBS, i. e. to interchange two MBS [32]. Akzyanov et al. [174] proposed an experimental realization of braiding based on vortex MBS. However, rather than attempting the very complex process of braiding, the **fusion of two MBS** would be a much simpler process. This involves bringing two MBS close together until their zero-energy modes overlap and split. In the experiment described in the initial motivation for this doctoral thesis, achieving this objective would be straightforward. The magnetic field could be set to a value that yields the second integer matching field. This would result in two vortices per antidot and consequently the fusion of two MBS. According to Beenakker [31], the fusion of MBS would already be sufficient to demonstrate non-Abelian statistics. Therefore, this theoretically simple fusion experiment could have a potentially revolutionary impact on the current state of physics.

A. Sample fabrication

In this appendix, the individual steps of the sample fabrication of an HgTe Hall bar with Nb antidots and topgate are listed.

Wafer dicing

Process step	Description and parameters
Cleaning	60 s acetone 60 s isopropyl alcohol drying with N_2 gun
Resist application	S1813 photoresist, spin coating at 1000 min^{-1}, 1000 min^{-1} s^{-1}, 30 s baking at 80 °C for 5 min
Wafer dicing	with a diamond scriber into samples with size 4 x 4 mm, repeating each scribe 4-5x breaking of the wafer along scribed edges
Quality control	with optical light microscope

Mesa structuring

Process step	Description and parameters
Cleaning	60 s acetone 60 s isopropyl alcohol drying with N_2 gun
Resist application	S1813 photoresist spin coating at 8000 min^{-1}, 4000 min^{-1} s^{-1}, 30 s baking at 80 °C for 3 min
Optical lithography	at 275 W for 80 s
Resist development	with MF-26A developer for 30 s distilled H_2O for 30 s development stop drying with N_2 gun

Chemical wet etching	with Br_2:$C_2H_6O_2$:H_2O = 0.1 mL:100 mL:25 mL, at 0 °C for 4 min, stirred at 300 min^{-1}, shaking of the sample every 30 s distilled H_2O for 5 s to stop etching drying with N_2 gun
Resist removing	60 s acetone 60 s isopropyl alcohol drying with N_2 gun
Etching depth control	with Dektak

Antidot fabrication

This section can be skipped for samples without Nb antidots. The recipes were optimised for a total of three different resists. First the recipes based on the positive resists (a) CSAR and (b) PMMA are described in bullet points. Then the recipe for the negative resist (c) AR-N 7520 is given.

(a) Based on **CSAR resist**:

Process step	Description and parameters
Cleaning	60 s acetone 60 s isopropyl alcohol drying with N_2 gun
Resist application	CSAR 9 % EBL resist spin coating, first at 3000 min^{-1}, 3000 min^{-1} s^{-1}, 5 s, then at 6000 min^{-1}, 2500 min^{-1} s^{-1}, 60 s baking at 80 °C for 20 min
Electron beam lithography	at 30 kV, 20 µm aperture, roughly 100 pA beam current and 700 pC cm^{-1} line dose
Resist development	with AR-600-546 for 30 s isopropyl alcohol for 30 s development stop drying with N_2 gun
Metallization	in-situ in UHV: Ar^+-etching for 27 s at 100 V 3 nm of Ti with electron gun, 100 mA 30 nm of Nb with Ar^+-sputtering, at 250 W 3 nm of Pt with electron gun, at 500 mA
Resist lift-off	in AR-600-71 for 90 s syringe pressure and ultrasonic application in AR-600-71

	isopropyl alcohol drying with N_2 gun
Quality control and documentation	with scanning electron microscope

(b) Based on **PMMA double resist** layers:

Cleaning	60 s acetone 60 s isopropyl alcohol drying with N_2 gun
Double layer resist application	PMMA 50K 9 % EBL resist spin coating at 6000 min^{-1}, 4000 min^{-1} s^{-1}, 30 s baking at 80 °C for 20 min PMMA 200K 9 % EBL resist spin coating at 6000 min^{-1}, 4000 min^{-1} s^{-1}, 30 s baking at 80 °C for 20 min
Electron beam lithography	at 30 kV, 30 µm aperture, roughly 150 pA beam current and 2500 pC cm^{-1} line dose
Resist development	with MIBK:isopropyl alcohol = 1:3 for 90 s isopropyl alcohol for 30 s development stop drying with N_2 gun
Chemical wet etching	with Br_2:$C_2H_6O_2$:H_2O = 1 drop:100 mL:25 mL, at 0 °C for 30 s, stirred at 300 min^{-1} distilled H_2O for 5 s to stop etching drying with N_2 gun
Metallization	in-situ in UHV: Ar^+-etching for 10 s at 100 V 3 nm of Ti with electron gun, 100 mA 30 nm of Nb with Ar^+-sputtering, at 250 W 3 nm of Pt with electron gun, at 500 mA
Resist lift-off	in acetone at 60 °C for 24 h syringe pressure and ultrasonic application in aceton isopropyl alcohol drying with N_2 gun
Quality control and documentation	with scanning electron microscope

(c) Based on **negative resist**:

Process step	Description and parameters
Cleaning	60 s acetone 60 s isopropyl alcohol drying with N_2 gun
Resist application	under yellow light: AR-N 7520 11 % EBL negative resist spin coating, 4000 min^{-1}, 1000 min^{-1} s^{-1}, 60 s baking at 80 °C for 3 min resist application process is performed twice to produce a thicker resist film
Electron beam lithography	sample must not be exposed to daylight during transportation to the scanning electron microscope at 30 kV, 20 µm aperture, roughly 75 pA beam current and 1 - 10 fC point dose
Resist development	under yellow light: with AR-300-47 for 50 s distilled H_2O for 60 s to stop development drying with N_2 gun resist can now be exposed to daylight
Metallization	in-situ in UHV: Ar^+-etching for 27 s at 100 V 3 nm of Ti with electron gun, 100 mA 30 nm of Nb with Ar^+-sputtering, at 250 W 3 nm of Pt with electron gun, at 500 mA
Resist lift-off	in AR-300-76 at 60 °C for at least 24 h syringe pressure and ultrasonic application in AR-300-76 isopropyl alcohol drying with N_2 gun
Quality control and documentation	with scanning electron microscope

Insulator deposition

Process step	Description and parameters
SiO_2 deposition	30 nm of SiO_2 with PECVD; 3 x 15 s SiH_4/N_2O, gas flow 710/170 sccm, 80 °C, 150 W

Al_2O_3 deposition	80 nm of Al_2O_3 with ALD; with C_3H_9Al and H_2O precursors, at 80 °C, 66 s purge time, 15 ms pulse, 1000 cycles

Metallization

Process step	Description and parameters
Cleaning	60 s acetone 60 s isopropyl alcohol drying with N_2 gun
Resist application	S1813 photoresist spin coating at 8000 min^{-1}, 4000 min^{-1} s^{-1}, 30 s baking at 80 °C for 3 min
Optical lithography	at 275 W for 80 s
Resist development	with MF-26A developer for 30 s distilled H_2O for 30 s to stop development drying with N_2 gun
Metallization	5 nm of Ti with Univex, 1.0 Å/s 70 nm of Au with Univex, 1.4 Å/s
Resist lift-off	in acetone at 60 °C for 24 h syringe acetone pressure application isopropyl alcohol drying with N_2 gun

Chip carrier contacting

Process step	Description and parameters
Gluing	into standard chip carrier with PMMA resist baking at 80 °C for 20 min
Bonding	with gold wire first bond on chip carrier (connected) and second bond on contact pad (not connected)
Soldering	soldering the disconnected second bond using indium with soldering iron settings 6 V and 1 A
Quality control	checking the mechanical stability of each bond by carefully pulling on it with a thin needle

	verifying electrical contact in the measuring set-up if required, again soldering

B. Supplementary data

B.1. Estimation of geometric capacitance

In this appendix, the total geometric capacitance of the modulation-doped wafer and the insulators deposited on it is estimated for the geometry of the measured samples.
The overlap of topgate and mesa, which is decisive for the geometric capacitance, is known to be $105\,500\,\mu m^2$ from lithographic files and microscopic images. Furthermore, it is assumed that the top surface 2DES sits 6 nm below the HgTe-CdHgTe interface [39].
The layer thicknesses, obtained from a private conversation with N. N. Mikhailov, are shown in figure 4.6. The thickness of the Al_2O_3 was estimated from the number of deposition cycles. According to Gieraltowska et al. [111] 1000 cycles result in 80 nm. The relative permittivities are taken from the supplemental of Kozlov et al. [39]. The parameters of the relevant insulating materials are summarized here:

Insulator	Thickness (nm)	Relative permittivity
Al_2O_3	80	9
SiO_2	30	3.5
CdTe	40	10.2
CdHgTe	20	13
HgTe	6	21

With equation 3.26 it follows that the total geometric capacitance

$$C_{geo} = \left(\frac{1}{C_{geo,\ Al_2O_3}} + \frac{1}{C_{geo,\ SiO_2}} + \frac{1}{C_{geo,\ CdTe}} + \frac{1}{C_{geo,\ CdHgTe}} + \frac{1}{C_{geo,\ HgTe}} \right)^{-1} = 40.3\,\text{pF}. \tag{B.1}$$

B.2. Characterization of wafer 150213

This section provides a brief characterisation of wafer 150213, which was used in the pinning experiments in chapter 8. The available data are limited, but are sufficient to determine the VB edge and the CB edge. The measurements are presented in figure B.1.

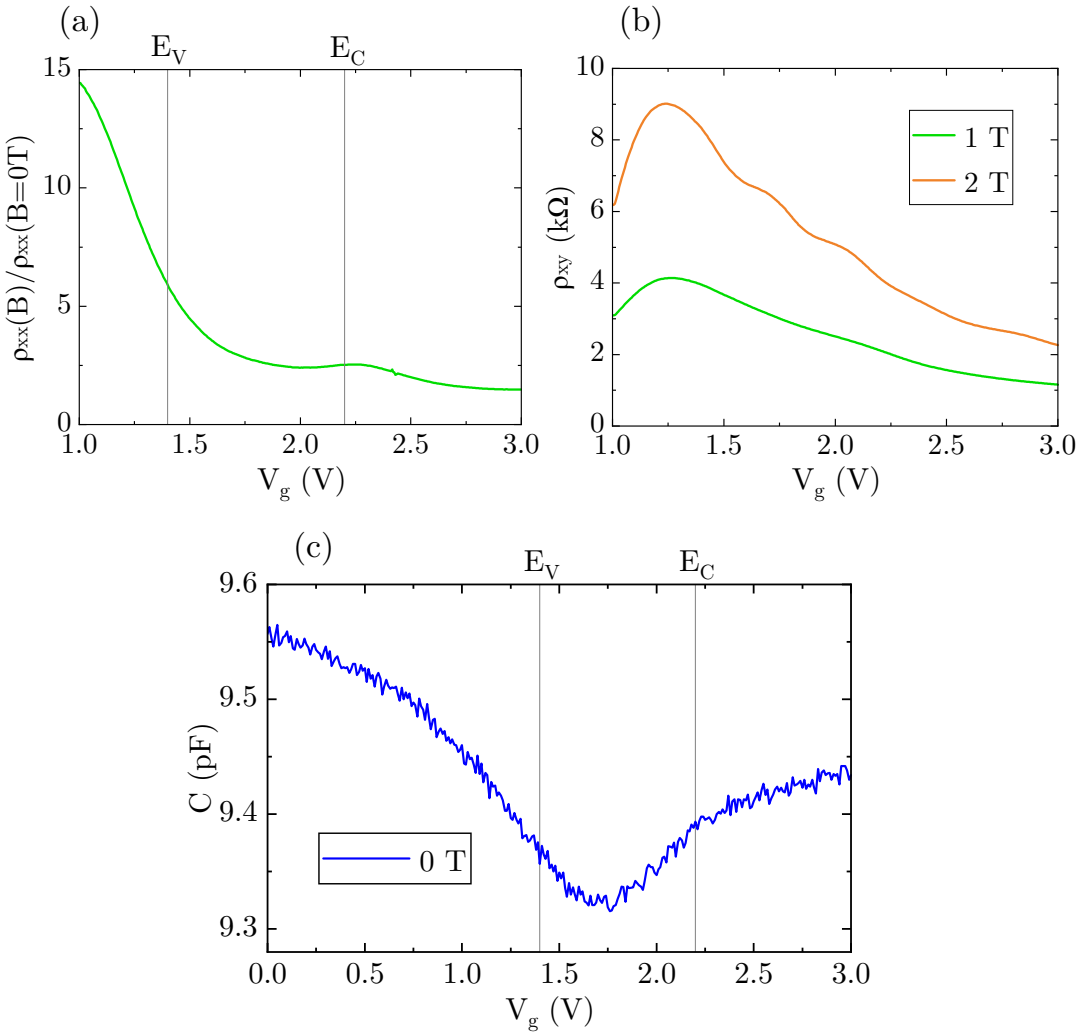

Fig. B.1.: Normalized $\rho_{xx}(B)$, $\rho_{xy}(B)$, and C vs V_g. (a) Shown is $\rho_{xx}(B = 1\,\mathrm{T})$ normalized to $\rho_{xx}(B = 0)$ as a function of gate voltage V_g. The VB edge sits approximately at 1.4 V. The weak hump at 2.2 V indicates the CB edge E_C. The large resistivity below 1 V indicates that the CNP sits below 1 V. (b) Shown is $\rho_{xy}(B)$ as a function of gate voltage V_g. ρ_{xy} changes sign approximately at the CNP. Due to the incomplete data this cannot be observed, however a linear extrapolation suggests that the CNP sits at around 0.7 V. The measurements were carried out with the AC lock-in technique at 1.5 K. (c) The capacitance data at 0 T confirms the positions of E_C and E_V. The capacitance was measured with the AH 2700A bridge at 1.5 K and 240 Hz.

B.3. Coherence length in unpatterned Nb films

This appendix presents a comparison between two distinct Nb-HgTe films on the same sample. Figure B.2 (a) shows the first film has antidots with a periodicity of 800 nm produced with the negative resist recipe. The other film consists of unpatterned Nb. Both films were produced in the same sputtering process and are therefore well comparable.

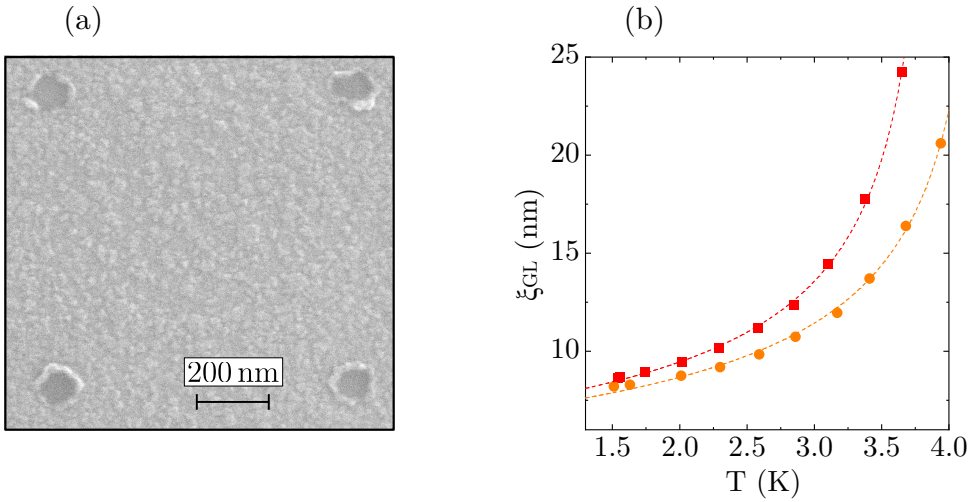

Fig. B.2.: SEM image of 800 nm periodic antidots and ξ_{GL} vs T. (a) The top view SEM image shows round antidots on HgTe with a periodicity of $a_{\square} = 800\,\text{nm}$. The diameter is $d_a = 60\,\text{nm}$. (b) The coherence length vs temperature is shown for the film with antidots (orange) and another film on the same sample with unpatterned Nb (red).

The $\xi_{GL}(T)$ data in figure B.2 (b) were fitted with equation 7.3. The fit converges in both cases and yields $\xi_{GL}(0\,\text{K}) = 6.38\,\text{nm}$ and $T_c = 4.36\,\text{K}$ for the area with antidots (orange). The result for the unpatterned Nb area (red) is $\xi_{GL}(0\,\text{K}) = 6.64\,\text{nm}$ and $T_c = 3.95\,\text{K}$.

Flux pinning effects at the theoretical integer matching fields $B_n = n \cdot 3.2\,\text{mT}$ with $n \in \mathbb{N}$ could not be observed in this sample.

B.4. Capacitance in Nb-HgTe heterostructures

This section investigates the extent to which quantum capacitance can be observed in capacitance measurements when part or all of the mesa layer is covered by a metal with a high density of states. The objective was to compare the capacitance of an HgTe-insulator-topgate structure with that of an Nb-HgTe-insulator-topgate structure.

For this, a simple sample was fabricated with three Hall bars based on wafer 150213 (see figure 4.1 (b)). The CdTe cap layer of the first Hall bar was removed

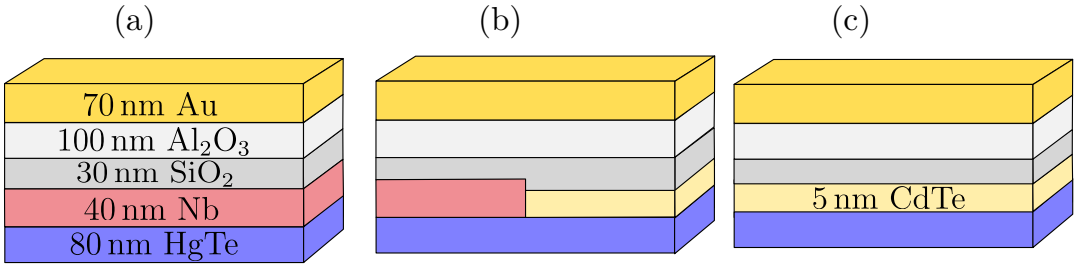

Fig. B.3.: Cross section, not to scale, of three Hall bars based on wafer number 150213. (a) The CdTe layer has been removed, and 3 nm Ti, 40 nm Nb, and 3 nm Pt have been deposited. (b) Exactly 51 % of the Hall bar's area has been treated similarly to figure (a). There is a small step in the insulators and the topgate due to the different height of the CdTe and the Nb, which is not shown here. (c) For the third Hall bar the 5 nm CdTe layer was not removed, and no metal has been deposited.

using Ar^+-etching. Subsequently, 3 nm Ti, 40 nm Nb, and 3 nm Pt were applied. The second Hall bar underwent the same procedure as the first, but with a crucial difference: only half of the surface area of the Hall bar had the CdTe removed and the metals were applied only to this half. The third Hall bar was left unprocessed. Next, 30 nm of SiO_2 and 100 nm of Al_2O_3 were applied to the entire sample. Finally, three individual top gates were added. The layer thicknesses are summarised in the figure B.3.

The capacitance of the three Hall bars was then measured as a function of the magnetic field, as shown in figure B.4. The Hall bar without metallisation shows oscillations stemming from Landau levels. The Hall bar with 100 %

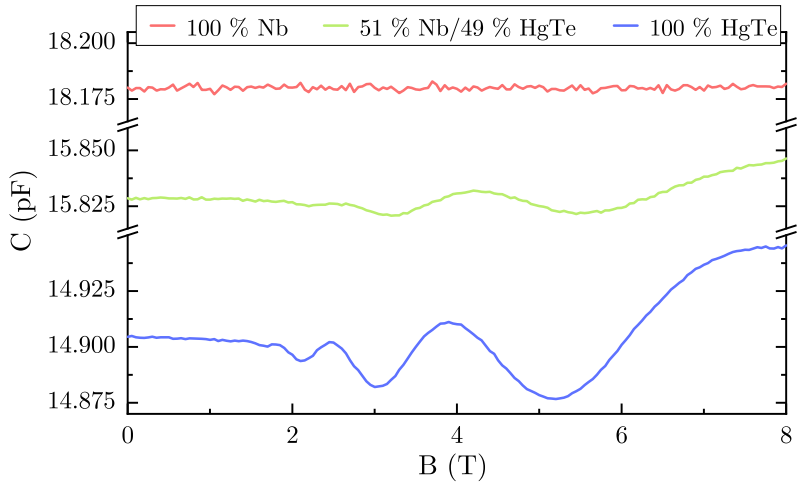

Fig. B.4.: Capacitance of the three Hall bars shown in figure B.3 as a function of magnetic field B. The legend refers to the uppermost conducting layer below the insulators. The y-axis has been broken at two points to allow the data to be plotted on one graph. The measurements were recorded with the AH 2700A bridge at 60 Hz, 1.4 K, and $V_g = 5$ V, which is close to the edge of the CB for the Hall bar without metallization.

metallisation shows no dependence of the capacitance on the magnetic field. The Hall bar with 51 % Nb and 49 % HgTe also exhibits oscillations, but their amplitude is attenuated. The conclusion is that it is possible to observe quantum capacitance in Nb-HgTe heterostructures when the Nb only partially covers the HgTe, however, the signal is attenuated.

The capacitance signals' absolute values differ amongst the individual Hall bars, ranging from approximately $\sim 14.9\,\mathrm{pF}$ to over $\sim 18.1\,\mathrm{pF}$. The absolute value is primarily composed of the geometric capacitance and parasitic capacitances. The geometric capacitance will be analysed first. It can be assumed that the insulators (SiO_2 and Al_2O_3) have a uniform thickness, as they are grown globally (i. e. on the entire sample) in one process. However, 5 nm of CdTe, which is also an insulator, has to be included in the calculation of the geometric capacitance for the areas lacking metallisation. Nonetheless, a rough estimate similar to the calculation in appendix B.1 indicates that this is insufficient to clarify the variation in the absolute value of the signal. Parasitic capacitance may therefore also play a role here, for instance due to the different lengths of the gold bonds of the three top gates, which interact capacitively with the mesa and the bonds of the mesa.

The capacitance of an HgTe sample where part of the mesa layer is covered by Nb, can be described by the circuit shown in figure B.5. The sample capacitance is the sum of the capacitance of the two branches, as they are parallel to each other. Each branch consists of C_{geo} and C_q in series. Therefore,

$$C_s = C_{HgTe} + C_{Nb} = \tag{B.2}$$

$$= \left(\frac{1}{C_{geo,HgTe}} + \frac{1}{C_{q,HgTe}}\right)^{-1} + \left(\frac{1}{C_{geo,Nb}} + \frac{1}{C_{q,Nb}}\right)^{-1} = \tag{B.3}$$

$$= C_{HgTe} + C_{geo,Nb}. \tag{B.4}$$

In the last step, it was accounted for that the density of states of metallic Nb is

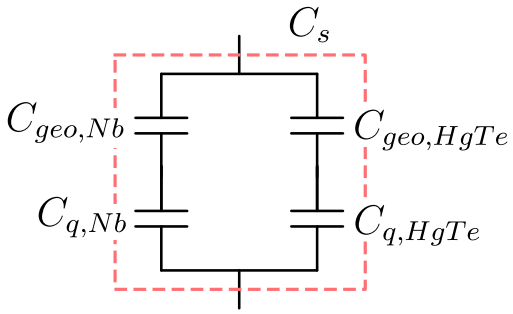

Fig. B.5.: Electrical circuit diagram describing the capacitance of figure B.4 (b). Here, the abbreviation Nb refers to the area of the Hall bar that is covered by Nb, while HgTe refers to the area of the Hall bar which is not covered by Nb. Parasitic capacitances are not considered here.

very large and therefore $C_{q,Nb} \to \infty$. The result of the equation confirms the possibility of observing the density of states in HgTe by capacitance measurements, even when part of the surface is covered with Nb.

The ratio of the respective areas of Nb and HgTe is crucial for determining the capacitance. This explains the attenuated amplitude of the Landau level oscillations of the green curve in figure B.4, as they stem from an area that is 49 % of the total area.

B.5. Capacitance in Nb antidots on HgTe

Here, the capacitance measurements on the heterostructures consisting of HgTe and Nb antidots are briefly discussed. Figure B.6 (a) shows ρ_{xx} on a sample with 200 nm periodic antidots just below T_c. Integer matching fields with a periodicity of $B = 52$ mT are observed, indicating that the vortices pin in the antidots. Figure B.6 (b) shows capacitance measurements on the same sample at different gate voltages. No modulation of the capacitance as a function of the magnetic field is observed.

The constant capacitance signal presented was a recurring image. There was no modulation as a function of the magnetic field, neither at temperatures slightly below T_c nor at millikelvin temperatures. Only a weak dependence on the top gate voltage was detected, which is likely a result of the band gap of

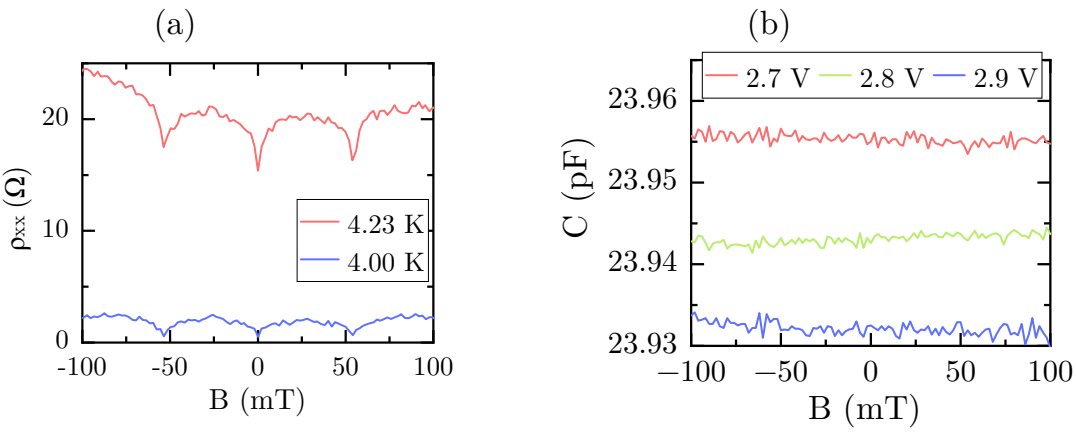

Fig. B.6.: Resistivity ρ_{xx} and capacitance C at small magnetic fields. (a) Integer matching fields in a sample with 200 nm periodic Nb antidots on HgTe. The data were obtained at different temperatures below T_c at a gate voltage of 0 V with the AC lock-in technique at 7 Hz. (b) The corresponding capacitance has been measured as a function of the magnetic field B for different gate voltages. While ρ_{xx} exhibits a clear field-dependent modulation, the capacitance remains constant. This constant capacitance in the HgTe samples with Nb antidots was a recurring pattern and occurred both when the temperature was slightly below T_c and at millikelvin temperatures. The capacitance was measured with the AH 2600A bridge at 100 Hz.

the HgTe, similar to the data shown in figure 6.7.

B.6. Integrated capacitance bridge

As part of this work, an integrated capacitance bridge (ICB) was designed. The bridge was developed to amplify the capacitance signal directly in the cryostat. This was based on the work of Verbiest et al. [173] and Hazeghi et al. [172]. However, the ICB did not yield better measurement data than the commercially available AH 2700 A bridge or when measuring capacitances with lock-ins.

Figure B.7 shows the electronic circuit of the ICB. The cryostat is depicted in blue, while the electronic components of the ICB are framed by a green dashed square. The $V_{\mathrm{AC,\,DUT}}$ signal passes through the device under test (DUT), i. e. the sample, while the $V_{\mathrm{AC,\,REF}}$ signal passes through a reference impedance Z_{REF}. Both AC signals can be phase and amplitude modulated. The two signals are superimposed just before the high-electron mobility transistor (HEMT). The superimposed signal is then amplified by the HEMT and sent to the AC voltmeter for detection. If the superimposed signal is zero, the bridge is balanced and the capacitance C_{DUT} can be calculated from the known amplitudes and phases of $V_{\mathrm{AC,\,DUT}}$ and $V_{\mathrm{AC,\,REF}}$. In addition, the top gate of the sample can be biased with $V_{\mathrm{g,\,DUT}}$ in order to tune the Fermi energy in the band structure, and the gate of the HEMT can be tuned with $V_{\mathrm{DC,\,REF}}$. The voltage $V_{\mathrm{DC,\,DS}}$ applied via a load resistor R_{load} additionally controls the current through the source-drain channel of the HEMT. The references offer a more comprehensive explanation of how the ICB operates.

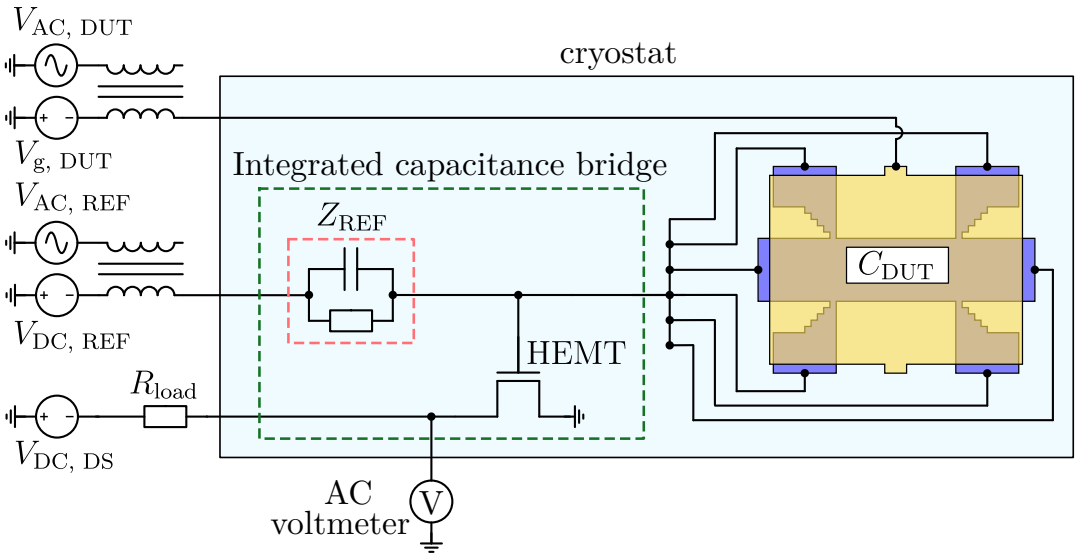

Fig. B.7.: Electrical circuit diagram of the ICB. The circuit is explained in the main text.

B.7. Transversal resistivity in antidot samples

In some samples with antidots, matching fields were also observed in the transversal resistivity ρ_{xy}, including fractional matching fields. Figure B.8 shows ρ_{xx} and ρ_{xy} as a function of magnetic field on a sample with 200 nm periodic Nb antidots on HgTe. The reason for this observation may be the exact geometry of the Hall bar: The Hall bar between the voltage taps was slightly widened, which could cause the current not to flow perfectly along the Hall bar, resulting in a transversal component. This, together with the physics described in section 7.2.4, might explain the features observed in ρ_{xy}.

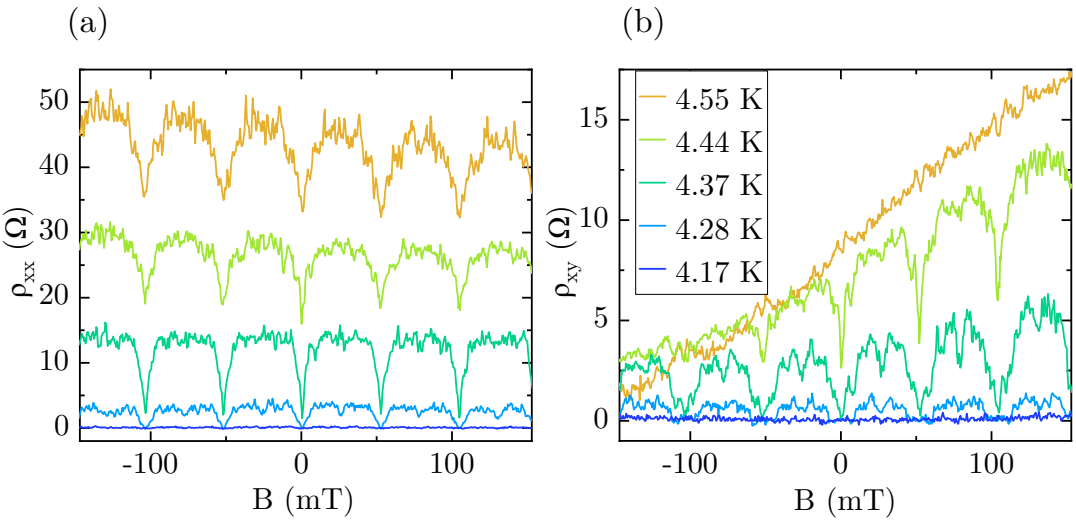

Fig. B.8.: Integer and fractional matching fields in ρ_{xx} and ρ_{xy}. The observation of matching fields in ρ_{xy} may be due to the current path through the sample, making the matching fields of trivial origin. The temperatures in figure (b) apply to both graphs. The data were recorded using the AC lock-in technique at 53 Hz.

List of Figures

Bibliography

[1] Hesiod and Homer, *Hesiod, the Homeric hymns and Homerica*, Evelyn-White, Hugh G (2012).

[2] S. Weart and M. Phillips, *History of physics*, eng, Vol. 2, Readings from physics today (American Inst. of Physics, New York, NY, 1985).

[3] H. Takayasu, *Fractals in the physical sciences*, eng, Nonlinear science (Manchester University Press, Manchester, 1990).

[4] J. He, X. Zhang, L. Dong, R. Zeng, and Z. Liu, "Fractal model of lightning channel for simulating lightning strikes to transmission lines", Science in China Series E: Technological Sciences **52**, 3135–3141 (2009).

[5] V. T. J. Phillips, M. Formenton, V. P. Kanawade, L. R. Karlsson, S. Patade, J. Sun, C. Barthe, J.-P. Pinty, A. G. Detwiler, W. Lyu, and S. A. Tessendorf, "Multiple environmental influences on the lightning of cold-based continental cumulonimbus clouds. Part I: description and validation of model", Journal of the Atmospheric Sciences **77**, 3999–4024 (2020).

[6] J. C. Maxwell, "VIII. A dynamical theory of the electromagnetic field", Philosophical Transactions of the Royal Society of London **155**, 459–512 (1865).

[7] D. van Delft and P. Kes, "The discovery of superconductivity", Physics Today **63**, 38–43 (2010).

[8] Ginzburg, V.L. and Landau, L.D., "On the theory of superconductivity", Sov. Phys. JETP, 20, 1064 (1950).

[9] A. A. Abrikosov, "The magnetic properties of superconducting alloys", Journal of Physics and Chemistry of Solids **2**, 199–208 (1957).

[10] A. A. Abrikosov, "Nobel Lecture: Type-II superconductors and the vortex lattice", Reviews of Modern Physics **76**, 975–979 (2004).

[11] C. Caroli, P. G. de Gennes, and J. Matricon, "Bound fermion states on a vortex line in a type II superconductor", Physics Letters **9**, 307–309 (1964).

[12] B. Pannetier, J. Chaussy, R. Rammal, and J. C. Villegier, "Experimental fine tuning of frustration: two-dimensional superconducting network in a magnetic field", Physical Review Letters **53**, 1845–1848 (1984).

[13] D. R. Hofstadter, "Energy levels and wave functions of Bloch electrons in rational and irrational magnetic fields", Physical Review B **14**, 2239–2249 (1976).

[14] J. D. Martin, "What's in a name change?", Physics in Perspective **17**, PII: 151, 3–32 (2015).

[15] L. Hoddeson, ed., *Out of the crystal maze, Chapters from the history of solid state physics*, eng (Oxford University Press, 1992).

[16] K. v. Klitzing, G. Dorda, and M. Pepper, "New method for high-accuracy determination of the fine-structure constant based on quantized Hall resistance", Physical Review Letters **45**, 494–497 (1980).

[17] Klaus von Klitzing, *The nobel prize in physics 1985*, edited by The Royal Swedish Academy of Sciences, Oct. 16, 1985.

[18] C. L. Kane and E. J. Mele, "Z2 topological order and the quantum spin Hall effect", eng, Physical Review Letters **95**, Journal Article, 146802 (2005).

[19] L. Fu, C. L. Kane, and E. J. Mele, "Topological insulators in three dimensions", eng, Physical Review Letters **98**, Journal Article, 106803 (2007).

[20] S.-Q. Shen, *Topological insulators, Dirac equation in condensed matters*, eng, Vol. 174, Springer series in solid-state sciences (Springer, Berlin and Heidelberg, 2012).

[21] B. A. Bernevig, T. L. Hughes, and S.-C. Zhang, "Quantum spin Hall effect and topological phase transition in HgTe quantum wells", eng, Science (New York, N.Y.) **314**, 1757–1761 (2006).

[22] M. König, S. Wiedmann, C. Brüne, A. Roth, H. Buhmann, L. W. Molenkamp, X.-L. Qi, and S.-C. Zhang, "Quantum spin hall insulator state in HgTe quantum wells", eng, Science (New York, N.Y.) **318**, 766–770 (2007).

[23] E. Majorana, "Teoria simmetrica dell'elettrone e del positrone", Il Nuovo Cimento **14**, 171–184 (1937).

[24] F. Guerra and N. Robotti, "The disappearance and death of Ettore Majorana", Physics in Perspective **15**, PII: 111, 160–177 (2013).

[25] C. C. Tsuei and J. R. Kirtley, "Pairing symmetry in cuprate superconductors", Reviews of Modern Physics **72**, 969–1016 (2000).

[26] L. Fu and C. L. Kane, "Superconducting proximity effect and majorana fermions at the surface of a topological insulator", eng, Physical Review Letters **100**, 096407 (2008).

[27] A. R. Akhmerov, J. Nilsson, and C. W. J. Beenakker, "Electrically detected interferometry of Majorana fermions in a topological insulator", eng, Physical Review Letters **102**, Journal Article, 216404 (2009).

[28] C. Beenakker, "Search for Majorana fermions in superconductors", Annual Review of Condensed Matter Physics **4**, 113–136 (2013).

[29] G. Moore and N. Read, "Nonabelions in the fractional quantum hall effect", Nuclear Physics B **360**, PII: 055032139190407O, 362–396 (1991).

[30] F. Wilczek, "Quantum mechanics of fractional-spin particles", Physical Review Letters **49**, 957–959 (1982).

[31] C. Beenakker, "Search for non-Abelian Majorana braiding statistics in superconductors", 10.21468/SciPostPhysLectNotes.15 (2020).

[32] C. Nayak, S. H. Simon, A. Stern, M. Freedman, and S. Das Sarma, "Non-Abelian anyons and topological quantum computation", Reviews of Modern Physics **80**, 1083–1159 (2008).

[33] V. V. Moshchalkov and J. Fritzsche, *Nanostructured superconductors*, eng (World Scientific, New Jersey, 2011).

[34] R. Fischer, J. Picó-Cortés, W. Himmler, G. Platero, M. Grifoni, D. A. Kozlov, N. N. Mikhailov, S. A. Dvoretsky, C. Strunk, and D. Weiss, "4-pi-periodic supercurrent tuned by an axial magnetic flux in topological insulator nanowires", Physical Review Research **4**, 10.1103/PhysRevResearch.4.013087 (2022).

[35] W. Himmler, R. Fischer, M. Barth, J. Fuchs, D. A. Kozlov, N. N. Mikhailov, S. A. Dvoretsky, C. Strunk, C. Gorini, K. Richter, and D. Weiss, "Supercurrent interference in HgTe-wire Josephson junctions", Physical Review Research **5**, 10.1103/PhysRevResearch.5.043021 (2023).

[36] A. L. Rakhmanov, A. V. Rozhkov, and F. Nori, "Majorana fermions in pinned vortices", Physical Review B **84**, 10.1103/PhysRevB.84.075141 (2011).

[37] R. S. Akzyanov, A. V. Rozhkov, A. L. Rakhmanov, and F. Nori, "Tunneling spectrum of a pinned vortex with a robust Majorana state", Physical Review B **89**, 10.1103/PhysRevB.89.085409 (2014).

[38] B. S. de Mendonça, A. L. R. Manesco, N. Sandler, and L. G. G. V. Da Dias Silva, "Near zero energy Caroli–de Gennes–Matricon vortex states in the presence of impurities", Physical Review B **107**, 10.1103/PhysRevB.107.184509 (2023).

[39] D. A. Kozlov, D. Bauer, J. Ziegler, R. Fischer, M. L. Savchenko, Z. D. Kvon, N. N. Mikhailov, S. A. Dvoretsky, and D. Weiss, "Probing quantum capacitance in a 3D topological insulator", eng, Physical Review Letters **116**, Journal Article, 166802 (2016).

[40] T. P. Smith, B. B. Goldberg, P. J. Stiles, and M. Heiblum, "Direct measurement of the density of states of a two-dimensional electron gas", eng, Physical review. B, Condensed matter **32**, Journal Article, 2696–2699 (1985).

[41] V. Mosser, D. Weiss, K. Klitzing, K. Ploog, and G. Weimann, "Density of states of GaAs-AlGaAs-heterostructures deduced from temperature dependent magnetocapacitance measurements", Solid State Communications **58**, 5–7 (1986).

[42] A. N. Grigorenko, G. D. Howells, S. J. Bending, J. Bekaert, M. J. van Bael, L. van Look, V. V. Moshchalkov, Y. Bruynseraede, G. Borghs, I. I. Kaya, and R. A. Stradling, "Direct imaging of commensurate vortex structures in ordered antidot arrays", Physical review. B, Condensed matter **63**, 10.1103/PhysRevB.63.052504 (2001).

[43] R. Gross and A. Marx, *Festkörperphysik*, ger, 3. Auflage, De Gruyter Studium (De Gruyter, Berlin and Boston, 2018).

[44] B. A. Bernevig and T. L. Hughes, *Topological insulators and topological superconductors*, eng (Princeton University Press, Princeton, NJ and Oxford, 2013).

[45] M. V. Berry, "Quantal phase factors accompanying adiabatic changes", Proceedings of the Royal Society of London. A. Mathematical and Physical Sciences **392**, 45–57 (1984).

[46] J. Zak, "Berry's phase for energy bands in solids", eng, Physical Review Letters **62**, Journal Article, 2747–2750 (1989).

[47] J. Kübler, *Theory of Itinerant Electron Magnetism*, eng, Second edition, Vol. 172, International series of monographs on physics (Oxford University Press, 2021).

[48] A. Altland and M. R. Zirnbauer, "Nonstandard symmetry classes in mesoscopic normal-superconducting hybrid structures", Physical review. B, Condensed matter **55**, 1142–1161 (1997).

[49] R. Kozlovsky, "Magnetotransport in 3D topological insulator nanowires" (Universität Regensburg, 2020).

[50] A. P. Schnyder, S. Ryu, A. Furusaki, and A. W. W. Ludwig, "Classification of topological insulators and superconductors in three spatial dimensions", Physical Review B **78**, 10.1103/PhysRevB.78.195125 (2008).

[51] C.-K. Chiu, J. C. Y. Teo, A. P. Schnyder, and S. Ryu, "Classification of topological quantum matter with symmetries", Reviews of Modern Physics **88**, 10.1103/RevModPhys.88.035005 (2016).

[52] L. Fu and C. L. Kane, "Topological insulators with inversion symmetry", Physical Review B **76**, 10.1103/PhysRevB.76.045302 (2007).

[53] M. Z. Hasan and C. L. Kane, "Colloquium: Topological insulators", Reviews of Modern Physics **82**, 3045–3067 (2010).

[54] T. Fukui, K. Shiozaki, T. Fujiwara, and S. Fujimoto, "Bulk-edge correspondence for Chern topological phases: a viewpoint from a generalized index theorem", Journal of the Physical Society of Japan **81**, 114602 (2012).

[55] Y. Ando, "Topological insulator materials", Journal of the Physical Society of Japan **82**, 102001 (2013).

[56] R. Roy, "Topological phases and the quantum spin Hall effect in three dimensions", Physical Review B **79**, 10.1103/PhysRevB.79.195322 (2009).

[57] S. H. Groves, R. N. Brown, and C. R. Pidgeon, "Interband magnetoreflection and band structure of HgTe", Physical Review **161**, 779–793 (1967).

[58] N. N. Berchenko and M. V. Pashkovskiĭ, "Mercury telluride—a zero-gap semiconductor", Soviet Physics Uspekhi **19**, 462–480 (1976).

[59] Z. D. Kvon, D. A. Kozlov, E. B. Olshanetsky, G. M. Gusev, N. N. Mikhailov, and S. A. Dvoretsky, "Topological insulators based on HgTe", Physics-Uspekhi **63**, 629–647 (2020).

[60] S. Tiwari, *Semiconductor Physics, Principles, theory and nanoscale*, eng, First edition, Vol. 3, Oxford scholarship online (Oxford University PressOxford, Oxford, 2020).

[61] S. Tiwari, *Nanoscale Device Physics, Science and Engineering Fundamentals*, eng, Electroscience Ser (Oxford University Press USA - OSO, Oxford, 2017).

[62] J. Gospodarič, V. Dziom, A. Shuvaev, A. A. Dobretsova, N. N. Mikhailov, Z. D. Kvon, E. G. Novik, and A. Pimenov, "Band structure of a HgTe-based three-dimensional topological insulator", Physical Review B **102**, 10.1103/PhysRevB.102.115113 (2020).

[63] K.-M. Dantscher, D. A. Kozlov, P. Olbrich, C. Zoth, P. Faltermeier, M. Lindner, G. V. Budkin, S. A. Tarasenko, V. V. Bel'kov, Z. D. Kvon, N. N. Mikhailov, S. A. Dvoretsky, D. Weiss, B. Jenichen, and S. D. Ganichev, "Cyclotron-resonance-assisted photocurrents in surface states of a three-dimensional topological insulator based on a strained high-mobility HgTe film", Physical Review B **92**, 10.1103/PhysRevB.92.165314 (2015).

[64] J. Ziegler, "Quantum transport in HgTe topological insulator nanostructures" (Universität Regensburg, 2019).

[65] S.-C. Wu, B. Yan, and C. Felser, "Ab initio study of topological surface states of strained HgTe", EPL (Europhysics Letters) **107**, 57006 (2014).

[66] H. Maier, "Geometrische Resonanzen in einem HgTe-basierten dreidimensionalen topologischen Isolator" (Universität Regensburg, 2023).

[67] C. Brüne, C. X. Liu, E. G. Novik, E. M. Hankiewicz, H. Buhmann, Y. L. Chen, X. L. Qi, Z. X. Shen, S. C. Zhang, and L. W. Molenkamp, "Quantum Hall effect from the topological surface states of strained bulk HgTe", eng, Physical Review Letters **106**, Journal Article, 126803 (2011).

[68] D. A. Kozlov, Z. D. Kvon, E. B. Olshanetsky, N. N. Mikhailov, S. A. Dvoretsky, and D. Weiss, "Transport properties of a 3D topological insulator based on a strained high-mobility HgTe film", eng, Physical Review Letters **112**, Journal Article, 196801 (2014).

[69] J. Ziegler, D. A. Kozlov, N. N. Mikhailov, S. Dvoretsky, and D. Weiss, "Quantum Hall effect and Landau levels in the three-dimensional topological insulator HgTe", Phys. Rev. Research **2**, 10.1103/PhysRevResearch.2.033003 (2020).

[70] E. H. Hall, "On a new action of the magnet on electric currents", American Journal of Mathematics **2**, 287 (1879).

[71] K. D. Weiss, "Untersuchungen zur Zustandsdichte eines zweidimensionalen Elektronengases in starken Magnetfeldern" (Technische Universität München, 1987).

[72] T. Ihn, *Semiconductor nanostructures, Quantum states and electronic transport*, eng, Reprinted with corrections (Oxford University Press, Oxford and New York, 2015).

[73] *Taschenbuch der Mathematik*, ger, 8., vollst. überarb. Aufl. (Deutsch, Frankfurt am Main, 2012).

[74] P. Drude, "Zur Elektronentheorie der Metalle", Annalen der Physik **306**, 566–613 (1900).

[75] L. Landau, "Diamagnetismus der Metalle", Z. Physik (Zeitschrift fuer Physik) **64**, PII: BF01397213, 629–637 (1930).

[76] J. H. Davies, *The physics of low-dimensional semiconductors, An introduction*, eng, Repr, Vol. 30, Literature, culture, theory (Cambridge Univ. Press, Cambridge, 2005).

[77] J. Weis, "Quantum Hall effect", in *Encyclopedia of Condensed Matter Physics* (Elsevier, 2024).

[78] General Conference on Weights and Measures, *On the revision of the International System of Units (SI), Resolution 1* (2018).

[79] L. Schubnikov and W. J. de HAAS, "A new phenomenon in the change of resistance in a magnetic field of single crystals of bismuth", Nature **126**, 500 (1930).

[80] H. L. Stormer, “Nobel Lecture: The fractional quantum Hall effect”, Reviews of Modern Physics **71**, 875–889 (1999).

[81] A. W. Gauß, “A scanning single-electron transistor array microscope probes the Hall potential profile in the fractional quantum Hall regime”, en (Universität Stuttgart, 2019).

[82] M. Kühn, “Experimental technique to resolve the compressible/incompressible droplet landscape in a (Al,Ga)As quantum Hall sample and Hall potential profiles in a 3D TI mercury telluride sample”, en (Universität Stuttgart, 2022).

[83] C. Beenakker and H. van Houten, *Solid state physics, Advances in research and applications*, eng, Vol. 44 (Academic Press, New York, NY, 1991).

[84] M. Büttiker, “Absence of backscattering in the quantum Hall effect in multiprobe conductors”, Physical review. B, Condensed matter **38**, 9375–9389 (1988).

[85] J. Weis and K. von Klitzing, “Metrology and microscopic picture of the integer quantum Hall effect”, eng, Philosophical transactions. Series A, Mathematical, physical, and engineering sciences **369**, 3954–3974 (2011).

[86] K. Panos, R. R. Gerhardts, J. Weis, and K. von Klitzing, “Current distribution and Hall potential landscape towards breakdown of the quantum Hall effect: a scanning force microscopy investigation”, New Journal of Physics **16**, 113071 (2014).

[87] D. B. Chklovskii, B. I. Shklovskii, and L. I. Glazman, “Electrostatics of edge channels”, Physical review. B, Condensed matter **46**, 4026–4034 (1992).

[88] K. Lier and R. R. Gerhardts, “Self-consistent calculations of edge channels in laterally confined two-dimensional electron systems”, eng, Physical review. B, Condensed matter **50**, Journal Article, 7757–7767 (1994).

[89] J. P. Eisenstein, L. N. Pfeiffer, and K. W. West, “Compressibility of the two-dimensional electron gas: Measurements of the zero-field exchange energy and fractional quantum Hall gap”, eng, Physical review. B, Condensed matter **50**, Journal Article, 1760–1778 (1994).

[90] E. Ahlswede, “Potential- und Stromverteilung beim Quanten-Hall-Effekt bestimmt mittels Rasterkraftmikroskopie”, Universität Stuttgart, de (2002).

[91] A. H. MacDonald, T. M. Rice, and W. F. Brinkman, “Hall voltage and current distributions in an ideal two-dimensional system”, Physical review. B, Condensed matter **28**, 3648–3650 (1983).

[92] S. Luryi, “Quantum capacitance devices”, Applied Physics Letters **52**, 501–503 (1988).

[93] M. Kaplit and J. N. Zemel, "Capacitance observations of Landau levels in surface quantization", Physical Review Letters **21**, 212–215 (1968).

[94] G. J. Iafrate, K. Hess, J. B. Krieger, and M. Macucci, "Capacitive nature of atomic-sized structures", eng, Physical review. B, Condensed matter **52**, Journal Article, 10737–10739 (1995).

[95] I. A. Dmitriev, A. D. Mirlin, D. G. Polyakov, and M. A. Zudov, "Nonequilibrium phenomena in high Landau levels", Reviews of Modern Physics **84**, 1709–1763 (2012).

[96] V. Daumer, I. Golombek, M. Gbordzoe, E. G. Novik, V. Hock, C. R. Becker, H. Buhmann, and L. W. Molenkamp, "Quasiballistic transport in HgTe quantum-well nanostructures", Applied Physics Letters **83**, 1376–1378 (2003).

[97] D. A. Kozlov, Z. D. Kvon, E. B. Olshanetsky, N. N. Mikhailov, S. A. Dvoretsky, and D. Weiss, "Supplemental material for "Transport properties of a 3D topological insulator based on a strained high-mobility HgTe film"", eng, Physical Review Letters **112**, Journal Article, 196801 (2014).

[98] H. J. Levinson, *Principles of lithography*, eng, 3. ed., Vol. 198, Press monograph (Spie Press, Bellingham, Wash., 2010).

[99] S. J. Weishäupl, "Quanteninterferenzeffekte in topologischen Isolatoren und magnetischen Halbleitern" (Universität Regensburg, 2015).

[100] M. Köhler, *Ätzverfahren für die Mikrotechnik*, ger (Wiley-VCH, Weinheim, 1998).

[101] Louis de Broglie, "The wave nature of the electron, Nobel Lecture", (1929).

[102] A. N. Broers, A. Hoole, and J. M. Ryan, "Electron beam lithography—Resolution limits", Microelectronic Engineering **32**, 131–142 (1996).

[103] C. T. Lewis, *A Latin dictionary, Founded on Andrews' edition of Freund's Latin dictionary*, lat;eng, in collab. with W. C. Freund, E. A. Andrews, and C. Short (Nigel Gourlay, Chapel-en-le-Frith, 2020).

[104] R. Fischer, "Induced superconductivity in HgTe based topological insulator nanowires" (Universität Regensburg, 2023).

[105] R. Franchy, T. Bartke, and P. Gassmann, "The interaction of oxygen with Nb(110) at 300, 80 and 20 K", Surface Science **366**, PII: 0039602896007819, 60–70 (1996).

[106] K. Zhussupbekov, K. Walshe, S. I. Bozhko, A. Ionov, K. Fleischer, E. Norton, A. Zhussupbekova, V. Semenov, I. V. Shvets, and B. Walls, "Oxidation of Nb(110): atomic structure of the NbO layer and its influence on further oxidation", eng, Scientific reports **10**, 3794 (2020).

[107] S. Thoms and D. S. Macintyre, "Investigation of CSAR 62, a new resist for electron beam lithography", Journal of Vacuum Science & Technology B, Nanotechnology and Microelectronics: Materials, Processing, Measurement, and Phenomena **32**, 10.1116/1.4899239 (2014).

[108] F. Lehmann, G. Richter, T. Borzenko, V. Hock, G. Schmidt, and L. Molenkamp, "Fabrication of sub-10-nm Au–Pd structures using 30 keV electron beam lithography and lift-off", Microelectronic Engineering **65**, 327–333 (2003).

[109] T. Borzenko, P. Fries, G. Schmidt, L. W. Molenkamp, and M. Schirmer, "A process for the fabrication of large areas of high resolution, high aspect ratio silicon structures using a negative tone Novolak based e-beam resist", Microelectronic Engineering **86**, 726–729 (2009).

[110] L. Ren and B. Chen, "Proximity effect in electron beam lithography", Peking University (Inst. of Microelectron., 2004).

[111] S. Gierałtowska, D. Sztenkiel, E. Guziewicz, M. Godlewski, G. Łuka, B. S. Witkowski, Ł. Wachnicki, E. Łusakowska, T. Dietl, and M. Sawicki, "Properties and characterization of ALD grown dielectric oxides for MIS structures", Acta Physica Polonica A **119**, 692–695 (2011).

[112] C. Enss and S. Hunklinger, *Low-temperature physics*, eng (Springer, Berlin, 2009).

[113] F. Pobell, *Matter and methods at low temperatures, With 28 tables, and 81 problems*, eng, 3., rev. and expanded ed. (Springer, Berlin and Heidelberg, 2007).

[114] D. J. Cousins, S. N. Fisher, A. M. Guénault, R. P. Haley, I. E. Miller, G. R. Pickett, G. N. Plenderleith, P. Skyba, P. Y. A. Thibault, and M. G. Ward, Journal of Low Temperature Physics **114**, PII: 412512, 547–570 (1999).

[115] Andeen-Hagerling Inc., *AH 2700A Ultra-Precision Capacitance Bridge*, www.andeen-hagerling.com (visited on 03/13/2024).

[116] T. H. Glisson, *Introduction to circuit analysis and design*, eng, 1. ed. (Springer, Dordrecht, 2011).

[117] J. Lawrence, A. Patel, and J. Brisson, "The thermal conductivity of Kapton HN between 0.5 and 5 K", Cryogenics **40**, 203–207 (2000).

[118] V. T. Dolgopolov, "Some experimental methods and tricks", Low Temperature Physics **37**, 188–196 (2011).

[119] R. K. Goodall, R. J. Higgins, and J. P. Harrang, "Capacitance measurements of a quantized two-dimensional electron gas in the regime of the quantum Hall effect", eng, Physical review. B, Condensed matter **31**, Journal Article, 6597–6608 (1985).

[120] Z. D. Kvon, E. B. Olshanetsky, D. A. Kozlov, N. N. Mikhailov, and S. A. Dvoretskii, "Two-dimensional electron-hole system in a HgTe-based quantum well", JETP Letters **87**, PII: 9011, 502–505 (2008).

[121] E. E. Mendez, L. Esaki, and L. L. Chang, "Quantum Hall effect in a two-dimensional electron-hole gas", eng, Physical Review Letters **55**, Journal Article, 2216–2219 (1985).

[122] M. L. Savchenko, D. A. Kozlov, N. N. Vasilev, N. N. Mikhailov, S. A. Dvoretsky, and Z. D. Kvon, "Transport properties of a 1000 nm HgTe film: the interplay of surface and bulk carriers", eng, Journal of physics. Condensed matter: an Institute of Physics journal **35**, 10.1088/1361-648X/acd5a2 (2023).

[123] J. G. Checkelsky, L. Li, and N. P. Ong, "Zero-energy state in graphene in a high magnetic field", eng, Physical Review Letters **100**, Journal Article, 206801 (2008).

[124] A. J. M. Giesbers, L. A. Ponomarenko, K. S. Novoselov, A. K. Geim, M. I. Katsnelson, J. C. Maan, and U. Zeitler, "Gap opening in the zeroth Landau level of graphene", Physical Review B **80**, 10.1103/PhysRevB.80.201403 (2009).

[125] G. M. Gusev, D. A. Kozlov, A. D. Levin, Z. D. Kvon, N. N. Mikhailov, and S. A. Dvoretsky, "Robust helical edge transport at v=0 quantum Hall state", Physical Review B **96**, 10.1103/PhysRevB.96.045304 (2017).

[126] A. A. Taskin and Y. Ando, "Berry phase of nonideal Dirac fermions in topological insulators", Physical Review B **84**, 10.1103/PhysRevB.84.035301 (2011).

[127] M. Tinkham, *Introduction to superconductivity*, eng, 2. ed., Dover books on physics (Dover Publ, Mineola, NY, 2004).

[128] R. Wördenweber, V. Moshchalkov, S. Bending, and F. Tafuri, *Superconductors at the Nanoscale* (De Gruyter, 2017).

[129] C. Buzea and K. Robbie, "Assembling the puzzle of superconducting elements: a review", Superconductor Science and Technology **18**, R1–R8 (2005).

[130] W. Meissner and R. Ochsenfeld, "Ein neuer Effekt bei Eintritt der Supraleitfaehigkeit", Die Naturwissenschaften **21**, 787–788 (1933).

[131] F. London and H. London, "The electromagnetic equations of the supraconductor", Proceedings of the Royal Society of London. A. Mathematical and Physical Sciences **149**, 71–88 (1935).

[132] R. Doll and M. Näbauer, "Experimental proof of magnetic flux quantization in a superconducting ring", Physical Review Letters **7**, 51–52 (1961).

[133] B. S. Deaver and W. M. Fairbank, "Experimental evidence for quantized flux in superconducting cylinders", Physical Review Letters **7**, 43–46 (1961).

[134] F. Colauto, M. Motta, and W. A. Ortiz, "Controlling magnetic flux penetration in low-T C superconducting films and hybrids", Superconductor Science and Technology **34**, 013002 (2021).

[135] P. W. Anderson, "Theory of flux creep in hard superconductors", Physical Review Letters **9**, 309–311 (1962).

[136] J. Bardeen and M. J. Stephen, "Theory of the motion of vortices in superconductors", Physical Review **140**, A1197–A1207 (1965).

[137] M. Baert, V. V. Metlushko, R. Jonckheere, V. V. Moshchalkov, and Y. Bruynseraede, "Composite flux-line lattices stabilized in superconducting films by a regular array of artificial defects", eng, Physical Review Letters **74**, Journal Article, 3269–3272 (1995).

[138] E. Rosseel, M. van Bael, M. Baert, R. Jonckheere, V. V. Moshchalkov, and Y. Bruynseraede, "Depinning of caged interstitial vortices in superconducting a-WGe films with an antidot lattice", eng, Physical review. B, Condensed matter **53**, Journal Article, R2983–R2986 (1996).

[139] G. R. Berdiyorov, M. V. Milošević, and F. M. Peeters, "Superconducting films with antidot arrays—Novel behavior of the critical current", EPL (Europhysics Letters) **74**, 493–499 (2006).

[140] W. Vinckx, J. Vanacken, V. V. Moshchalkov, S. Mátéfi-Tempfli, M. Mátéfi-Tempfli, S. Michotte, and L. Piraux, "Vortex pinning in superconducting Nb thin films deposited on nanoporous alumina templates", The European Physical Journal B **53**, PII: 358, 199–203 (2006).

[141] G. R. Berdiyorov, M. V. Milosević, and F. M. Peeters, "Novel commensurability effects in superconducting films with antidot arrays", eng, Physical Review Letters **96**, Journal Article, 207001 (2006).

[142] C. Reichhardt and C. J. Olson Reichhardt, "Transport anisotropy as a probe of the interstitial vortex state in superconductors with artificial pinning arrays", Physical Review B **79**, 10.1103/PhysRevB.79.134501 (2009).

[143] P. Sabatino, C. Cirillo, G. Carapella, M. Trezza, and C. Attanasio, "High field vortex matching effects in superconducting Nb thin films with a nanometer-sized square array of antidots", Journal of Applied Physics **108**, 053906 (2010).

[144] A. D. Thakur, S. Ooi, S. P. Chockalingam, J. Jesudasan, P. Raychaudhuri, and K. Hirata, "Multi-vortex versus interstitial vortices scenario in superconducting antidot arrays", Physica C: Superconductivity and its Applications **470**, 1112–1114 (2010).

[145] C. Xue, J.-Y. Ge, A. He, V. S. Zharinov, V. V. Moshchalkov, Y. H. Zhou, A. V. Silhanek, and J. van de Vondel, "Tunable artificial vortex ice in nanostructured superconductors with a frustrated kagome lattice of paired antidots", Physical Review B **97**, 10.1103/PhysRevB.97.134506 (2018).

[146] X. Ma, C. J. O. Reichhardt, and C. Reichhardt, "Manipulation of individual superconducting vortices and stick-slip motion in periodic pinning arrays", Physical Review B **97**, 10.1103/PhysRevB.97.214521 (2018).

[147] R. Panghotra, M. Timmermans, C. Xue, B. Raes, V. Moshchalkov, and J. van de Vondel, "Exploring the impact of core expansion on the vortex distribution in superconducting–normal-metal hybrid nanostructures", Physical Review B **100**, 10.1103/PhysRevB.100.054519 (2019).

[148] M. Kamran, S. R. Naqvi, T. Akram, A. u. din, S. K. He, M. Ikram, M. Usman, and S. A. Haider, "Minimizing energy losses by introducing periodic pinning centers on superconducting films", Applied Nanoscience **9**, PII: 919, 113–117 (2019).

[149] X.-H. Chen, X.-D. He, A.-L. Zhang, V. V. Moshchalkov, and J.-Y. Ge, "Vortex ice pattern evolution in a kagome nanostructured superconductor", Physical Review B **102**, 10.1103/PhysRevB.102.054516 (2020).

[150] A.-L. Zhang, V. N. Gladilin, X.-H. Chen, J. van de Vondel, V. V. Moshchalkov, and J.-Y. Ge, "Variation of local fields of pinned vortices with temperature", Applied Physics Letters **116**, 10.1063/1.5144647 (2020).

[151] A. Jones, M. Al-Qurainy, A. Hamood, S. K. H. Lam, and A. V. Pan, "Dominant factors for the pinning enhancement by large artificial partial and complete antidots in superconducting films", Superconductor Science and Technology **33**, 035004 (2020).

[152] G. Mkrtchyan and V. Schmidt, "Interaction between a cavity and a vortex in a superconductor of the second kind", Soviet Physics JETP, 195 (1972).

[153] M. M. Doria, S. de Andrade, and E. Sardella, "Maximum number of flux lines inside columnar defects", Physica C: Superconductivity **341-348**, 1199–1200 (2000).

[154] G. R. Berdiyorov, M. V. Milošević, and F. M. Peeters, "Vortex configurations and critical parameters in superconducting thin films containing antidot arrays: Nonlinear Ginzburg-Landau theory", Physical Review B **74**, 10.1103/PhysRevB.74.174512 (2006).

[155] V. V. Moshchalkov, M. Baert, V. V. Metlushko, E. Rosseel, M. J. van Bael, K. Temst, Y. Bruynseraede, and R. Jonckheere, "Pinning by an antidot lattice: The problem of the optimum antidot size", Physical review. B, Condensed matter **57**, 3615–3622 (1998).

[156] W. A. Little and R. D. Parks, "Observation of Quantum Periodicity in the Transition Temperature of a Superconducting Cylinder", Physical Review Letters **9**, 9–12 (1962).

[157] R. D. Parks and W. A. Little, "Fluxoid Quantization in a Multiply-Connected Superconductor", Physical Review **133**, A97–A103 (1964).

[158] E. Rosseel, "Critical parameters of superconductors with an antidot lattice" (Katholieke Universiteit Leuven, 1998).

[159] Y. Hatsuda, H. Katsura, and Y. Tachikawa, "Hofstadter's butterfly in quantum geometry", New Journal of Physics **18**, 103023 (2016).

[160] R. T. Huber, "Superlattice band structure engineering of Graphene" (Universität Regensburg, 2021).

[161] K. Harada, O. Kamimura, H. Kasai, T. Matsuda, A. Tonomura, and V. V. Moshchalkov, "Direct observation of vortex dynamics in superconducting films with regular arrays of defects", eng, Science (New York, N.Y.) **274**, 1167–1170 (1996).

[162] A. I. Buzdin, "Multiple-quanta vortices at columnar defects", eng, Physical review. B, Condensed matter **47**, Journal Article, 11416–11419 (1993).

[163] I. B. Khalfin and B. Shapiro, "Relaxation of magnetic flux in a superconductor with a system of columnar defects", Physica C: Superconductivity **207**, 359–365 (1993).

[164] E. Sardella, R. de Alvarenga Freire, and P. N. Lisboa-Filho, "Vortices in superconductors with a columnar defect: Finite size effects", Physica C: Superconductivity **421**, 41–48 (2005).

[165] S. I. Park and T. H. Geballe, "Tc depression in thin Nb films", Physica B+C **135**, 108–112 (1985).

[166] S. I. Park and T. H. Geballe, "Superconducting tunneling in ultrathin Nb films", eng, Physical Review Letters **57**, 901–904 (1986).

[167] J. Vanacken, W. Vinckx, V. V. Moshchalkov, S. Mátéfi-Tempfli, M. Mátéfi-Tempfli, S. Michotte, L. Piraux, and X. Ye, "Vortex pinning in superconductors laterally modulated by nanoscale self-assembled arrays", Physica C: Superconductivity and its Applications **468**, 585–588 (2008).

[168] W. Vinckx, J. Vanacken, and V. V. Moshchalkov, "Vortex pinning in Nb thin films modulated by nanospheres", Journal of Applied Physics **100**, 10.1063/1.2227711 (2006).

[169] W. J. Zhang, S. K. He, H. F. Liu, G. M. Xue, H. Xiao, B. H. Li, Z. C. Wen, X. F. Han, S. P. Zhao, C. Z. Gu, X. G. Qiu, and V. V. Moshchalkov, "Crossover behaviors in magnetoresistance oscillations for Nb thin film with rectangular arrays of antidots", EPL (Europhysics Letters) **99**, 37006 (2012).

[170] V. S. Stolyarov, T. Cren, C. Brun, I. A. Golovchanskiy, O. V. Skryabina, D. I. Kasatonov, M. M. Khapaev, M. Y. Kupriyanov, A. A. Golubov, and D. Roditchev, "Expansion of a superconducting vortex core into a diffusive metal", Nature Communications **9**, 10.1038/s41467-018-04582-1 (2018).

[171] W. Vinckx, J. Vanacken, V. V. Moshchalkov, S. Mátéfi-Tempfli, M. Mátéfi-Tempfli, S. Michotte, L. Piraux, and X. Ye, "High field matching effects in superconducting Nb porous arrays catalyzed from anodic alumina templates", Physica C: Superconductivity **459**, 5–10 (2007).

[172] A. Hazeghi, J. A. Sulpizio, G. Diankov, D. Goldhaber-Gordon, and H. S. P. Wong, "An integrated capacitance bridge for high-resolution, wide temperature range quantum capacitance measurements", eng, The Review of scientific instruments **82**, 053904 (2011).

[173] G. J. Verbiest, H. Janssen, D. Xu, X. Ge, M. Goldsche, J. Sonntag, T. Khodkov, L. Banszerus, N. von den Driesch, D. Buca, K. Watanabe, T. Taniguchi, and C. Stampfer, "Integrated impedance bridge for absolute capacitance measurements at cryogenic temperatures and finite magnetic fields", eng, The Review of scientific instruments **90**, Journal Article, 084706 (2019).

[174] R. S. Akzyanov, A. L. Rakhmanov, A. V. Rozhkov, and F. Nori, "Tunable Majorana fermion from Landau quantization in 2D topological superconductors", Physical Review B **94**, 10.1103/PhysRevB.94.125428 (2016).

Acknowledgements

In meiner akademischen Laufbahn habe ich zwei Entscheidungen getroffen, von denen ich nicht ahnen konnte, wie gut sie sich erweisen würden. Die erste war, Physik zu studieren und die zweite, bei meinem Doktorvater Prof. Dr. Dieter Weiss zu promovieren. Die Ruhe und Professionalität, mit der er mich durch die Doktorarbeit geführt hat und mir dabei stets zur Seite stand, sucht ihresgleichen. Es war genau der richtige Mittelweg zwischen selbstständig forschen und geführt werden. Wenn ich die beiden genannten Entscheidungen noch einmal treffen müsste, würde ich sie ohne zu zögern wieder genauso treffen.

Weiterhin möchte ich Herrn Prof. Dr. Christoph Strunk für die inspirierenden Gespräche und Hinweise zur Supraleitung sowie für die Bereitstellung relevanter Literatur danken! Dies hat im Laufe der Arbeit mehrfach zu signifikanten Fortschritten geführt.

Mein Dank gilt auch Prof. Dr. Jürgen Weis und Lukas Freund vom Max-Planck-Institut für Festkörperforschung in Stuttgart für die fruchtbare und produktive Zusammenarbeit.

I would also like to thank apl. Prof. Dr. Juan-Diego Urbina, Prof. Dr. Sergey Ganichev and Prof. Dr. Milena Grifoni for their interest in my dissertation and for attending my doctoral colloquium!

In addition, I would like to express my gratitude to Prof. Dr. Denis Kochan for taking the time to discuss the experimental results with me. It was a valuable insight to discuss the differing perspectives that experimental and theoretical physicists can adopt towards the same problem. Furthermore, I would like to thank him for the invitation to the workshop in Bratislava.

I would also like to thank Dr. Dmitriy Kozlov for providing the wafers, for his abundant help over the past two years and for the numerous discussions!

Darüber hinaus möchte ich mich bei folgenden Personen bedanken:

Ohne die intensive Unterstützung und den Wissenstransfer meiner Vorgänger Dr. Johannes Ziegler und Dr. Ralf Fischer wäre der Start meiner Doktorarbeit wesentlich holpriger verlaufen. Die Zusammenarbeit mit Dr. Jimin Wang ermöglichte enorme Fortschritte bei der Kapazitätsbrücke und der Entwicklung des Verständnisses von resistiven Effekten. Auch Dipl.-Ing. Dieter Riedl hat mit seinem Enthusiasmus einen unschätzbaren Beitrag zur Kapazitätsbrücke geleistet. Mia Schambeck, Leo Waldhauser und Simon Reinhardt unterstützten mich

regelmäßig mit Perl und halfen so bei der Automatisierung der Messungen. Ohne Michael Weigl wären weder der Kapazitätsprobenhalter für den Mischkryostat noch die perfekten CAD-Zeichnungen in dieser Arbeit so entstanden. Der Einsatz der Techniker Cornelia Linz, Daniel Pahl, Thomas Haller und Ulrich Gürster trug zum reibungslosen Betrieb des Lehrstuhls und damit der Experimente bei. Dazu kommen Elke Haushalter und Claudia Moser, die sich stets weit über das normale Maß hinaus um alles gekümmert haben und mir so den Rücken von bürokratischem Aufwand aller Art frei gehalten haben. Die gesamte Topogruppe, insbesondere meine direkten Doktorandenkollegen Wolfgang Himmler, Elisabeth Richter und Albert Koop haben mich bei der Arbeit mit dem Mischkryostaten, dem Magnetlabor und all den anderen Dingen sehr unterstützt.

Außerdem möchte ich mich an dieser Stelle ausdrücklich bei Dr. Vanessa Junk bedanken, die mir bei vielen Problemen in der theoretischen Physik geholfen hat und mir ein exzellentes LaTeX-Template zur Verfügung gestellt hat. Nicht zu unterschätzen ist auch der Verdienst von Benedikt Kopyciok, der mit seinen Proben und Daten wesentlich zu dieser Dissertation beigetragen hat.

Bedanken möchte ich mich auch bei meinen Master- und Bachelorstudenten Julian Maier, Benedikt Kopyciok, Lukas Rupp, Stephen Yeboah, Marcel Hild, Emanuel Traiger und Stefan Müller. Die Betreuung und Zusammenarbeit hat mir sehr viel Freude bereitet und ich habe viel von und mit euch gelernt!

I would also like to thank Dr. Dmitriy Kozlov, Dr. Vanessa Junk, Simon Reinhardt, Benedikt Grünewald, Jan Bärenfänger, Dr. Johannes Ziegler, Prof. Dr. Jürgen Weis, Benedikt Kopyciok, Dr. Nico Leumer, Elisabeth Hartl, Dr. Jimin Wang and Dr. Michael Barth for proofreading sections and chapters of this thesis.

Last, but by no means least, I would like to thank my friends, family and Beril Kadıoğlu. Their constant support, encouragement and sometimes necessary distraction throughout the five years of this dissertation have been crucial to its success!